

## An absorbing boundary condition for wave-current flow simulations in maritime applications

Chang, X.

**DOI**

[10.4233/uuid:c9c3fdea-293e-4650-a7f0-c600b178d933](https://doi.org/10.4233/uuid:c9c3fdea-293e-4650-a7f0-c600b178d933)

**Publication date**

2021

**Document Version**

Final published version

**Citation (APA)**

Chang, X. (2021). *An absorbing boundary condition for wave-current flow simulations in maritime applications*. [Dissertation (TU Delft), Delft University of Technology]. <https://doi.org/10.4233/uuid:c9c3fdea-293e-4650-a7f0-c600b178d933>

**Important note**

To cite this publication, please use the final published version (if applicable). Please check the document version above.

**Copyright**

Other than for strictly personal use, it is not permitted to download, forward or distribute the text or part of it, without the consent of the author(s) and/or copyright holder(s), unless the work is under an open content license such as Creative Commons.

**Takedown policy**

Please contact us and provide details if you believe this document breaches copyrights. We will remove access to the work immediately and investigate your claim.

# An absorbing boundary condition for wave-current flow simulations in maritime applications

Xing Chang



# An absorbing boundary condition for wave-current flow simulations in maritime applications

Proefschrift

ter verkrijging van de graad van doctor  
aan de Technische Universiteit Delft,  
op gezag van de Rector Magnificus prof.dr.ir. T.H.J.J. van der Hagen,  
voorzitter van het College voor Promoties,  
in het openbaar te verdedigen op donderdag 20 mei 2021 om 12:30 uur

door

Xing CHANG

Master of Engineering in Design and Manufacture of Naval and Marine Structures  
Wuhan University of Technology, China  
geboren te Shanxi, China

Dit proefschrift is goedgekeurd door de  
Promotor prof.dr.ir. R.H.M. Huijsmans en copromotor dr.ir. P.R. Wellens

Samenstelling promotiecommissie:

Rector Magnificus	voorzitter
Prof.dr.ir. R.H.M. Huijsmans	Technische Universiteit Delft, promotor
Dr.ir. P.R. Wellens	Technische Universiteit Delft, copromotor

Onafhankelijke leden:

Prof.dr. A.E.P. Veldman	Rijksuniversiteit Groningen
Prof.dr.ir. C. van Rhee	Technische Universiteit Delft
Prof. M.F.D.M. Visonneau	Ecole Centrale de Nantes
Dr. P. Higuera	University of Auckland
Dr. Z.L. Gao	Wuhan University of Technology
Prof.ir. J.J. Hopman	Technische Universiteit Delft, reservelid

This research was financially supported by the China Scholarship Council. The research was embedded as Work Package X in the ComMotion project that was (partly) funded by the Dutch Research Council NWO (project number: 13267).

ISBN 978-94-6419-213-1

©Xing Chang, 2021. No part of this book may be reproduced, stored in a retrieval system, or transmitted in any form or by any means without permission from the author.

The photograph on the cover shows the Doppler effect of the current on the wave pattern. The photograph was painted by Henk J. Seubers and made available to the author for illustrating the cover of this thesis, for which Henk is gratefully acknowledged.

Printed by Gildeprint, Enschede

Dedicated to my husband, Fan Liu



# Summary

## Subject and main objective

During the lifetime of ships and offshore platforms, they can be subject to harsh climate - wind, waves and currents. Currents can be wind-driven, induced by wave breaking or originate from tides. They impose a mean load on marine structures. In heavy storms, time-varying wave loads add to the current loads. Waves and structure motions can become so large that solid amounts of sea water, called 'green water', flow over the deck of ships and platforms, threatening their safety and operability. The development of our numerical method has focused on wave loads thus far, with a particular interest in green water flow. This thesis intends to add current loading to our simulations with waves.

In reality, the interaction between surface wave-current flow and numerous kinds of man-made maritime structures is local but embedded in a domain with the size of a sea. Detailed simulations of the vast domain are computationally unfeasible. Therefore, artificial boundaries are introduced to truncate the large domain so as to obtain a small domain around the structure of interest. These artificial boundaries can produce reflections which obscure the flow information from true reflectors. To eliminate the reflections from artificial boundaries, this thesis proposes absorbing boundary conditions (ABCs). The novelty is that ABCs for free surface waves in a detailed numerical model with a resolved vertical direction are derived in the presence of nonzero mean flow.

A ship at forward speed in waves can be simulated with the ship at zero forward speed in both waves and a uniform current with the magnitude of the forward velocity. An important insight of this thesis has been that with absorbing boundary conditions for waves and currents also ships at forward speed can be simulated. This thesis contains the first validated simulation of a ship at forward speed free to move in heave and pitch through irregular waves in our method.

## Numerical method

The used solver is based on ComFLOW, which is a Navier-Stokes solver (Duz (2015), van der Heiden (2019), van der Plas (2017), Wellens (2012)). A finite volume discretization on Cartesian grids has been adopted for the derivation of the numerical

method. The matrix of discrete convective terms is skew-symmetric and that of diffusive terms is symmetric negative definite. Forward Euler time discretization is applied, in which the pressure term is evaluated implicitly. Substitution of the discrete momentum equation in the discrete continuity equation results in a pressure Poisson equation. With the inclusion of the discrete absorbing boundary condition with currents, additional terms are added to the Poisson equation, which is solved iteratively by means of BiCGSTAB combined with an Incomplete Lower-Upper preconditioner (ILU).

The free surface is advected by means of an improved Volume of Fluid algorithm, consisting of a local height function that can reduce mass loss, flotsam and jetsam. The local height function fluxes the fluid in the way of aggregating the fluid in a stencil of three cells in each spatial direction. Geometries move through the fixed Cartesian grid, with their position described in a cut-cell fashion by edge and volume apertures. The object is then represented by the apertures, through which liquid cannot pass. The object movements through the grid are enabled by tracking the apertures changes over time. Prescribed movements are possible. It is also possible to determine the body movements, which are subject to the forces exerted by the fluid on it, by solving the equations of the body motion. The combined system of ships and fluid is solved by a quasi-simultaneous coupling method which makes use of an interaction law.

### **Absorbing boundary conditions for waves on top of currents**

Reflections of waves and currents from the domain boundaries can violate the field solution inside the domain. Certain measures should be taken to prevent this disturbance. Damping zones are often used near domain boundaries to dissipate the wave energy. They usually take up a large proportion of the total computational resources in the simulations, while local absorbing boundary conditions can be more efficient, see Duz (2015), Wellens (2012). In this thesis, a local absorbing boundary condition for long-crested irregular waves on top of a current is derived and investigated.

The Sommerfeld conditions including the effect of currents in this work were inspired by the factorization of the planar wave equation including currents. They absorb plane waves in currents according to the direction in which the waves propagate with currents. For a regular wave, its propagation direction is known and thus can be used as a criterion for the design of the boundary condition. In the case of waves from more than one direction, the maximum reflection coefficients are used for the choice of the absorption direction. Multiplication of two absorption operators gives the opportunity to account for multi-directional waves.

The absorbing boundary conditions in this work are obtained from an approximation of the dispersion relation, which is accurate within a range of wave numbers. Second-order vertical derivatives of the solution variables along the boundary estimate the wave number in the dispersion relation. The discretized absorbing boundary conditions can be combined with the discrete momentum equation inside the domain and the pressure Poisson equation.

## Verification study

The first-order Sommerfeld condition (S-1), generating and absorbing boundary condition (GABC-1) and second-order absorbing boundary condition (ABC-2), all including the effect of uniform currents, are verified by means of combined wave-current simulations.

Firstly, with regular waves on top of currents, the performance of the boundary conditions S-1 and GABC-1 are assessed. Six currents: three following and three opposing ones, are accounted for. For each current, 25 monochromatic waves, varying from small amplitude waves to mildly steep waves, are applied.

For each current, the simulated surface elevations for four waves, varying from small amplitude waves to mildly steep waves at the inflow boundary are compared to the input waves first. Subsequently, numerical surface elevations for the above four waves at four positions in the domain, from near the inflow boundary to near the outflow end, are shown. Lastly, the numerical reflection coefficients, defined as the ratio of the reflected wave amplitude and the outgoing wave amplitude, are presented in comparison with theoretical values.

For all the following current velocities:  $U = 0.5 \text{ m/s}$ ,  $U = 1.0 \text{ m/s}$  and  $U = 2.0 \text{ m/s}$ , and the opposing currents:  $U = -0.5 \text{ m/s}$  and  $U = -1.0 \text{ m/s}$  in the water depth of  $10 \text{ m}$ , the simulated reflection coefficients match well with the theory. However, for a larger opposing current  $U = -2.0 \text{ m/s}$ , the reflections for input waves with the  $kh$  values larger than 2.4, are hardly observed due to excessive dissipation.

A JONSWAP wave spectrum, with the peak period of  $6 \text{ s}$  and significant wave height of  $2 \text{ m}$ , is used to further test the boundary condition GABC-1. Two currents: one following and one opposing, are imposed. In each test, the numerical input spectrum was first compared with the theoretical spectrum, followed by the comparison of the reflection coefficients for the entire spectrum. The simulated reflections in the case of the following current are less than 3% in the entire spectrum. On the whole, they are smaller than the theoretical results. In the presence of the opposing current, the numerical reflection coefficients for shorter waves are larger than theory.

As the last example for the verification, a test of an oscillating sphere on top of currents is utilized to observe the performance of the second-order boundary condition ABC-2 with currents. It is an interesting test because all directions between waves and currents are contained in one simulation. This allows us to assess our boundary condition in a three dimensional domain. The lengths of the waves radiated by the vertically oscillating sphere in different directions, especially in the direction of following currents, normal currents and opposing currents, are extracted from the simulations and compared with the theory. The ratios of wave amplitudes at different radii in these three directions are also compared to theoretical values. From the observations, the boundary condition performs well on fine grids.

## Validation study

Experimental tests with a scale model of a Wigley hull at forward speed in both regular and irregular waves were performed in the towing tank at Delft University of Technology. The heave and pitch motions of the Wigley hull were measured with two vertical position gauges, located half a meter away from the center of gravity of the model. The other four DoF were kept restrained during the experiments.

In ComFLOW simulations, the same Wigley was used. The width and water depth of the computational domain were specified as same as in the experiment. A grid study was first carried out to obtain sufficient grid resolution for representing the waves at the position where the ship was supposed to be, followed by a sensitivity study to investigate how close the inflow and outflow boundaries can be placed around the structure. For the cases of two regular waves, the positions of the inflow and outflow boundaries were positioned at 2.5 and 1.67 times of the ship's length away from the center of the hull, respectively. Input waves in the simulations were generated with linear wave theory. For the cases of the Wigley hull moving in regular waves, the generating and absorbing boundary conditions with currents derived in this work were applied at both the inflow and outflow boundaries of the domain, while in the test of irregular waves, absorbing boundary conditions with currents were used at the outflow boundary. For all simulations, the resulting heave and pitch motions of the hull agree well with the experiments.

Based on the validated wave and ship motions, an application of green water impact on the deck of the Wigley hull in extreme waves was investigated. In these simulations, the waves were obtained by scaling the amplitudes of the wave components in the experiment by a factor of 6. Time histories of the surface elevations at different locations on the deck were presented, as well as the pressure signals at different positions. With the method being validated for milder waves, the application demonstrated how the numerical method can be used as a first-principle-based extrapolation to more extreme waves.

On the whole, the validation study in this work proved that the extended boundary condition GABC-1 including the effect of currents can be applied efficiently in the application of the structure at forward speed in long-crested waves.

# Samenvatting

## Onderwerp en doel en het onderzoek

Tijdens de levensduur van schepen en offshore constructies worden ze blootgesteld aan ruwe weerscondities met wind, golven en stroming. Stroming kan door de wind zijn aangedreven, door golfbreken worden veroorzaakt of het gevolg zijn van het getij. Stromingen oefenen een gemiddelde belasting uit op constructies in de zee. In zware stormen komen daar tijdsvariërende belastingen bij. De golven, en de bewegingen van de constructie kunnen zo hoog worden dat hoeveelheden water op het dek terecht komen. Dit noemt men "groen water" op het dek, en dit kan de veiligheid en inzetbaarheid van het schip in gevaar brengen. De ontwikkeling van onze numerieke methode heeft zich tot nu gericht op golfbelastingen, en dan in het bijzonder groen-waterbelastingen. Met dit proefschrift willen we het mogelijk maken stroming toe te voegen aan onze simulaties met golven.

Voor een constructie op zee is de interactie met golven en stroming weliswaar een lokaal proces nabij de constructie, maar dit proces is afhankelijk van wat er in de hele zee gebeurt omdat golven zich over grote afstanden verplaatsen. Het is niet mogelijk om de hele zee te simuleren met het door ons gewenste detailniveau. Daarom simuleren we in een domein dat net voldoende groot is om de constructie in te laten passen. Zo'n rekendomein heeft domeinwanden of -randen en als we niets speciaals doen bij deze randen, dan worden alle golven daar gereflecteerd alsof door een muur. De golfreflectie van randen is niet zoals het in werkelijkheid is op zee en verstoort de golfinteractie met de constructie zoals deze zou moeten zijn. Om dergelijke golfreflectie te voorkomen, worden in dit proefschrift absorberende randvoorwaarden afgeleid. De vernieuwende bijdrage is dat er nu absorberende randvoorwaarden zijn voor de simulatie van golven in het vrije vloeistofoppervlak met een gedetailleerd numeriek model in aanwezigheid van stroming met een snelheid die niet nul is. De verticale richting wordt in dit model volledig opgelost.

Een ship met voorwaartse snelheid in golven kan worden gesimuleerd door het schip stil te houden en een combinatie van golven en stroming op te leggen, met de grootte van de stroomsnelheid gelijk aan de voorwaartse snelheid die we proberen te simuleren. Een belangrijk inzicht dat tijdens het samenstellen van dit proefschrift ontstond was dat de absorberende randvoorwaarden voor golven en stroming dus ook voor schepen met voorwaartse snelheid kunnen worden gebruikt. Dit proefschrift bevat de eerste

gevalideerde simulatie van een schip met voorwaartse snelheid in onregelmatige golven, waarbij het schip vrij kon dompen en stampen.

## Numerieke methode

ComFLOW is een numerieke oplosmethode voor de Navier-Stokes-vergelijkingen. Er wordt een eindige-volumediscretisatie van de vergelijkingen gebruikt op een vast, cartesisch rooster. Een belangrijk kenmerk van de discretisatie is dat de matrix van de discrete convectieve term scheefsymmetrisch is en dat de matrix van de diffusieve term symmetrisch is en negatief-definiet, net zoals de termen in de continue modelvergelijkingen. Euler Voorwaarts wordt gebruikt als tijddiscretisatie van de impulsvergelijking, waarbij de druk impliciet wordt geëvalueerd. Wanneer de impulsvergelijking wordt gesubstitueerd in de continuïteitsvergelijking, dan levert dat een Poissonvergelijking op voor de druk. De absorberende randvoorwaarden voor golven en stroming uit dit proefschrift worden gecombineerd met de Poissonvergelijking, die vervolgens iteratief wordt opgelost met een BiCGSTAB-methode met ILU preconditioner.

Het vrij oppervlak wordt verplaatst met een verbeterd Volume-of-Fluid (iVOF) algoritme met lokale hoogtefunctie, die verlies van massa beperkt en “flotsam and jetsam”, kleine hoeveelheden vloeistof die niet meer door het algoritme worden verplaatst, helpt voorkomen. De lokale hoogtefunctie werkt doordat het fluxen van vloeistof geïntegreerd wordt in een lokaal volume van  $3 \times 3 \times 3$  cellen in 3D rond de cel waarin de flux bepaald wordt. Objecten snijden door het rooster door rand- en volumeapertures te administreren waar vloeistof doorheen kan fluxen en waar vloeistof zich kan bevinden. Het object is dan gerepresenteerd door het complement van de apertures, waar vloeistof niet doorheen kan. Verplaatsingen van het object door het rooster worden mogelijk gemaakt door veranderingen van de apertures in de tijd bij te houden. Voorgescreven bewegingen zijn mogelijk, maar het is ook mogelijk om de verplaatsing van het lichaam onderhevig te laten zijn aan de krachten die de vloeistof erop uitoefent door een bewegingsvergelijking voor het lichaam op te lossen. Om de bewegingsvergelijking van het object efficiënt samen met de vloeistofbeweging op te lossen wordt een zogenoemde Interactiewet gebruikt.

## Absorberende randvoorwaarde voor golven en stroming

Als gezegd zullen golfreflecties van domeinwanden de simulatie van golfinteractie met een object in het rekendomein verstoren. Deze verstoringen moeten worden gemitigeerd. Vaak worden dempingszones of numerieke stranden gebruikt om golfenergie te dissipiëren. Dempingszones moeten groot zijn en nemen een groot deel van de rekenkracht in beslag die nodig is om de simulatie uit te voeren. Lokale randvoorwaarden zijn gedefinieerd op de rand die dicht bij het object gekozen kan worden, en gebruiken daardoor minder rekenkracht dan dempingszones. Absorberende randvoorwaarden voor golven en stroming in één simulatie bestaan nog niet en daarom worden ze in dit proefschrift afgeleid en onderzocht.

De Sommerfeld randvoorwaarden voor golven waarin het effect van een gemiddelde

stroming is meegenomen zijn geïnspireerd op het factoriseren van de golfvergelijking in een vlak met stroming. Deze zijn absorberend voor golven in stroming in de richting waarin de golven lopen. Voor regelmatige golven is de richting bekend en kan dus meegenomen worden bij het opstellen van de randvoorwaarde. In situaties met meerdere golfcomponenten, die ieder een eigen richting hebben, kan de richting van de component met de hoogste energie onderdeel zijn van de randvoorwaarde. Als de randvoorwaarde wordt vermenigvuldigd met nog een randvoorwaardeoperator, dan kunnen meer richtingen ingesteld worden zodat daarmee een bereik wordt opgespannen waartussen de reflectiecoëfficiënt als functie van golfrichting laag is.

Om het bereik van de randvoorwaarde als functie van het golfgetal (of, equivalent, golf-frequentie) te vergroten wordt de Sommerfeld randvoorwaarde gecombineerd met een Padé benadering van de dispersierelatie in termen van het golfgetal. De termen met het golfgetal worden vervangen door tweede afgeleiden van de oplossingsgrootheden langs de rand, zodat de randvoorwaarde niet meer afhankelijk is van een specifieke invoerwaarde voor het golfgetal. De randvoorwaarde is nauwkeurig voor die golfgetallen waar ook de benadering van de dispersierelatie nauwkeurig is. Na discretisatie wordt de absorberende randvoorwaarde gecombineerd met de impulsvergelijking en toegevoegd aan het stelsel met de Poissonvergelijking.

## Verificatiestudie

Verschillende varianten van de absorberende randvoorwaarde met stroming zijn op werkzaamheid getest in sommen met daarin zowel golven als stroming. De variant Sommerfeld noemen we S-1 en is met name geschikt voor regelmatige golven met 1 dominant golfgetal. De variant met de benadering van de dispersierelatie noemen we GABC-1; deze is nauwkeurig voor een bereik aan golfgetallen, dus voor meerdere golfcomponenten met een verdeling van energie zoals in een golfspectrum. Tot slot is er nog de variant met de extra randvoorwaarde operator, die nauwkeurig is voor een bereik aan golfrichtingen en golfgetallen. Deze noemen we ABC-2.

Eerst hebben we S-1 en GABC-1 getest in sommen met regelmatige golven en verschillende stroomsnelheden. Er zijn 6 waarden voor de uniforme stroomsnelheid gebruikt, drie met de stroming in de richting van de golven, drie met tegenstroming. Bij iedere stromingssituatie zijn 25 sommen gedaan met evenzoveel verschillende golfgetallen om een goed beeld te krijgen van het volledige bereik. De steilheid was mild, om niet-lineair gedrag van de regelmatige golven te beperken. In totaal zijn er in deze test 150 sommen gedaan.

De gesimuleerde oppervlakteuitwijkingen in de test met regelmatige golven zijn vergeleken met wat ze theoretisch zouden moeten zijn. Vervolgens zijn de oppervlakteuitwijkingen op 4 locaties, dichtbij de inkomende rand en de uitgaande rand, gebruikt om de amplitudes van de inkomende en gereflecteerde te bepalen. De verhouding van gereflecteerde amplitude en inkomende amplitude definieert de reflectiecoëfficiënt. De reflectiecoëfficiënt uit elk van de simulaties is bepaald en vergeleken met de theoretische reflectie.

Voor alle stroomsnelheden, behalve  $U = -2.0$  m/s, komen de reflectiecoëfficiënten in de regelmatige golfsimulaties goed overeen met theorie. Voor de situatie  $U = -2.0$  m/s, voor waarden van het dimensieloze golfgetal  $kh$  groter dan 2.4, was het nauwelijks mogelijk om de reflectiecoëfficiënt te bepalen omdat er overdreven veel dissipatie van de inkomende golf was. Het is nog niet duidelijk hoe dit veroorzaakt wordt en dat moet worden onderzocht.

Voor een volgende test van de randvoorwaarde GABC-1 is een JONSWAP-golfspectrum met piekperiode 6 s en significante golfhoogte 2 m gesimuleerd. In een simulatie was een onderliggende stroming van 0.5 m/s met de golven mee gedefinieerd; in een andere simulatie een tegenstroming van -0.5 m/s. Voor elke test is eerst het in de simulatie verkregen golfspectrum vergeleken met het theoretisch golfspectrum. Vervolgens is het reflectiespectrum bepaald dat door de randvoorwaarde veroorzaakt wordt. De reflectiecoëfficiënt voor alle waarden van  $kh$  is verkregen door het gereflecteerd golfspectrum te delen door het inkomend golfspectrum en de wortel van de uitkomst te bepalen. De gesimuleerde reflectiecoëfficiënt is iets lager dan de theoretische reflectiecoëfficiënt.

Als laatste verificatie is een test uitgevoerd met een dompende boei in een stroming om te onderzoeken hoe goed de ABC-2 met stroming werkt. Deze test is interessant omdat alle hoeken tussen stroming en golven tegelijkertijd in dezelfde simulatie aanwezig zijn, en goed het effect van de hoek van de golfrichting met de domeinrand kan worden onderzocht. De golflengte van de geradieerde golf is in elke richting anders. De golflengtes in de verschillende richtingen zijn bepaald en vergeleken met de theoretische waardes. Ook is de verhouding van de amplitudes als functie van de afstand tot de boei bepaald. Golflengte en -amplitude komen goed overeen met theorie, waaruit blijkt dat de randvoorwaarde ABC-2 het goed doet.

## Validatiestudie

Experimenten zijn uitgevoerd in de kleine sleeptank in Delft voor een schaalmodel van de Wigley rompvorm met voorwaartse snelheid in regelmatige en onregelmatige golven. De golven zijn gegenereerd met een roterend golfschot aan een kant van de tank. Aan de andere kant was een parabolisch strand geïnstalleerd om golfreflectie te reduceren. Het schaalmodel, met een lengte van 3.0 m, lag initieel ver bij het golfschot vandaan. Na aanvang van de metingen werd het model door kopgolven gesleept. Het dompen en stampen van de Wigley zijn gemeten met twee, in verticale richting geïnstalleerde potmeters op 0.5 m afstand aan weerszijde van het zwaartepunt. Bewegingen van het model in andere vrijheidsgraden werden tegengehouden.

Met ComFLOW zijn simulaties uitgevoerd met hetzelfde model. De breedte en diepte van het rekendomein kwamen overeen met de breedte en diepte van de sleeptank. Eerst is onderzocht met een roosterverfijningsstudie welk rooster geschikt zou zijn om de golven te representeren. Daarna is een gevoeligheidsstudie gedaan om te onderzoeken hoe dicht de domeinranden in longitudinale richting ( $x$ -richting) bij het

model geplaatst konden worden. Uiteindelijk is gekozen om de inkomende golfrand op 1.7 keer de scheepslengte, en de uitgaande golfrand op 2.5 keer de scheepslengte bij de voor- en achterkant van het schip vandaan te leggen. De inkomende golven zijn gegenereerd door gebruik te maken van lineaire golftheorie. Voor de regelmatige golf-simulaties is de S-1 randvoorwaarde gebruikt. Voor de simulaties met onregelmatige golven is de GABC-1 randvoorwaarde gebruikt. De simulaties voor de Wigley komen goed overeen met de experimenten.

Met het gevalideerde rooster is een toepassing van groenwater met ComFLOW-simulaties onderzocht. De golven in deze simulaties zijn verkregen door de amplitudes van de golfcomponenten in het experiment te schalen met een factor 6. Als uitvoer van de simulaties zijn waterstanden op het dek en de drukken op een constructie aan dek gegenereerd en gevisualiseerd. Deze toepassing is een voorbeeld van hoe de numerieke methode gebruikt kan worden om, vanuit een gevalideerde situatie, de modelvergelijkingen voor massa en impuls te gebruiken voor een extrapolatie naar de meer extreme situaties waar ComFLOW voor gemaakt is.

Met de validatie en de toepassing voor groenwater kan gesteld worden dat de GABC-1 absorberende randvoorwaarde, inclusief het effect van stroming, goed toegepast kan worden in simulaties van schepen met voorwaartse snelheid en golven.

De voornaamste conclusie van het hele proefschrift is dat de afgeleide en geïmplementeerde absorberende randvoorwaarden voor golven in combinatie met stroming overeenkomen met de theorie en dat daar praktische simulaties efficiënt mee kunnen worden uitgevoerd.



# Contents

<b>Summary</b>	<b>vii</b>
<b>Samenvatting</b>	<b>xi</b>
<b>1 Introduction</b>	<b>1</b>
1.1 Analytical study of wave-current interaction . . . . .	2
1.2 Experimental study of wave-current interaction . . . . .	3
1.3 Numerical study of wave-current interaction . . . . .	4
1.3.1 Prevention of wave reflection . . . . .	4
1.3.2 Advancing ships in head waves . . . . .	6
1.4 This research . . . . .	6
1.5 Outline . . . . .	7
<b>2 Mathematical and numerical modeling</b>	<b>9</b>
2.1 Mathematical modeling . . . . .	9
2.1.1 Governing equations . . . . .	9
2.1.2 Boundary conditions . . . . .	11
2.2 Computational domain and grid . . . . .	13
2.3 Continuity equation . . . . .	15
2.4 Momentum equation . . . . .	16
2.4.1 Convection . . . . .	16
2.4.2 Diffusion . . . . .	17
2.4.3 viscous normal stress . . . . .	17
2.4.4 Shear stress . . . . .	18
2.4.5 Pressure . . . . .	19
2.5 Time Integration . . . . .	20
2.6 Stability . . . . .	22
2.7 Interaction with a moving body . . . . .	22
2.8 Free surface . . . . .	24
2.8.1 Boundary conditions at the free surface . . . . .	25
2.8.2 Discrete velocities at the free surface . . . . .	26
2.8.3 Discrete pressures at the free surface . . . . .	26

<b>3</b>	<b>ABCs with uniform current</b>	<b>27</b>
3.1	Absorbing boundary conditions . . . . .	27
3.2	Factorization of the wave equation . . . . .	28
3.3	Outflow boundary condition . . . . .	29
3.3.1	Wave equation with uniform current . . . . .	29
3.3.2	Derivation of the ABC . . . . .	33
3.4	ABC with uniform current . . . . .	34
3.4.1	Pade approximation of the dispersion relation . . . . .	34
3.4.2	Relating the wave number and the potential . . . . .	35
3.4.3	Boundary conditions in terms of primitive variables . . . . .	37
3.5	Stability . . . . .	39
3.5.1	Dispersion relation of progressive, evanescent and spurious waves	40
3.5.2	Padé approximation of the dispersion relation . . . . .	40
3.6	Discretization of the boundary conditions . . . . .	42
<b>4</b>	<b>Verification Results</b>	<b>49</b>
4.1	Tests: Regular waves on currents . . . . .	49
4.1.1	S-1 with current . . . . .	50
4.1.2	GABC-1 with current . . . . .	57
4.2	Tests: irregular waves on currents . . . . .	64
4.3	Oscillating sphere in currents . . . . .	69
<b>5</b>	<b>Validation results</b>	<b>75</b>
5.1	Introduction . . . . .	75
5.2	Experiment modeling . . . . .	77
5.3	Numerical simulation . . . . .	77
5.3.1	Grid study . . . . .	78
5.3.2	Sensitivity study . . . . .	79
5.3.3	Wigley hull at forward speed in irregular waves . . . . .	82
5.3.4	Application: green water in extreme waves . . . . .	85
5.3.5	Discussion . . . . .	89
<b>6</b>	<b>Conclusions</b>	<b>93</b>
<b>A</b>	<b>1D reflection coefficient</b>	<b>99</b>
<b>B</b>	<b>2D reflection coefficient</b>	<b>101</b>
<b>C</b>	<b>Coefficients in ABC-2</b>	<b>105</b>
	<b>Bibliography</b>	<b>107</b>
	<b>Acknowledgements</b>	<b>113</b>
	<b>Curriculum Vitae</b>	<b>115</b>

# Chapter 1

## Introduction

Ships and offshore structures play important roles in the exploration, extraction and production of oil and gas under the seabed. Offshore platforms can be fixed to the ocean bottom in shallow water, such as jack up rings and concrete gravity platforms. In deep water, floating systems are required. For example, a tension-leg platform is moored through tethers or tendons. The semi-submersible unit is another type of floating production system, which is usually moored by anchors with ropes and chains, or is dynamically positioned using rotating thrusters.

During the lifetime of ships and offshore platforms, they can be subject to harsh climate - wind, waves and currents. In heavy storms, waves and structure motions can become so large that solid amounts of sea water, called 'green water', flow over the deck of ships and platforms, threatening their safety and operability. Waves and currents can also exert loads on the mooring system and thus induce vortex shedding. Modelling of wave loads on structures at sea is incomplete without currents and thus the combination of currents and waves is an important aspect of simulating a realistic loading environment. Prediction of nonlinear forces exerted on the structures demands that we consider the combination of waves and currents.

Computational fluid dynamics (CFD) has become more and more popular for researchers to evaluate the performance of wave-current-structure interaction, with the rapid development of high-performance computer hardwares. However, numerical wave simulations become unrealistic if one does not make sure to prevent wave reflections from the computational domain boundaries. Damping zones are usually employed to dissipate wave energy, but this method requires large extra domain lengths and thus extra computational efforts. As an alternative, an absorbing boundary condition (ABC) is another way to prevent wave reflections, which forms the foundation of this thesis.

This study fits within the framework of ComFLOW, which is a Navier-Stokes solver. It can deal with breaking waves, green water on deck and wave-in-deck situations. It has a long tradition dating back to 1995 and has been in continuous development

from that moment until today, see Gerrits (2001), Fekken (2004), Kleefsman (2005), Wemmenhove (2008), Wellens (2012), Duz (2015), van der Plas (2017) and van der Heiden (2019).

Before this thesis, one could do either current simulations with ComFLOW, or wave simulations, but not the combination. However, in reality waves and currents, for instance those induced by tides, are always present together. Therefore, working on absorbing boundary conditions for combined wave-current simulations is a next step towards representing realistic wave and current conditions.

The main research topic of this thesis is the subject of the absorbing boundary conditions for the numerical simulation of combined wave-current flows in truncated domains for maritime applications. In this introductory chapter, the analytical, experimental and numerical contexts of the wave-current flows are presented.

## 1.1 Analytical study of wave-current interaction

An early analytical study of wave-current interaction was performed by Peregrine and Jonsson (1983), in which a variety of aspects have been elaborated, including how to account for the Doppler effect in the wave dispersion equation when currents are present, refraction of waves by currents through the concept of wave action, wave dissipation with the introduction of currents and wave breaking with the influence of currents. The Doppler effect in the wave dispersion relation is going to be important for absorbing boundary conditions in this work.

One of the interesting phenomena is wave blockage by opposing currents, where the wave group velocity is smaller than the current speed. Wave blockage can occur in regions such as estuaries. The opposing currents yield an increase in the wave steepness, which may result in wave breaking. Since the wave field is changed drastically over the blocking region, it is significant to know under which conditions wave blockage will take place for coastal engineers. For more information on wave blockage, see Chawla and Kirby (1998), Suastika (2004) and Onorato et al. (2011).

In addition, the tidal turbine is a favourable invention to convert the kinematic energy of tidal currents into electrical energy. Currents can be significantly changed by the waves, which will influence the performance of tidal turbines, see Henriques et al. (2014).

Since the uniform currents in this thesis have been fully sent into the computational domain initially, we will not study the processes of wave blockage. Numerical simulations of regular and long-crested irregular waves in the presence of opposing uniform currents in truncated domains will be investigated, to verify our boundary conditions at the inflow and outflow boundaries.

From the author's knowledge, boundary conditions to infinity in the analytical study

of wave-current flows are scarcely found in the literature. Since the present work does not focus on the mechanism of how waves and currents influence each other, we refer the readers to Lane et al. (2006) and Soulsby et al. (1993) for more insights.

## 1.2 Experimental study of wave-current interaction

There also exist experiments to investigate wave-current flows such as by Fernando et al. (2014), Liu et al. (1992) and Swan et al. (2001). One difficulty in the experiments is to obtain the desired current profile (uniform or sheared) by means of pumps. Detailed measures in this literature are described below. They can basically be categorised into two types: passive and active ones.

In a passive absorber, if there is effective absorption, reflections can be close to zero. A beach is one of often-used passive absorbers to dissipate wave energy. For example, a series of experiments have been performed by Liu et al. (1992), from direct observation of particles orbits using Particle Image Velocimetry (PIV) measurements, to obtain the proper beach configuration.

Polyether foam can also be employed in the wave-current flume to damp the wave motion. In the work of Swan et al. (2001), the front end of the foam has been cut to form a vertical wedge with an angle of  $30^\circ$ . The largest reflection coefficient within the flume is measured to be less than 1% using this method of passive absorption.

Others, for example Fernando et al. (2014), use plywood walls coated with resins to minimize the propagating wave resistance from the side walls. Besides, three layers of sandbags are randomly placed along the side walls to dissipate diffracted waves. A porous slope made of crushed stones is adopted to absorb waves at the outflow end of the basin. The reflection coefficient from the slope is controlled to be less than 6%.

In an experimental context, active absorption refers to the use of a wavemaker as a moving boundary, in response to measurements of the surface elevation on the wave board, to absorb waves impinging on it. It has been clearly stated by Wellens (2012) that the accuracy obtained from active wave absorption is limited due to three main reasons. First of all, the measurements of the surface elevation are influenced by the motion of the wave board. Besides, evanescent wave modes near the board can disturb measurements of the outgoing waves. The third reason is that long waves require a long stroke, but the wave board has a limited stroke.

The advantages of employing an active absorption system in a physical wave basin or flume can be found in the introduction of the software AUKEPC (see online) in Deltares. Moreover, Hemming and Klopman (1985) reviewed the design requirements for the active system.

## 1.3 Numerical study of wave-current interaction

Numerical simulations play an important role in the study of wave-current interaction. Similar to the experimental study, we will focus on how wave reflection is prevented in the numerical simulations. The study of combined wave-current flow can find its application in the area of ships at forward speed in waves, because one can keep the domain boundaries close to the structures.

### 1.3.1 Prevention of wave reflection

A damping zone is most frequently used to dissipate wave energy in numerical simulations. Different damping schemes are adopted in the literature.

**Passive wave absorption** For example, a gradually coarsen grid and an increasing viscosity distribution have been employed by Teles et al. (2013) at the outflow end of the computational domain, which results in a damping area of six wave lengths.

Another method is to modify the horizontal velocity in the wave making region and outflow end of the domain with a dissipative coefficients, see Li and Lin (2015), for the purpose of absorbing wave re-reflection from the input boundary and reflection from the end wall. Some research such as Zhang et al. (2014) employs a damping scheme on the vertical velocity at the in/outflow boundaries to avoid the reflection of incident waves and interference of inflow currents. In Park et al. (2001), an artificial damping acting on both the horizontal and vertical velocities are added to the momentum equation.

In Wellens (2012), a pressure damping zone, in which an additional pressure proportional to the vertical velocity at the free surface, is mentioned.

Analogous to a beach in the experimental basin, the vertical velocity and pressure damping zones are more efficient for short wave components than for long wave components, because the dissipation is proportional to the vertical velocity. The vertical velocities in long waves are small, and thus long dissipation zones are required to sufficiently prevent reflection.

Another often-used approach to dissipate waves is the use of relaxation zones. This method has been employed by Park et al. (1999) and Choi and Yoon (2009), in which momentum source terms are incorporated in the governing equations to dissipate waves. Peric and Abdel-Maksoud (2015) discussed momentum source terms based on linear and quadratic damping functions systematically. This paper investigated how the damping functions work, on which factors the damping quality depends and how reliable wave damping can be set up case-independently.

Boundary Element Method (BEM) is also used to investigate wave-current simulations. For example, Koo and Kim (2007) applied a  $\phi - n$  and  $\eta$ - type damping on the free surface in front of the wave maker and end wall to prevent wave reflection.

**Active wave absorption** The above mentioned approaches belong to passive absorbers. Active wave absorption can also be found in the wave-current simulations. In Higuera et al. (2013) and Paolo et al. (2018), based on the shallow water theory in the 2D case where the velocity along the vertical direction is constant, the relation  $uh = c\eta$  can be derived. Here  $h$  and  $\eta$  are required to be measured.  $u$  is the horizontal velocity, which is the variable to solve for.  $c$  denotes the wave phase speed and is estimated as  $\sqrt{gh}$ . In order to cancel out reflected waves, the boundary must generate a velocity equal to the incident one but in the opposite direction. Therefore, the active wave absorption designed for the surface elevation of the reflected wave  $\eta_{refl}$  can be expressed as  $u = -\sqrt{\frac{g}{h}}\eta_{refl}$ . This is the correction value that is specified to a velocity which is normal to the boundary. The reflected wave elevation  $\eta_{refl}$  is determined from subtracting the measured elevation at the wavemaker from the target one. This approach is a static boundary and only for shallow water.

Later, Higuera et al. (2015) extended this active wave absorption to a moving boundary in shallow water, where the equation  $u = -\sqrt{\frac{g}{h}}\eta_{refl}$  is expressed in differential form:  $\frac{dX}{dt} = -\sqrt{\frac{g}{h}}\eta_{refl}$ . The correction displacement of the paddle can then be represented in terms of an integral from the start of the test to the current time. Further on, the active wave absorption method was developed to consider any water depth by applying the wave celerity  $c$  and horizontal velocity  $u$  in a different way. More details can be found in the work of Higuera (2020).

**PML and external method** An alternative to damping zones can be Perfectly Matched Layers (PMLs), see Berenger (1994). Unlike the above mentioned methods, the PML requires an additional set of equations to be solved. Moreover, it is possible to impose wave kinematics from external methods on the downstream side of the computational domain. More details can be found in Wellens (2012).

As can be seen in these applications, the interaction between surface wave-current flow and maritime structures is local but takes place in a vast domain. For improved computational efficiency, artificial boundaries are introduced to truncate the large domain so as to obtain a small domain around the object of interest. These artificial boundaries can produce reflections that give unrealistic results inside the computational domain. To get rid of the reflections from artificial boundaries, absorbing boundary conditions (ABCs) are desired, see Wellens and Borsboom (2020).

**Absorbing boundary conditions (ABCs)** While prescribing absorbing boundary conditions for maritime applications, one has basically two main objectives. The first is to let the outflow arriving at the boundary go without reflection, in a way that is compatible with the mathematical and numerical methods inside the domain. The second is to provide some additional knowledge on inflow.

In contrast to active wave absorption which responds to the reflected waves with a control system, the method of ABCs acts as a type of passive operation to the waves impinging on the boundaries. ABCs can be categorized into two types: global and local ABCs. It has been discussed in Wellens (2012) that global absorbing boundary

conditions are computationally undesirable, due to the requirement of storage of all previous time steps and processing of all grid points at each time step. In addition, it is also not clear how to add currents in the global ABCs. Therefore, attention will be paid to local ABCs. The different perspectives to derive absorbing boundary conditions are reviewed at the start of Chapter 3. No ABCs with currents have been found that can readily be incorporated into the numerical model ComFLOW.

Here we highlight the requirements for the design of an ABC including uniform currents to be implemented in ComFLOW. Firstly, the computational cost to prevent wave reflection in the presence of currents should be marginal compared to the resources devoted to solve the solution field. Secondly, it should be feasible to locate the domain boundaries close to the geometries of interest, which can save a lot of computer memories than using damping zones. Thirdly, the stability of the equations inside the domain should not be influenced by the ABC including uniform currents.

### 1.3.2 Advancing ships in head waves

A ship at constant speed in head waves can be simulated with the ship at zero forward speed in both waves and a uniform current in the opposite direction of the ship. An important insight of this thesis has been that with absorbing boundary conditions for waves and currents also ships at a forward speed could be simulated. The experimental study in this thesis is on a Wigley hull moving at a forward speed in head waves in the towing tank and is used to validate the simulation results.

Some research, for example by Journee (2007), Karim and Naz (2017) and Sherbin and Kings (2018), focuses on the resistance analysis of a Wigley hull in waves, while other efforts are devoted to the motions of a Wigley hull at forward speed in waves. For instance, Dumitru (2016) pays attention to the simultaneous resonance case where the external excitation period is near the pitch period. Sato et al. (1999) employs a finite volume method, in the framework of a boundary-fitted grid system, together with the marker-density-function to predict the motions of Wigley hull. A numerical prediction of the motion response of a Wigley hull in long-crested irregular waves is presented by means of the URANS-VOF method. More interesting for our applications is the green water problem on the deck of the Wigley hull, which can take place with a sufficiently large wave, see Chen et al. (2020),

## 1.4 This research

The work involved in this thesis adds to the CFD program ComFLOW. The approach in ComFLOW solves the Navier-Stokes equations which describe the conservation of mass and momentum. The finite volume method on a fixed Cartesian grid is adopted to discretize the governing equations. The structure geometry is described by means of the cut-cell method. For the convection of the free surface, a Volume-of-Fluid (VoF) method improved by a local height function is applied, which ensures the mass conservation.

The project ComFLOW started in the application of liquid sloshing in satellites in zero-gravity circumstances, see Gerrits (2001), and moved to wave motion and hydrodynamic wave loading on offshore structures such as in the work of Fekken (2004) and Kleefsman (2005). The research with maritime and offshore applications was later organized as a joint industry project, headed by the Maritime Research Institute in the Netherlands (MARIN).

Funded by the Dutch technology foundation STW, two PhD students have been employed to work on different aspects of the numerical method. One at the university of Groningen is to develop an efficient numerical scheme for interactively moving bodies. The other at Delft University of Technology works on the hydroelastic response. The third one is funded by China Scholarship Council and her work is presented in this thesis.

## 1.5 Outline

In Chapter 2, the mathematical model that describes the fluid flow is introduced, as well as the discretization of the analytical equations in the numerical modeling. The governing equations are concerned with the conservation of mass, the conservation of momentum and the evolution of the free surface over time.

A detailed discussion on the absorbing boundary conditions (ABCs) accounting for both waves and currents is presented in Chapter 3. Reflection coefficients are chosen to verify the boundary condition. Therefore, theoretical reflection coefficients are derived in an appendix to act as a reference.

The verification results of the ABC with current are included in Chapter 4. The generating and absorbing boundary condition for long-crested dispersive waves with current in this thesis is both accurate for sea states often found in marine environments, and practical to implement in ComFLOW.

Simulation results, validated by experiments, are shown in Chapter 5. The simulations consider a Wigley hull at forward speed in both regular and irregular waves in shallow water. In the experiment, measurements are taken of pitch and heave motions at the center of gravity (CoG) of the ship; the measurements are compared to numerical results at the same locations. In addition, an application of green water impact on the deck of the Wigley hull is demonstrated.

Lastly, to conclude the discussion, observations regarding the approaches and results obtained from the application to ships at forward speed in waves are summarized in Chapter 6, along with several statements with recommendations for future research.



# Chapter 2

## Mathematical and numerical modeling

In this chapter, the mathematical and numerical models that describe fluid flow are presented. The governing equations followed by boundary conditions imposed at solid boundaries, free surface, inflow and outflow boundaries are described in the first section. In subsequent sections, a finite volume discretization of the Navier-Stokes equations on a staggered grid and time integration of the resulting discrete system of equations are provided, as well as a brief introduction of the advection and reconstruction of the free surface and the discrete boundary condition at the free surface.

### 2.1 Mathematical modeling

A homogeneous continuum assumption is used for the fluid flow model. The Navier-Stokes equations, derived from the conservation laws of mass and momentum, are adopted to describe fluid flow in an arbitrary and fixed control volume  $\Omega$  with boundary  $\Gamma$ , see Fig. 2.1. A right-handed Cartesian coordinate system is adopted and the axes are indicated by  $\mathbf{x} = (x, y, z)$ .

#### 2.1.1 Governing equations

The governing equations, which are continuity and momentum equations, are formulated in an integral way in this section, revealing its conservation character.

##### Continuity equation

The continuity equation, indicating that the rate of change of mass in a given control volume is equal to the net flow of mass into the same control volume across its boundaries, is stated as follows:

$$\int_{\Omega} \frac{\partial \rho}{\partial t} d\Omega + \int_{\Gamma} \rho \mathbf{u} \cdot \mathbf{n} d\Gamma = 0, \quad (2.1)$$

where  $\rho$  is the density of the fluid,  $\mathbf{u} = (u, v, w)$  represents the flow velocity in three directions, and  $\mathbf{n}$  denotes the normal vector pointing outwards of the control volume.

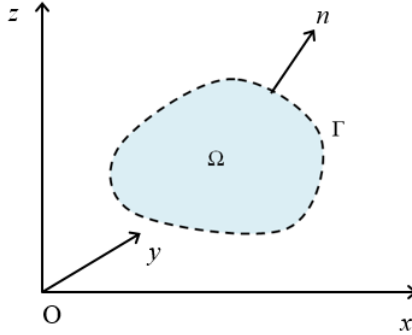


Figure 2.1: Arbitrary volume  $\Omega$  with boundary  $\Gamma$  in a right-handed system

### Momentum equation

The momentum equation in a similar control volume, derived from Newton's second law, states that the rate of increase of momentum of the volume equals the sum of the forces acting on the same volume. It is given as follows:

$$\int_{\Omega} \frac{\partial \rho \mathbf{u}}{\partial t} d\Omega + \int_{\Gamma} \rho \mathbf{u} \mathbf{u} \cdot \mathbf{n} d\Gamma + \int_{\Gamma} p \mathbf{n} d\Gamma - \int_{\Gamma} (\mu(\nabla \mathbf{u} + \nabla \mathbf{u}^T) - 2/3\mu(\nabla \cdot \mathbf{u})I) \cdot \mathbf{n} d\Gamma - \int_{\Omega} \rho \mathbf{f} d\Omega = 0. \quad (2.2)$$

Here the pressure is described by  $p$  and the dynamic viscosity is denoted by  $\mu$ .  $I$  is the unit tensor. The viscosity varies with temperature and less with ambient pressure, but this dependency can be ignored in our applications. Thus, the viscosity is regarded as constant in the remainder of this research.

The external force  $\mathbf{f}$  is a body force acting on the fluid such as gravity:

$$\mathbf{f} = (0, 0, -g)^T, \quad (2.3)$$

in which  $g$  is the gravitational acceleration.

In this work one-phase flow (water only) is considered, therefore, the continuity equation (2.1) and momentum equation (2.2) can be simplified. Since water is treated as incompressible with constant density, we have  $\partial \rho / \partial t = 0$ .

Substituting the above relation in Eq. (2.1) and (2.2), the continuity and momentum equation reduce to, respectively:

$$\int_{\Gamma} \mathbf{u} \cdot \mathbf{n} \, d\Gamma = 0 \quad (2.4)$$

$$\int_{\Omega} \frac{\partial \mathbf{u}}{\partial t} \, d\Omega + \int_{\Gamma} \mathbf{u}\mathbf{u} \cdot \mathbf{n} \, d\Gamma + \frac{1}{\rho} \int_{\Gamma} p\mathbf{n} \, d\Gamma - \nu \int_{\Gamma} \mathbf{n} \cdot \nabla \mathbf{u} \, d\Gamma - \int_{\Omega} \mathbf{f} \, d\Omega = 0, \quad (2.5)$$

where  $\nu$  is the kinematic viscosity  $\nu = \mu/\rho$ . Because of incompressibility, it is not required to solve a conservation law for energy in an additional equation.

### Free surface equation

In our application, the interface between water and air is of great interest. This interface is known as free surface. As the flow is considered incompressible, the evolution of the free surface,  $S(\mathbf{x}, t) = 0$ , in space and time satisfies:

$$\frac{\partial S}{\partial t} + \nabla \cdot (\mathbf{u}S) = 0. \quad (2.6)$$

### 2.1.2 Boundary conditions

To obtain a solution to the system of partial differential equations describing fluid flow, as shown in the previous section, boundary conditions are necessary. Now the boundary conditions, imposed on various boundaries that may be encountered in a domain, are explained.

#### Solid boundary

At solid boundaries, no-slip or free-slip conditions can be chosen. In the simulations presented in this thesis, a free-slip condition has been adopted at the outer domain walls, as it allows us to use a coarser computational grid near the outer walls. Along the surface of the (moving) objects a no-slip condition  $\mathbf{u} = \mathbf{u}_b$  has been chosen, where  $\mathbf{u}_b$  is the velocity of the object. To resolve the resulting viscous boundary layer, the grid has been locally refined. For more details about the local grid refinement, please refer to van der Plas (2017).

#### Free surface

At the free surface, the normal and tangential forces are balanced and this is imposed by the following conditions:

$$\mu \left( \frac{\partial u_n}{\partial \tau} + \frac{\partial u_\tau}{\partial n} \right) = 0 \quad (2.7)$$

$$-p + 2\mu \frac{\partial u_n}{\partial n} = -p_0 + \sigma \kappa, \quad (2.8)$$

Here the indices  $n$  and  $\tau$  denote the normal and tangential direction, respectively. The curvature of the free surface and surface tension are represented by  $\kappa$  and  $\sigma$ , respectively, while  $p_0$  is the atmospheric pressure.

### Inflow and outflow boundaries

The conditions applied at the inflow and outflow boundaries have already been developed in the ComFLOW project. They allow (only) waves to move into and out of the computational domain simultaneously, which are called Generating and Absorbing Boundary Conditions (GABC). These form the basis of this research. Here the GABC will be briefly introduced, and the readers are referred to Wellens (2012), Duz (2015) and Wellens and Borsboom (2020) for detailed implementation of the GABC in ComFLOW. The GABC extended for both waves and currents, which is the main topic of this research, will be derived in Chapter 3.

Since we are looking at the waves and the waves are well described by potential theory, the inflow and outflow boundary conditions in this thesis are derived from potential theory. The potential theory for waves is introduced as follows.

**Potential theory** In this work, a constant and uniform current  $\mathbf{U}$ , independent of position and time and propagating in the  $x$ -direction, is added into potential flow. The concept of irrotationality allows for the introduction of a potential function  $\phi$ , whose spatial derivative yields the velocity in the direction of the derivative. Superimposing undisturbed waves and currents, the following relation holds for the potential:

$$\nabla\phi = \nabla(\phi_w + \mathbf{U} \cdot \mathbf{x}) = \mathbf{u}_w + \mathbf{U} = \mathbf{u}, \quad (2.9)$$

where  $\phi_w$  and  $\mathbf{u}_w$  are the potential and velocity attributed to waves.

Many flow types may be considered as irrotational and the use of the potential leads to a reduced set of equations that in some instances can be solved analytically for these flow types. With the potential the continuity equation becomes:

$$\nabla^2\phi = 0. \quad (2.10)$$

After substitution of the relation (2.9) into the momentum equation (2.2) and integration along the domain boundary, the momentum equation (2.2) becomes the unsteady Bernoulli equation:

$$\frac{\partial\phi}{\partial t} + \frac{1}{2} |\nabla\phi|^2 + \frac{p}{\rho} - F = C, \quad (2.11)$$

in which  $F$  is the external force potential  $-gh$  at the free surface and  $C$  is an integration constant.

**Absorbing boundary conditions** In this discussion, it will be highlighted what is considered to be important for the design of an absorbing boundary condition (ABC) in ComFLOW. It has been clearly stated in the work of Wellens (2012):

- *The stability of the system of equations inside the domain should not be affected by the ABC.*
- *The reflection caused by the ABC should not exceed 5 %. In practical simulations, five percent reflection for wave components within the frequency band where most of the wave energy resides in the spectrum is an acceptable level of accuracy.*
- *The boundaries where the ABC is defined, are to be truly open boundaries, i.e. transparent to incoming and outgoing waves simultaneously.*
- *The ABC has to absorb ship generated waves at the domain boundaries.*
- *The computational resources to prevent reflection should be marginal compared to the computational effort to determine the solution itself.*
- *The ABC needs to be formulated on a rectangular, Cartesian grid domain.*

In Chapter 3 we will work out these requirements in more detail.

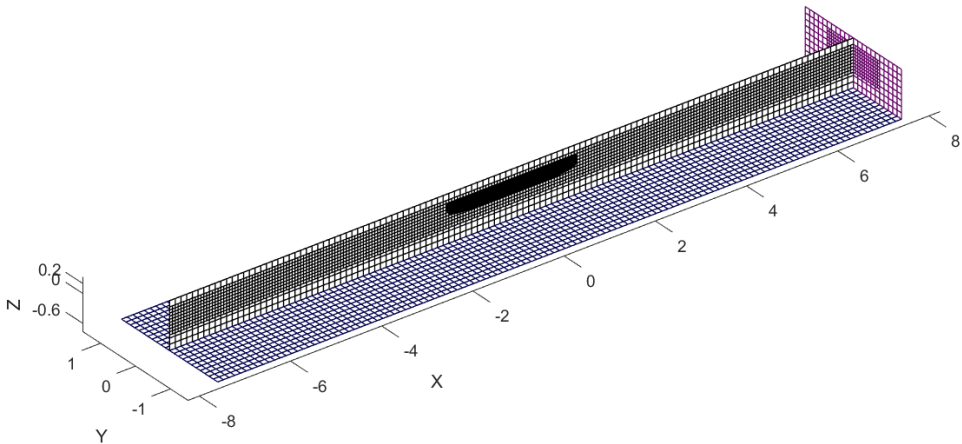


Figure 2.2: Illustration of the local grid refinement in the simulation setup. For visualization purposes the grid is depicted at a one time coarser resolution

## 2.2 Computational domain and grid

In ComFLOW the governing equations, including the continuity and momentum equations, for fluid flow are discretized on finite control volumes in the computational domain. The domain  $\Omega$  is rectangular. It is covered with a Cartesian grid, that is fixed and structured. A hierarchical grid refinement procedure is implemented in the program, in which grid cells are split in a set of smaller grid cells upon satisfying a certain refinement criterion. The goal of local grid refinement is to concentrate

grid nodes in those areas of the solution domain that are under-resolved in order to increase the accuracy of the solution with as little effort as possible. Local grid refinement provides an efficient tool to capture more details around boundaries where the solution has large gradients. Fig. 2.2 illustrates a setup of local grid refinement in the simulation of a Wigley hull at forward speed in head waves, where local grid refinement is applied around the hull. The reader is referred to van der Plas (2017) for more details on local grid refinement.

The flow variables  $\mathbf{u} = (u, v, w)$  and  $p$  are positioned in a grid cell using a staggered grid arrangement. The velocity components are located at the face centers of the grid cell while the pressure is defined at the center of the grid cell. The staggered arrangement gets rid of an irregular checker-board pressure field that can be observed in collocated grids, in which the velocities are defined at the same positions as the scalar variables such as pressure.

A cut-cell approach, see Droge and Verstappen (2005), is adopted to represent impermeable structures within the domain, where the geometry intersects with the grid. The intersection produces cells that are filled with both fluid and geometry simultaneously. In comparison with the staircase description of a geometry, the cut-cell method is more accurate. In addition, it has the same flexibility as the boundary-fitted unstructured grid. To explain the framework clearly, a typical cut-cell is shown in Fig. 2.4. Part of the cut-cell is filled with water and the other part is occupied by a section of the structure.

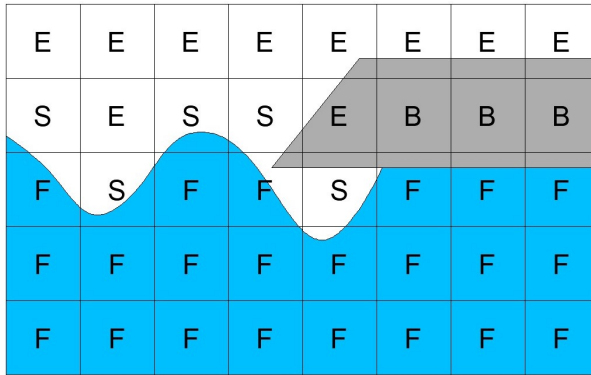


Figure 2.3: Labels identifying **E**mpy cells, **S**urface cells, **F**luid cells and **B**oundary cells

The volume aperture  $F^b$  represents the proportion of the cell volume  $\Delta x \Delta z$  that is open to flow. This implies that the volume aperture taken by the object is  $(1 - F^b)$ . Where the structure cuts through a cell face, the edge apertures  $A^x$ ,  $A^z$  (and  $A^y$  in 3D) are measures of the portion of the cell faces open to flow.

Based on the structure and the fluid configuration, the similar cells that call for similar processing are identified through a labelling system. It is visualized in Fig.

2.3. Cells are labelled in a distinct order. First, **Empty** cells that contain no fluid are identified. Subsequently, the non-empty cells bordering the Empty cells are labeled as **Surface** cells, which are thought to contain the free surface. Lastly, the remaining cells are selected as **Fluid** cells which are neighbours to Surface and Fluid cells. The ones that are completely occupied by the structure are labeled as **Boundary** cells. The cell labelling process is carried out at each time step to update the labels across the domain.

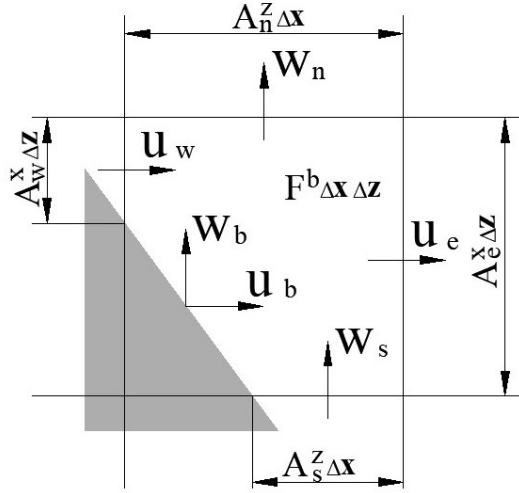


Figure 2.4: Representation of a cut-cell containing both the fluid and the structure. It is also a control volume for the continuity equation.

## 2.3 Continuity equation

In this section, the continuity equation, as well as momentum equations later, will only be discussed in 2D for clarity. In the control volume for the continuity equation, see Fig. 2.4, the velocities are moved to the center of the part of the cell face open to flow. The mass flux over the western cell face is  $\mathcal{F}_w = u_w A_w^x \Delta z$ . The same applies to the eastern, northern and southern faces. By summing all flux contributions, the continuity equation is discretized as follows:

$$(u_e A_e^x - u_w A_w^x - u_b(1 - A_w^x))\Delta z + (w_n A_n^z - w_s A_s^z - w_b(1 - A_s^z))\Delta x = 0. \quad (2.12)$$

where  $u_b$  and  $w_b$  are the velocities of the moving object in  $x$ - and  $z$ -direction, respectively.

## 2.4 Momentum equation

The momentum equation for the incompressible flow is re-stated as follows:

$$\int_{\Omega} \frac{\partial \mathbf{u}}{\partial t} d\Omega + \oint_{\Gamma} \mathbf{u}(\mathbf{u} \cdot \mathbf{n}) d\Gamma - \nu \oint_{\Gamma} \mathbf{n} \cdot \nabla \mathbf{u} d\Gamma + \frac{1}{\rho} \oint_{\Gamma} p \mathbf{n} d\Gamma - \int_{\Omega} \mathbf{f} d\Omega = 0. \quad (2.13)$$

To discretize the time derivative term in space on a staggered control volume, see Fig, 2.5, the midpoint rule is applied:

$$\int_{\Omega} \frac{\partial u}{\partial t} d\Omega = \frac{\partial u_c}{\partial t} \frac{F_w^b \Delta x_w + F_e^b \Delta x_e}{2} \Delta z. \quad (2.14)$$

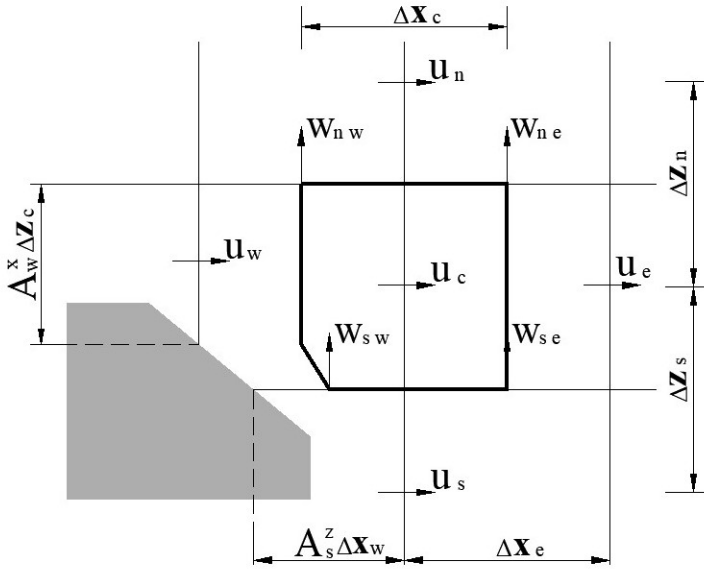


Figure 2.5: Control volume for the convective term

### 2.4.1 Convection

The convective term in the  $x$ -direction is:

$$\oint_{\Gamma} u(\mathbf{u} \cdot \mathbf{n}) d\Gamma. \quad (2.15)$$

Note the distinction between the convected quantity  $u$  and the convecting mass flux  $(\mathbf{u} \cdot \mathbf{n}) d\Gamma$ .

For the discretization of the convection term, fluxes over the faces of the control

volume in Fig. 2.5 have to be calculated. For the convecting mass flux at the western face of the control volume:

$$\mathcal{F}_w^m = \frac{1}{2}(u_c A_c^x + u_w A_w^x) \Delta z. \quad (2.16)$$

Taking the convected quantity  $u$  at the western face into account, the convective flux over the western face of the control volume is obtained:

$$\mathcal{F}_w^c = \frac{1}{2} \mathcal{F}_w^m (u_w + u_c) + \frac{1}{2} \alpha |\mathcal{F}_w^m| (u_w - u_c). \quad (2.17)$$

When  $\alpha = 0$  a second-order central discretization is obtained, which is energy preserving, see Verstappen and Veldman (2003). When  $\alpha = 1$  a first-order upwind scheme is applied by means of Eq. (2.17).

For brevity, the convective mass flux over the eastern, northern and southern faces of the control volume will not be given in detail.

### 2.4.2 Diffusion

The discretization of the diffusion term is based on the work of van der Heiden (2019). The diffusion term in the horizontal direction of the control volume of Fig. 2.5 is:

$$-\nu \oint_{\Gamma} \mathbf{n} \cdot \nabla u dS. \quad (2.18)$$

The viscous stresses are discretised at the faces of the control volume.

In cut-cells the discretization of the diffusive term is not trivial, since boundary conditions should be imposed at a position that is immersed in the grid cells.

In the 2-D situation, a boundary immersed in the cell is represented by a straight line segment which is determined by the cell face apertures. The immersed boundary makes the control volume not necessarily rectangular. Some typical deformation are shown in Fig. 2.6 . As can be observed, the control volume extends over two cells.

### 2.4.3 viscous normal stress

The finite volume discretization of the diffusion term requires the evaluation of the boundary integral at the right-hand side of Eq. (2.18).

Considering the situation on the right of Fig. 2.6 and applying Gauss' divergence theorem:

$$\int_{\Omega} \nabla \cdot \mathbf{u} d\Omega = \oint_{\Gamma} \mathbf{n} \cdot \mathbf{u} dS, \quad (2.19)$$

to the western continuity cell  $\Omega_w$  yields the equality (compare (2.12)):

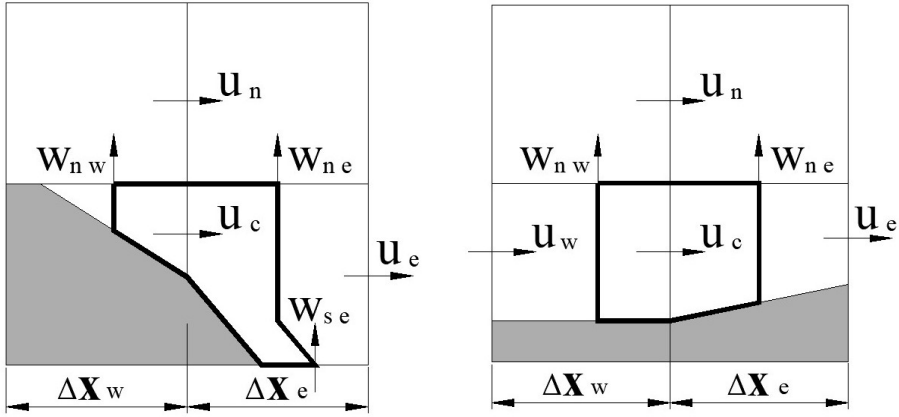


Figure 2.6: Two typical examples of the momentum control volume in 2-D cut cells

$$\left( \frac{\partial u}{\partial x} \Big|_w + \frac{\partial w}{\partial z} \Big|_w \right) |\Omega_w| = [A_c^x u_c - A_w^x u_w + A_{nw}^x w_{nw} + (A_w^x - A_c^x) u_b - A_{nw}^z w_b] \Delta z. \quad (2.20)$$

Then the discretization of the viscous normal stress  $\frac{\partial u}{\partial x}$  can be obtained from the above equation as:

$$\frac{\partial u}{\partial x} \Big|_w = \frac{A_c^x u_c - A_w^x u_w + (A_w^x - A_c^x) u_b}{|\Omega_w| / \Delta z_c}. \quad (2.21)$$

The viscous normal stress contribution of the western and eastern cell faces to the diffusion term in (2.18) can be calculated similar to the face integral for the pressure balance (2.26). For convenience, we will explain this procedure in detail in the next subsection, where it leads to the discretization of the pressure gradient (2.27). Here we merely give the result as:

$$\oint_{\Gamma} n_x \frac{\partial u}{\partial x} dS = A_c^x \left( \frac{\partial u}{\partial x} \Big|_e - \frac{\partial u}{\partial x} \Big|_w \right) \Delta z_c. \quad (2.22)$$

#### 2.4.4 Shear stress

The shear stress contribution at the right-hand side of Eq. (2.18) is described as:

$$\oint_{\Gamma} n_z \frac{\partial u}{\partial z} dS = \frac{\partial u}{\partial z} \Big|_n \Delta S_n - \frac{\partial u}{\partial z} \Big|_s \Delta S_s. \quad (2.23)$$

The shear stresses are calculated at 1) the northern boundary where the shear stress position coincides with a vertex of the grid cell, 2) the southern boundary where the

control volume coincides with the immersed boundary. These are the only two possibilities that can occur in a 2-D case.

The gradient at the northern face is evaluated as:

$$\left. \frac{\partial u}{\partial z} \right|_n = \frac{u_n - u_c}{\frac{1}{2}(A_c^x \Delta z_c + A_n^x \Delta z_n)}. \quad (2.24)$$

The velocity gradient at the southern face is evaluated as:

$$\left. \frac{\partial u}{\partial z} \right|_s = \frac{u_c - u_b}{\frac{1}{2}A_c^x \Delta z_c}. \quad (2.25)$$

Additionally, the discretization of the shear stress requires a choice for  $\Delta S_n$  (the integration area in the northern part of the control volume) and  $\Delta S_s$  (the southern part of the control volume). The northern shear stress is integrated over  $\Delta S_n = \frac{1}{2}(A_{nw}^z \Delta x_w + A_{ne}^z \Delta x_e)$ . The southern integration area  $\Delta S_s = \frac{1}{2}(A_{sw}^z \Delta x_w + A_{se}^z \Delta x_e)$  requires integration over the immersed boundary of the control volume. More details have been discussed in Droge and Verstappen (2005) and van der Heiden (2019).

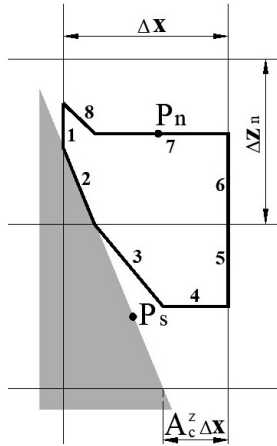


Figure 2.7: Control volume for the pressure term.  $p_n$  is the pressure acting on the segments 2, 7 and 8, and  $p_s$  is exerting on the segment 3 and 4

### 2.4.5 Pressure

The pressure term in the  $z$ -direction needs to be summed over the faces of the control volume in Fig. 2.7 as follows:

$$\oint_{\Gamma} p n_z d\Gamma = \sum_j \oint_j p_j n_{zj} d\Gamma, \quad (2.26)$$

in which  $-1/\rho$  is ignored and  $n_z$  is the outward pointing normal of the north and

south boundary of the control volume.

The pressure is assumed to be constant within a cell,  $p = p_s$  holds for the faces 3, 4 and 5 while  $p = p_n$  holds for 1, 2, 6, 7 and 8. It is observed that the faces 1, 5 and 6 do not give contribution to the integral since  $n_y = 0$  over them. Moreover, the faces 2 and 8 cancel each other because they have the same pressure value but their contributions  $n_y d\Gamma = dx$  have opposite signs. Therefore, only the contributions of the faces 3, 4 and 7 remain as follows:

$$\oint_{\Gamma} pn_z d\Gamma = \oint_{\Gamma_7} pn_z d\Gamma + \oint_{\Gamma_{3+4}} pn_z d\Gamma = \oint_{\Gamma_7} p dx + \oint_{\Gamma_{3+4}} p dx = (p_n - p_s) A_c^z \Delta x, \quad (2.27)$$

which depends on the open part of the central face of the control volume. The exact position of the geometry does not have effects here.

The gravity term, which is the only external force in our applications, can be discretized similarly to the pressure. By means of Gauss' theorem the volume integral of the gravity term,  $\int_{\Omega} -g d\Omega$ , can be transformed to a surface integral along the boundary of the control volume in Fig. 2.7:

$$\int_{\Omega} -g d\Omega = \int_{\Omega} \nabla(-gz) d\Omega = \oint_{\Gamma} -gz n_x d\Gamma. \quad (2.28)$$

Similar to (2.27), the integral of the gravity term over all the faces of the volume is written eventually as:

$$\oint_{\Gamma} -gz n_x d\Gamma \approx -g A_c^z \Delta x (z_n - z_s) = -g A_c^z \Delta x \Delta z, \quad (2.29)$$

where  $z_n$  and  $z_s$  represent the center positions of the northern and southern cells in the  $z$ -direction.

## 2.5 Time Integration

The fluxes discussed above, including mass, convective, diffusion, pressure and gravity fluxes, can be formulated as matrix coefficients multiplied by vectors containing the discrete solution variables.

For the discrete continuity equation, the divergence matrix  $\mathcal{M}$  can be described as:

$$\mathcal{M} \mathbf{u}_h = 0, \quad (2.30)$$

in which  $\mathbf{u}_h$  contains the discrete velocities.

For the terms in the discrete momentum equation, a convective matrix  $\mathcal{C}$ , a diffusive matrix  $\mathcal{D}$  and a gradient matrix  $\mathcal{G}$  are defined. The discrete momentum equation can further be rewritten as:

$$\mathcal{V} \frac{\partial \mathbf{u}_h}{\partial t} = -\mathcal{C}(\mathbf{u}_h) \mathbf{u}_h + \nu \mathcal{D} \mathbf{u}_h - \frac{1}{\rho} \mathcal{G} \mathbf{p}_h + \mathbf{f}_h, \quad (2.31)$$

in which  $\mathcal{V}$  is a diagonal matrix containing the control volume size, the notation  $\mathcal{C}(\mathbf{u}_h)$  shows that it is a nonlinear term, the vector  $\mathbf{p}_h$  contains the discrete pressure and  $\mathbf{f}_h$  accounts for the discrete gravity. For the purpose of energy preservation, the pressure forces should not contribute to the energy balance. Therefore, the discrete pressure gradient  $\mathcal{G}$  has to be related to the discrete mass equation, i.e.  $\mathcal{G} = -\mathcal{M}^T$ .

The temporal discretization is accomplished by means of explicit forward Euler in time. The velocities in the convective and diffusive terms are chosen at the old time level  $t^n$ , while in the continuity equation the velocities are selected at the new time level  $t^{n+1}$  to make sure that the velocity field at this level is divergence free. Correspondingly, the pressure has to be calculated at the new time level as well, due to the incompressibility of fluid.

Adding the superscripts indicating the time level to the solution variables and employing the relation  $\mathcal{G} = -\mathcal{M}^T$ , the equations are written as:

$$\mathcal{M} \mathbf{u}_h^{n+1} = 0 \quad (2.32)$$

$$\mathcal{V} \frac{\mathbf{u}_h^{n+1} - \mathbf{u}_h^n}{\Delta t} = -\mathcal{C}(\mathbf{u}_h^n) \mathbf{u}_h^n + \nu \mathcal{D} \mathbf{u}_h^n - \frac{1}{\rho} \mathcal{M}^T \mathbf{p}_h^{n+1} + \mathbf{f}_h^n. \quad (2.33)$$

An auxiliary vector  $\tilde{\mathbf{u}}_h$ , containing the contributions of convection, diffusion and gravity at the old time level, is introduced:

$$\tilde{\mathbf{u}}_h^n = \mathbf{u}_h^n - (\mathcal{C}(\mathbf{u}_h^n) \mathbf{u}_h^n - \nu \mathcal{D} \mathbf{u}_h^n - \mathbf{f}_h^n). \quad (2.34)$$

With this auxiliary velocity  $\tilde{\mathbf{u}}_h$ , the discrete momentum equation (2.33) becomes:

$$\mathbf{u}_h^{n+1} = \tilde{\mathbf{u}}_h^n - \Delta t \mathcal{V}^{-1} \frac{1}{\rho} \mathcal{M}^T \mathbf{p}_h^{n+1}. \quad (2.35)$$

Substitution of the momentum equation into the continuity equation and rearranging terms result in a discrete Poisson equation for the pressure:

$$\mathcal{M} \mathcal{V}^{-1} \mathcal{M}^T p_h^{n+1} = \frac{\rho}{\Delta t} \mathcal{M} \tilde{\mathbf{u}}_h^n. \quad (2.36)$$

The pressure at the new time level  $p_h^{n+1}$  in the above equation can be solved with a linear solver. A Bi-CGSTAB solver with an incomplete LU preconditioner has been adopted in this work. The solution  $p_h^{n+1}$  in the system (2.36) is used to calculate the velocities  $\mathbf{u}_h^{n+1}$  from Eq. (2.35).

## 2.6 Stability

The evolution of the kinetic energy is employed to investigate the stability of spatial discretization, see Verstappen and Veldman (2003). More details have also been discussed in Fekken (2004) and Kleefsman (2005).

The convective time integration stability for first-order upwind discretization on uncut cells is satisfied by the CFL criterion, see Droge and Verstappen (2005):

$$\left| \frac{u}{\Delta x} + \frac{v}{\Delta y} + \frac{w}{\Delta z} \right| \Delta t \leq 1. \quad (2.37)$$

The CFL condition should also be guaranteed in the propagation of waves, in which the velocity is wave celerity.

The diffusive criterion on uncut cells can be met through:

$$2\nu \left( \frac{1}{\Delta x^2} + \frac{1}{\Delta y^2} + \frac{1}{\Delta z^2} \right) \Delta t \leq 1. \quad (2.38)$$

For all stability conditions mentioned above, the time step is automatically adjusted to meet them in ComFLOW.

## 2.7 Interaction with a moving body

The interaction with a moving object is based on the work of Veldman et al. (2017, 2018). In our applications a Wigley hull is advancing in head waves. Its dynamics have to be determined interactively with the wave dynamics. Therefore, coupling conditions are required at their common interface (see Fig. 2.8), including the acceleration of the solid body  $\dot{\mathbf{u}}_b$  and the integrated pressure force  $\mathbf{f}_\Gamma$  acting on the object. Here the viscous stresses are neglected. The coupling conditions are formulated as:

$$\mathbf{u} = \mathbf{u}_b \quad \text{and} \quad \mathbf{f}_\Gamma = \int_\Gamma p \mathbf{n}_b \, d\Gamma \equiv Bp, \quad (2.39)$$

where  $B$  is a non-sparse matrix corresponding with the pressure integration over the body.

The equations of fluid flow can be formulated in an abstract and simplified way as:

$$\mathbf{f}_\Gamma = -M_a \dot{\mathbf{u}}_b. \quad (2.40)$$

Here  $M_a$  represents the so-called added mass operator, which describes the fluid response to the acceleration of the structure. The term  $\mathbf{f}_\Gamma$  also contains a gravitational force, but it is omitted for simplicity of presentation.

The dynamics of the structure are described as:

$$M_b \dot{\mathbf{u}}_b = \mathbf{f}_\Gamma, \quad (2.41)$$

in which  $M_b$  is the mass operator formed from a 6-DOF model.

**Quasi-simultaneous coupling** In this work, the equations of fluid flow (2.40) and the dynamics of the structure (2.41) are coupled in a quasi-simultaneous way, see Veldman (1981, 2009). In this approach, the dynamics of the solid body is approximated and then solved simultaneously with the equations of fluid flow. In particular, an approximation  $\widetilde{M}_b^{-1}$  of the inverse of the structural mass operator in Eq. (2.41) is introduced, which is called interaction law. In the iterative process this interaction law is employed as:

$$\dot{\mathbf{u}}_b^{new} - \widetilde{M}_b^{-1} \mathbf{f}_\Gamma^{new} = M_b^{-1} \mathbf{f}_\Gamma^{old} - \widetilde{M}_b^{-1} \mathbf{f}_\Gamma^{old} \quad \text{Interaction law} \quad (2.42)$$

$$\mathbf{f}_\Gamma^{new} + M_a \dot{\mathbf{u}}_b^{new} = 0. \quad \text{fluid} \quad (2.43)$$

In our implementation, the superscripts  $\cdot^{old}$  and  $\cdot^{new}$  correspond with the old time level  $n$  and new time level  $n + 1$ , but they can also relate to (sub)iterations within one time step.

The case  $\widetilde{M}_b^{-1} = 0$  corresponds to the usual weak coupling process, which can be written as:

$$\mathbf{f}_\Gamma^{new} = -M_a M_b^{-1} \mathbf{f}_\Gamma^{old}. \quad (2.44)$$

From the mathematical perspective, these iterations converge if and only if the spectral radius of the iteration matrix  $\rho(M_a M_b^{-1}) < 1$ . Physically, this means that the solid body should be heavy enough compared to the fluid added mass. If it is not, underrelaxation can help to achieve convergence, but this will require additional and costly (sub)iterations.

In the quasi-simultaneous approach iterative process (2.42) and (2.43) can be condensed to:

$$(I + M_a \widetilde{M}_b^{-1}) \mathbf{f}_\Gamma^{new} = -M_a (M_b - \widetilde{M}_b^{-1}) \mathbf{f}_\Gamma^{old}, \quad (2.45)$$

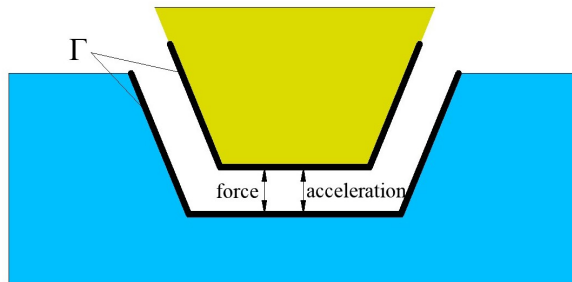


Figure 2.8: Information exchange over the common interface  $\Gamma$  between fluid and solid body in a partitioned way

where  $I$  is the unit operator. In comparison with Eq. (2.44), the addition of the approximate structure operator  $\widetilde{M}_b^{-1}$  makes the left-hand side 'larger' and the right-hand side 'smaller', thus improving the convergence. If the interaction law is chosen equal to the full structure operator  $M_b^{-1}$ , the right-hand sides in Eq. (2.42) and (2.45) vanish which makes the coupling process immediate.

**Implementation** Realizing that  $\mathbf{f}_\Gamma = Bp$ , the interaction law (2.42) is a relation between the pressure  $p$  and the velocity  $\mathbf{u}_b$  over the structure surface. This relation can be substituted into the boundary condition  $\mathbf{u} = \mathbf{u}_b$ , which enters the divergence expression  $\mathcal{M}\mathbf{u}$  in Eq. (2.30). This  $\mathcal{M}$  is the divergence operator from the continuity equation, while the other  $M$ 's in this section are mass matrices. It ends up with the pressure Poisson equation (2.36) and thus forms a boundary condition for the pressure. It can be shown that the Poisson equation keeps its favourable numerical properties such that its iterative solution can proceed as before. More details are given in Veldman et al. (2017, 2018).

## 2.8 Free surface

After the velocity and pressure field are calculated, the free surface will be displaced by the Volume of Fluid (VoF) method. The VoF function is a discrete function with values between 0 and 1 in each cell, indicating the fraction of the cell which is open to fluid. The displacement of the free surface at each time step is performed according to Eq. (2.6).

The VoF method was originally introduced by Hirt and Nichols (1981). The most well-known drawback of the VoF method is the problem of flotsam and jetsam that are small droplets of fluid disconnecting from the free surface. Another disadvantage is that mass is not exactly conserved in the domain although in theory VoF is mass conserving (in contrast to the level set method). Due to rounding off the VoF values at the end of the displacement, water can be gained or lost. One way to prevent these problems is the use of a local height function. More detailed information has been given in Fekken (2004), Wellens (2012) and Duz (2015).

The original VoF method does not resolve the free surface explicitly. However, the exact position of the free surface is important in our application and thus an appropriate reconstruction of the free surface is necessary. In ComFLOW, the piecewise linear interface calculation (PLIC) approach is employed, such as in Fekken (2004) and Duz (2015), in which the free surface orientation is not necessarily grid aligned. It is a much better approximation of the free surface than the simple line interface calculation (SLIC) method where the free surface is kept grid aligned, which leads to the problem of flotsam and jetsam, see Kleefsman (2005) and Wellens (2012).

### 2.8.1 Boundary conditions at the free surface

As shown above, governing equations for the fluid flow are discretized by means of numerical approaches implemented in ComFLOW. To complete the stencil, conditions at the boundaries of the domain need to be discretized as well.

In the applications presented in this thesis, the free slip condition is adopted at domain walls. At the (moving) boundaries of the structures, the no-slip condition, i.e.  $\mathbf{u} = \mathbf{u}_b$ , is applied. Therefore, velocities at faces between Boundary and Fluid cells (FB) are set equal to the velocity of the object. Discretization of inflow and outflow boundary conditions are discussed in detail in Chapter 3. Here a brief introduction of the numerical boundary conditions for velocities and pressures at the free surface is presented.

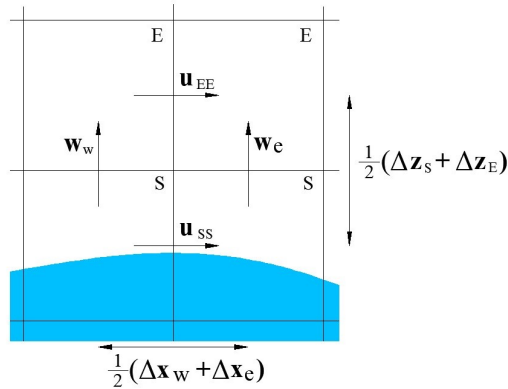


Figure 2.9: Calculation of EE velocity at the free surface

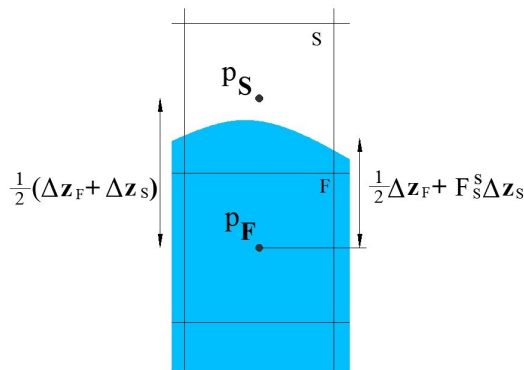


Figure 2.10: Calculation of the pressure for Surface cells at the free surface

## 2.8.2 Discrete velocities at the free surface

As shown in Fig. 2.3, the velocities which are solved in the momentum equations are located at the cell faces between two neighbouring cells, containing two Fluid cells (FF), Fluid and Surface cells (FS), and two Surface cells (SS). Boundary conditions, which are velocities between neighbouring Surface and Empty cells (SE) and two Empty cells (EE) are required for the calculation of SS velocities.

SE velocities are obtained by constant or linear extrapolation from the velocities inside the fluid. The comparison between these two extrapolation is investigated in detail by Fekken (2004), Kleefsman (2005) and Wellens (2012).

EE velocities are calculated according to the balance of normal and tangential stress at the free surface, as shown in Eq. (2.8). When the orientation of the free surface is (almost) horizontal, SS and EE velocities are in  $x$ -direction and SE velocities are in  $z$ -direction, see Fig. 2.9. The condition is adopted as follows:

$$\frac{\partial u}{\partial z} + \frac{\partial w}{\partial x} = 0. \quad (2.46)$$

A central difference scheme is used to discretize the above condition as:

$$u_{EE} = u_{SS} - \frac{\Delta z_S + \Delta z_E}{\Delta x_w + \Delta x_e} (w_e - w_w). \quad (2.47)$$

## 2.8.3 Discrete pressures at the free surface

The pressure in Surface cells is required as the boundary condition and can be obtained by interpolation of the pressure at the free surface and the pressure in a neighbouring Fluid cell. The pressure at the free surface is determined from the boundary condition shown in Eq. (2.10), which represents the continuity of normal stress at the free surface. In our applications, the surface tension and viscosity in the boundary condition (2.10) can be neglected, which results in the pressure at the exact position of the free surface  $p_{fs}$  equalling the atmospheric pressure  $p_0$ .

The pressure in Surface cells  $p_S$  is now calculated from  $p_{fs}$  and the pressure in a neighbouring Fluid cell  $p_F$ . If the free surface is mainly horizontal, shown as in Fig. 2.10, the Fluid cell below the Surface cell is adopted for the interpolation. The pressure at the center of the Surface cell is calculated as:

$$p_S = \beta p_{fs} + (1 - \beta) p_F, \quad (2.48)$$

in which  $\beta = (\Delta z_F + \Delta z_S) / (\Delta z_F + F_S^s \Delta z_S)$ . If no Fluid cells exist adjacent to the Surface cell, the pressure in the Surface cell is prescribed as the atmospheric pressure, corrected with a hydrostatic pressure contribution based on the local height of the fluid.

# Chapter 3

## ABCs with uniform current

In this chapter, the first-order generating and absorbing boundary condition and the second-order absorbing boundary condition for waves are derived. They are extended to include the effect of uniform current. This is the main objective of the thesis. Subsequently, the discretization of the boundary conditions and implementation in the program ComFLOW are presented.

### 3.1 Absorbing boundary conditions

The prevention of wave reflection at the domain boundaries is vital to keep the flow field inside the domain from being disturbed. Damping zones have often been adopted to dissipate wave energy in numerical simulations. They are effective for short wave components, while for long wave components quite a length, usually more than two wave lengths, is required. For long-crested wave simulations, it may still be acceptable in the 2D domain, however, it can become infeasible in the 3D case with the computer memory at one's disposal.

Absorbing boundary conditions (ABCs), also known as non-reflecting boundary conditions, are another type of technique to prevent wave reflection. ABCs can be categorised into two types: global and local ABCs. The discrete global ABC operator necessitates the storage of all previous time steps, as well as the processing of all spatial grid points at each time step, which makes it generally accurate but computationally expensive and difficult to carry out, see Tsynkov (1998) and Wellens (2012). On the contrary, local ABCs, which are local in time, are less accurate but more economical and effortless to implement. The ABC studied in this work belongs to the local type.

Fourier transform of the planar wave equation can be used to derive the local ABC, see Engquist and Majda (1977). This procedure has also been summarized by Wellens (2012). The first-order approximation of the dispersion relation yields the first-order ABC, and the higher-order approximation gives higher derivatives in the ABC with which waves propagating at different directions are accurately absorbed, see Higdon

(1986).

To account for the dispersive properties of waves, the higher-order ABC mentioned above is one of the approaches, because it contains a couple of phase speeds that together span a range. An alternative is the use of a low-order boundary condition in combination with an estimate of the actual celerity at the boundary, see Orlanski (1976). A dynamic approximation of the phase speed obtained from the solution itself is employed:

$$c = -\frac{\partial\phi/\partial t}{\partial\phi/\partial x}. \quad (3.1)$$

When the denominator in the above relation becomes zero, the value of  $c$  can get infinitely large and thus lead to an unstable solution field. This approach should not be adopted.

Blayo and Debreu (2005) consider open boundary conditions from the point of view of characteristic variables. This approach separates the incoming and outgoing flow quantities. The method of characteristic variables is also employed by Verboom and Slob (1984).

Other researchers derive absorbing boundary conditions by factoring the wave equation into components which represent the incoming and outgoing wave fields. The components that prescribe the incoming wave field are then used to design the absorbing boundary condition. This strategy was used by Lindman (1975) for the 2-D acoustic equation and by Engquist and Majda (1977) for the acoustic and elastic wave equations. Clayton and Engquist (1980) later extended these results to the one-way wave equation for migration.

Keys (1985) decomposed the wave equation in a somewhat different way from the previous factorization. His decomposition leads to local absorbing boundary conditions obtained directly from the outgoing components of the wave field. It is not necessary to approximate the outgoing components of the wave field, as is the case with the usual decomposition of the wave equation. As the derivation of the ABC in this thesis has been inspired by this approach, it will be discussed in the next section.

The approach to deal with the wave dispersion in this thesis will be presented in Section 3.4.

## 3.2 Factorization of the wave equation

The planar wave equation is factorized into the individual components representing incoming and outgoing waves respectively, see Keys (1985). The outgoing wave component is adopted to design an absorbing boundary condition.

We will study waves with a two-dimensional wave number vector  $\mathbf{k} = (k_x, k_y)$ , whose

length is denoted by  $k \equiv |\mathbf{k}| = \sqrt{k_x^2 + k_y^2}$ . The wave number components  $k_x$  and  $k_y$  can be complex valued to distinguish between propagating and evanescent/spurious waves. This means that its length  $|\mathbf{k}|$  can also be a complex number. The unit vector in the wave direction  $\mathbf{k}$  is represented by  $\mathbf{e}_k$ .

With the unit vector  $\mathbf{e}_k$ , the planar wave equation can be factorized as follows:

$$\nabla^2 \phi - \frac{1}{c^2} \frac{\partial^2 \phi}{\partial t^2} = \left( \nabla + \frac{\mathbf{e}_k}{c} \frac{\partial}{\partial t} \right) \left( \nabla - \frac{\mathbf{e}_k}{c} \frac{\partial}{\partial t} \right) \phi = 0. \quad (3.2)$$

A plane wave propagating in the direction  $\mathbf{e}_k$  with velocity  $c$  has the form  $\phi = \phi(\mathbf{x} \cdot \mathbf{e}_k - ct)$ . Applying the first factor in Eq. (3.2) to the plane wave  $\phi = \phi(\mathbf{x} \cdot \mathbf{e}_k - ct)$  results in:

$$\left( \nabla + \frac{\mathbf{e}_k}{c} \frac{\partial}{\partial t} \right) \phi = 0. \quad (3.3)$$

This means that the factor  $\nabla + (\mathbf{e}_k/c)(\partial/\partial t)$  is able to identify plane waves traveling in the direction  $\mathbf{e}_k$ . Similarly, the second factor in Eq. (3.2) corresponds to those waves propagating in the opposite direction  $-\mathbf{e}_k$ . If outgoing waves are propagating in the direction  $\mathbf{e}_k$ , the operator  $\nabla + (\mathbf{e}_k/c)(\partial/\partial t)$  can be used to design a boundary condition which absorbs these waves without reflection under potential flow assumptions.

In this type of boundary condition, the wave propagation direction  $\mathbf{e}_k$  is used as a criterion to absorb plane waves. In this thesis,  $\mathbf{e}_k$  is a fixed parameter for the entire domain boundary. The generating function is added to the right-hand side of the boundary condition, which considers the incoming wave. It is called the generating and absorbing boundary condition in this work. For multi-directional waves, the second-order boundary condition is adopted by concatenating two of these absorption operators.

### 3.3 Outflow boundary condition

The derivation of the outflow boundary condition for waves with current on the basis of linear potential wave theory will be given in this section. The wave equation with uniform current is derived first, followed by different paths to reach the final choice of the boundary condition.

#### 3.3.1 Wave equation with uniform current

A constant current  $\mathbf{U}$ , independent of position and time and propagating in the horizontal plane, is considered in potential flow. First split off the current component from the potential  $\phi$ , i.e.

$$\phi = \mathbf{U} \cdot \mathbf{x} + \phi_w, \quad (3.4)$$

where  $\phi_w$  is the velocity potential due to waves and the term  $\mathbf{U} \cdot \mathbf{x}$  represents the potential due to the current.

### Boundary conditions

At the free surface  $z = \eta(x, y, t)$ , the kinematic condition reads:

$$w = \frac{d\eta}{dt} = \frac{\partial\eta}{\partial t} + \frac{\partial\eta}{\partial x} \frac{dx}{dt} + \frac{\partial\eta}{\partial y} \frac{dy}{dt}, \quad (3.5)$$

indicating that the velocity of the surface elevation equals the vertical component of the velocity for the fluid particle at the same location. Here the variable  $\eta$  describes the position of the free surface, with the origin of the coordinate system positioned at the equilibrium of the free surface and the vertical axis in  $z$ -direction pointing upwards.

For the velocity potential  $\phi$ , its spatial derivatives result in velocities in respective directions:

$$\frac{dx}{dt} = u = (u_w + U) = \frac{\partial\phi}{\partial x}, \quad \frac{dy}{dt} = v = \frac{\partial\phi}{\partial y}, \quad w = \frac{\partial\phi}{\partial z}. \quad (3.6)$$

Here  $u_w$  is the velocity of the fluid particle only due to waves.

Substitution of the above relations into the kinematic condition (3.5) and rearrangement of it yields:

$$\frac{\partial\eta}{\partial t} + \frac{\partial\phi}{\partial x} \frac{\partial\eta}{\partial x} + \frac{\partial\phi}{\partial y} \frac{\partial\eta}{\partial y} - \frac{\partial\phi}{\partial z} = 0 \Big|_{z=\eta}. \quad (3.7)$$

The dynamic boundary condition at the free surface obtained from the Bernoulli equation was given in (2.11). It is rewritten here as:

$$g\eta + \frac{\partial\phi}{\partial t} + \frac{1}{2} |\nabla\phi|^2 = C \Big|_{z=\eta}, \quad (3.8)$$

in which  $C$  is a constant.

Additionally, the boundary condition at the horizontal bottom follows the condition of impermeability:

$$w = \frac{\partial\phi}{\partial z} = 0 \Big|_{z=-h}. \quad (3.9)$$

### Solution of the wave potential

Here a linear long-crested wave is taken into account, therefore, the wave propagating in the  $\mathbf{k}$ -direction follows the form as:

$$\phi_w = f(z) \cos(\mathbf{k} \cdot \mathbf{x} - \omega t). \quad (3.10)$$

Substituting the above relation into the Laplace equation as shown in Eq. (2.10) results in:

$$\frac{d^2 f}{dz^2} \cos(\mathbf{k} \cdot \mathbf{x} - \omega t) - |\mathbf{k}|^2 f \cos(\mathbf{k} \cdot \mathbf{x} - \omega t) = 0 \quad \Leftrightarrow \quad \frac{d^2 f}{dz^2} - |\mathbf{k}|^2 f = 0. \quad (3.11)$$

Applying the method of separation of variables in Eq. (3.11), the velocity potential of wave (only)  $\phi_w$  can be obtained as:

$$\begin{aligned} \phi_w &= \frac{1}{2} \frac{Ag}{\omega \cosh(|\mathbf{k}|h)} [e^{|\mathbf{k}|(z+h)} + e^{-|\mathbf{k}|(z+h)}] \cos(\mathbf{k} \cdot \mathbf{x} - \omega t) \\ &= \frac{Ag}{\omega \cosh(|\mathbf{k}|h)} \cosh |\mathbf{k}|(z+h) \cos(\mathbf{k} \cdot \mathbf{x} - \omega t), \end{aligned} \quad (3.12)$$

in which  $A$  is the wave amplitude.

### Dispersion relation for linear waves and uniform currents

Substitution of the velocity potential due to both waves and currents as in (3.4) into the kinematic and dynamic boundary conditions at the free surface as in (3.7) and (3.8) results in:

$$\begin{aligned} \frac{\partial \eta_w}{\partial t} + \left( U_x + \frac{\partial \phi_w}{\partial x} \right) \frac{\partial \eta_w}{\partial x} + \left( U_y + \frac{\partial \phi_w}{\partial y} \right) \frac{\partial \eta_w}{\partial y} - \frac{\partial \phi_w}{\partial z} &= 0 \Big|_{z=\eta}, \\ g\eta_w + \frac{\partial \phi_w}{\partial t} + \frac{1}{2} |\nabla \phi_w + \mathbf{U}|^2 &= C \Big|_{z=\eta}. \end{aligned} \quad (3.13)$$

By choosing the constant  $C = \frac{1}{2}U^2$  and ignoring the second-order terms, we obtain the following relations:

$$\frac{\partial \eta_w}{\partial t} + \mathbf{U} \cdot \nabla \eta_w = \frac{\partial \phi_w}{\partial z} \Big|_{z=\eta}, \quad (3.14)$$

$$\frac{\partial \phi_w}{\partial t} + \mathbf{U} \cdot \nabla \phi_w + g\eta_w = 0 \Big|_{z=\eta}. \quad (3.15)$$

Using the latter condition (3.15), which is a linearized Bernoulli equation, to eliminate the surface displacement  $\eta_w$  from the kinematic condition (3.14) gives the following formula (after multiplication with  $g$ ):

$$\left( \frac{\partial}{\partial t} + \mathbf{U} \cdot \nabla \right)^2 \phi_w = -g \frac{\partial \phi_w}{\partial z} \Big|_{z=\eta}. \quad (3.16)$$

Next focus on the right-hand side of this equation. Specific waves of the form  $\phi =$

$e^{i(\mathbf{k}\cdot\mathbf{x}-\omega t)} \cosh(|\mathbf{k}|z)$  are considered. For small amplitude waves, the relations at the exact position  $z = \eta$  are approximately satisfied at the mean free surface  $z = 0$ :

$$g \frac{\partial \phi_w}{\partial z} \Big|_{z=0} = -c_{k0}^2 \nabla \cdot \nabla \phi_w \Big|_{z=0}, \quad c_{k0}^2 \equiv g (\tanh |\mathbf{k}|h)/|\mathbf{k}|. \quad (3.17)$$

The notation  $c_{k0}$  is the propagation speed without current (hence the 0). In the presence of a current, the difference between the propagating wave and the reflected wave is no longer a minus-sign in  $c$ , as we will see next.

Substitution of the above relation into Eq. (3.16) gives the equation for both waves and currents at the free surface:

$$\left( \frac{\partial}{\partial t} + \mathbf{U} \cdot \nabla \right)^2 \phi_w = c_{k0}^2 \nabla \cdot \nabla \phi_w. \quad (3.18)$$

Finally, substituting waves of the form  $\phi_w(\mathbf{k}\cdot\mathbf{x}-\omega t)$  into (3.18) leads to the dispersion relation:

$$\omega_{\pm} - \mathbf{U} \cdot \mathbf{k} = \pm c_{k0} |\mathbf{k}|. \quad (3.19)$$

### Solution of the dispersion relation for linear propagating waves in a following and an opposing current

In this part, we discuss the dispersion relation for linear propagating waves and thus the wave number  $\mathbf{k}$  is real. The exposition is based on the work of Peregrine (1976) and Peregrine and Jonsson (1983).

For a given intrinsic wave frequency  $\sigma(k)(= c_{k0}|\mathbf{k}|)$  and water depth  $h$ , the solutions of the dispersion relation Eq. (3.19) vary with the angle between waves and currents. Here the parallel cases, i.e., waves propagate with a following or an opposing current, are of most interest. Therefore, the solutions are displayed graphically in Fig. 3.1, by plotting the left-hand side  $\omega - \mathbf{U} \cdot \mathbf{k}$  and the right-hand side  $\pm c_{k0}|\mathbf{k}|$ , which is  $\pm\sigma(k)$  in the figure, of the dispersion Eq. (3.19). In Fig. 3.1, the positive direction of the horizontal axis is chosen as the direction of wave propagation and then a following current ( $\mathbf{U} \cdot \mathbf{k} > 0$ ) is positive while an opposing current is negative ( $\mathbf{U} \cdot \mathbf{k} < 0$ ).

The dashed line parallel to the  $k$ -axis in the figure represents the solution for the wave-only (no current) case. Only one solution, marked by point  $E$ , is found. For the case with a parallel current, two lines of  $\omega - \mathbf{U} \cdot \mathbf{k}$ , corresponding to a following and an opposing current, are plotted in the figure. Four possible solutions are marked by points  $A$ ,  $B$ ,  $C$  and  $D$ , in which points  $C$  and  $D$  describe the case of waves in a following current, while points  $A$  and  $B$  correspond to waves in an opposing current.

In maritime engineering, solutions  $A$  and  $C$  are the ones of most interest. As can be seen from the figure, a following current increases wave length and an opposing current decreases the wave length, under the condition that wave frequency and water

depth, i.e.  $c_{k0}$ , are the same.

Solutions  $B$  and  $D$ , which do not exist if there is no current, correspond to shorter waves than  $A$  and  $C$ . Solution  $B$  corresponds to waves propagating against the current, but their energy is transported in the direction of the current. Solution  $D$  corresponds to waves propagating in the direction of current and the wave energy is swept downstream by the current.

For a sufficiently large current, the solutions  $A$  and  $B$  may coincide and this has been described in Peregrine (1976):

$$c_g + \mathbf{U} \cdot \mathbf{e}_k = 0, \quad (3.20)$$

where  $c_g = \frac{d\omega}{dk}$  is the group velocity of the wave, which describes the propagation velocity of the wave energy. Let  $\theta$  be the angle between waves and currents, i.e. between  $\mathbf{e}_k$  and  $\mathbf{U}$ . In the case of waves in an opposing current,  $\theta = 180^\circ$ . In this situation the wave energy cannot be transported and the phenomenon of wave blocking is observed. If  $c_g + \mathbf{U} \cdot \mathbf{e}_k < 0$ , the solutions  $A$  and  $B$  do not exist which represents that the waves are blocked by the opposing current.

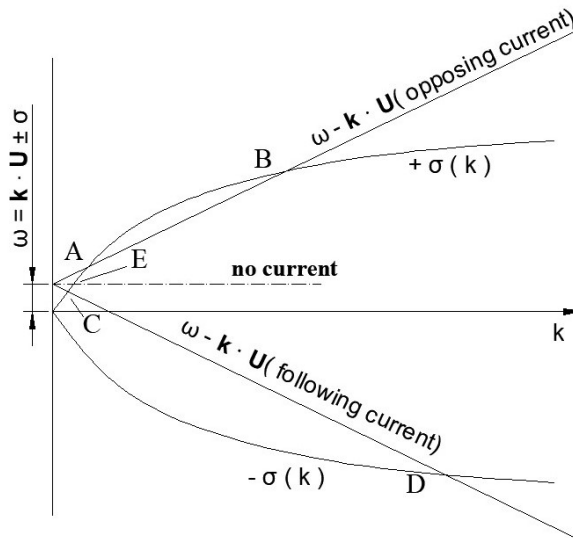


Figure 3.1: Solution of the dispersion relation for linear waves on top of uniform current. The figure is from the work of Peregrine and Jonsson (1983)

### 3.3.2 Derivation of the ABC

To derive a Sommerfeld-like boundary condition, it is observed that waves of the form  $\phi_w(\mathbf{k} \cdot \mathbf{x} - \omega t)$  satisfy:

$$\left( \mathbf{k} \frac{\partial}{\partial t} + \omega \nabla \right) \phi_w = 0. \quad (3.21)$$

Substitution of the dispersion relation (3.19) into the above relation (3.21) leads to a boundary condition of the form as below:

$$\left( \mathbf{k} \frac{\partial}{\partial t} + (\mathbf{U} \cdot \mathbf{k} \pm \omega_0) \nabla \right) \phi_w = 0 \quad \iff \quad \left( \mathbf{e}_k \frac{\partial}{\partial t} + (U_k \pm c_{k0}) \nabla \right) \phi_w = 0. \quad (3.22)$$

Note that this condition concerns a vector, hence it has three components. By dot-multiplying it with a normal vector  $\mathbf{n}$ , it results in the following condition, which is the basis for the later derivations.

$$\left( (\mathbf{n} \cdot \mathbf{e}_k) \frac{\partial}{\partial t} + (U_k \pm c_{k0}) \frac{\partial}{\partial n} \right) \phi_w = 0. \quad (3.23)$$

In Section 3.5 we will study the stability and well-posedness of this boundary condition.

**Alternative** Another option would be to multiply Eq. (3.22) by  $\mathbf{e}_k$ , after which it becomes:

$$\left( \frac{\partial}{\partial t} + (U_k \pm c_{k0}) \mathbf{e}_k \cdot \nabla \right) \phi_w = 0. \quad (3.24)$$

The essential difference with (3.23) is that it includes a tangential derivative along the boundary. Without current, Romate (1992) has studied both formulations. In his paper, they correspond with BC2 and BC1, respectively. He argues that (3.23) is well-posed (except for waves parallel to the boundary), whereas the alternative (3.24) is weakly ill-posed for all wave directions. Therefore, we will stick to (3.23).

## 3.4 ABC with uniform current

In this section, the extension of the absorbing boundary conditions for waves to include the effect of uniform current is discussed, which is the main topic of this research.

### 3.4.1 Pade approximation of the dispersion relation

The first-order boundary condition (3.23) is perfectly absorbing for a single component, but in reality waves are often composed of the superposition of a number of components. Each individual component has its own frequency, amplitude, wave number and phase. We first want to estimate the wave number of the wave that is passing the boundary at that location and at that time instant. Then the celerity belonging to this wave number needs to be used in the ABC. In particular, it is better to do this in an implicit way because of stability arguments. As the wave number

features as an argument in the dispersion relation, this requires some form of linearisation, e.g. Newton-like, which does not look attractive.

As an alternative, the better we approximate the dispersion relation, the less reflection we obtain. Now we introduce a rational polynomial in  $kh$ , discussed by Wellens (2012), where  $k = |\mathbf{k}| = \sqrt{k_x^2 + k_y^2}$ , to approximate the dispersion relation:

$$c_{k0} = \sqrt{gh} \sqrt{\frac{\tanh(kh)}{kh}} \approx \sqrt{gh} \frac{a_0 + a_1(kh)^2}{1 + b_1(kh)^2}. \quad (3.25)$$

The coefficients  $a_0$ ,  $a_1$  and  $b_1$  can be chosen such that different  $kh$ -ranges of the dispersion relation are approximated well.

### 3.4.2 Relating the wave number and the potential

Now a further improvement is introduced into the design of the boundary condition. The wave number  $k$  can be found by taking derivatives of the solution in space. In linear theory, the solution to the system of equation is given by the wave potential.

Propagating wave components satisfy the following relation for the potential:

$$\phi_w = \frac{Ag}{\omega} \frac{\cosh k(z+h)}{\cosh kh} e^{i(\mathbf{k} \cdot \mathbf{x} - \omega t)}. \quad (3.26)$$

By taking the second-order derivative in  $z$ -direction, we obtain an expression, which is  $k^2$  times the potential:

$$\frac{\partial^2 \phi_w}{\partial z^2} = k^2 \phi_w. \quad (3.27)$$

**ABC-1 with current** Substitution of the approximate dispersion relation (3.25) into the first-order Sommerfeld-like condition (3.23) leads to the following equation:

$$\begin{aligned} & \left[ (\mathbf{n} \cdot \mathbf{e}_k) \frac{\partial}{\partial t} + \left( U_k + \sqrt{gh} \frac{a_0 + a_1(kh)^2}{1 + b_1(kh)^2} \right) \frac{\partial}{\partial n} \right] \phi_w \\ &= (\mathbf{n} \cdot \mathbf{e}_k) (1 + b_1 h^2 k^2) \frac{\partial \phi_w}{\partial t} + \left( (1 + b_1 h^2 k^2) U_k + \sqrt{gh} (a_0 + a_1 h^2 k^2) \right) \frac{\partial \phi_w}{\partial n} \\ &= (\mathbf{n} \cdot \mathbf{e}_k) \left( \frac{\partial \phi_w}{\partial t} + b_1 h^2 \frac{\partial(k^2 \phi_w)}{\partial t} \right) + \left( \frac{\partial \phi_w}{\partial n} + b_1 h^2 \frac{\partial(k^2 \phi_w)}{\partial n} \right) U_k \\ & \quad + \sqrt{gh} \left( a_0 \frac{\partial \phi_w}{\partial n} + a_1 h^2 \frac{\partial(k^2 \phi_w)}{\partial n} \right) = 0. \end{aligned} \quad (3.28)$$

Substitution of the relation (3.27) into the equation (3.28) yields the first-order condition ABC-1:

$$\begin{aligned}
& (\mathbf{n} \cdot \mathbf{e}_k) \left( \frac{\partial \phi_w}{\partial t} + b_1 h^2 \frac{\partial(\partial^2 \phi_w / \partial z^2)}{\partial t} \right) + \left( \frac{\partial \phi_w}{\partial n} + b_1 h^2 \frac{\partial(\partial^2 \phi_w / \partial z^2)}{\partial n} \right) U_k \\
& + \left( \sqrt{gh} a_0 \frac{\partial \phi_w}{\partial n} + a_1 h^2 \frac{\partial(\partial^2 \phi_w / \partial z^2)}{\partial n} \right) \\
& = (\mathbf{n} \cdot \mathbf{e}_k) \left( \frac{\partial \phi_w}{\partial t} + b_1 h^2 \partial^2 / \partial z^2 \frac{\partial \phi_w}{\partial t} \right) + \left( \frac{\partial \phi_w}{\partial n} + b_1 h^2 \partial^2 / \partial z^2 \frac{\partial \phi_w}{\partial n} \right) U_k \\
& + \left( \sqrt{gh} a_0 \frac{\partial \phi_w}{\partial n} + a_1 h^2 \partial^2 / \partial z^2 \frac{\partial \phi_w}{\partial n} \right) \\
& = \left[ (\mathbf{n} \cdot \mathbf{e}_k) \left( 1 + b_1 h^2 \frac{\partial^2}{\partial z^2} \right) \frac{\partial}{\partial t} + \right. \\
& \quad \left. \left( \left( 1 + b_1 h^2 \frac{\partial^2}{\partial z^2} \right) U_k + \sqrt{gh} \left( a_0 + a_1 h^2 \frac{\partial^2}{\partial z^2} \right) \right) \frac{\partial}{\partial n} \right] \phi_w = 0. \tag{3.29}
\end{aligned}$$

**GABC-1 with current** At the inflow boundary, incoming waves need to be specified while preventing re-reflection of outgoing waves simultaneously. A non-zero right-hand side consisting of the same combination of operators applied to the incoming wave potential is prescribed following Perkins et al. (1997), which leads to the first-order generating and absorbing boundary condition (GABC-1) with current as follows:

$$\begin{aligned}
& \left[ (\mathbf{n} \cdot \mathbf{e}_k) \frac{\partial}{\partial t} + \left( U_k + \sqrt{gh} \frac{a_0 + a_1 h^2 \partial^2 / \partial z^2}{1 + b_1 h^2 \partial^2 / \partial z^2} \right) \frac{\partial}{\partial n} \right] \phi_w \\
& = \left[ (\mathbf{n} \cdot \mathbf{e}_k) \frac{\partial}{\partial t} + \left( U_k + \sqrt{gh} \frac{a_0 + a_1 h^2 \partial^2 / \partial z^2}{1 + b_1 h^2 \partial^2 / \partial z^2} \right) \frac{\partial}{\partial n} \right] \phi_{in}. \tag{3.30}
\end{aligned}$$

Here  $\phi_{in}$  denotes the incoming wave potential. Now a truly open boundary condition GABC-1 with current for long-crested dispersive waves and uniform current is obtained.

**ABC-2 with current** Before going to the second-order absorbing boundary condition (ABC-2), the Sommerfeld-like boundary condition should be given. It follows the idea of Higdon (1986). Two wave directions and celerities are chosen to absorb two wave components, which results in the second-order boundary condition:

$$\prod_{i=1}^2 \left( (\mathbf{n} \cdot \mathbf{e}_{ki}) \frac{\partial}{\partial t} + (U_k + c_{ki}) \frac{\partial}{\partial n} \right) \phi_w = 0. \tag{3.31}$$

The condition (3.31) is satisfied exactly by any plane wave  $\phi_w$  travelling out of the domain at the directions  $\mathbf{e}_{k1}$  and  $\mathbf{e}_{k2}$  with the phase speeds  $c_{k1}$  and  $c_{k2}$ , respectively. The expansion of the condition (3.32) results in:

$$\left( (\mathbf{n} \cdot \mathbf{e}_{k1}) \frac{\partial}{\partial t} + (U_k + c_{k1}) \frac{\partial}{\partial n} \right) \left( (\mathbf{n} \cdot \mathbf{e}_{k2}) \frac{\partial}{\partial t} + (U_k + c_{k2}) \frac{\partial}{\partial n} \right) \phi_w = 0. \quad (3.32)$$

To obtain the dispersive boundary condition in second order, only one of the operators in the condition (3.32) can include the approximation (3.25) for the dispersion relation. Otherwise, the product of two approximations would yield a fourth-order derivative in  $z$ -direction, which yields difficulties in the discretization at the boundaries. Consequently, substitution of the relation (3.25) and (3.27) in one of the operators in the condition (3.32) gives the ABC-2 as follows:

$$\left[ (\mathbf{n} \cdot \mathbf{e}_{k1}) \frac{\partial}{\partial t} + (U_k + c_{k1}) \frac{\partial}{\partial n} \right] \cdot \left[ (\mathbf{n} \cdot \mathbf{e}_{k2}) \frac{\partial \phi_w}{\partial t} + \left( U_k + \sqrt{gh} \frac{a_0 + a_1 h^2 \partial^2 / \partial z^2}{1 + b_1 h^2 \partial^2 / \partial z^2} \right) \frac{\partial \phi_w}{\partial n} \right] = 0. \quad (3.33)$$

Unlike the boundary condition GABC-1 in (3.30), we can not simply prescribe an incoming wave potential to the right-hand side of the condition ABC-2 in (3.33), due to the existence of second derivatives of the wave potential. The second derivatives of the wave potential are the derivatives of the velocity and pressure, which are not known at the inflow boundary. Since there are not proper approaches yet to add the generating functionality to the condition ABC-2, we will not discuss the condition GABC-2.

### 3.4.3 Boundary conditions in terms of primitive variables

The GABC-1 and ABC-2 with current in the boundary condition (3.30) and (3.33) are utilized as boundary conditions for outgoing waves and currents in ComFLOW that solves for velocities and pressures. The solution variables are staggered within a cell. The domain boundary is chosen such that it coincides with the position of the horizontal velocity  $u_b$ . It is essential that the velocity and pressure in this boundary condition are defined at the same position. Any other configuration would lead to phase differences between solution variables at the boundary and additional spurious reflection.

In potential theory, the velocity in  $n$ -direction is defined to be the derivative of the potential in that direction:

$$\frac{\partial \phi_w}{\partial n} = \mathbf{u}_w \cdot \mathbf{n} = (\mathbf{u}_b - \mathbf{U}) \cdot \mathbf{n}. \quad (3.34)$$

The subscript  $w$  describes the velocity only due to waves. The subscript  $b$  here indicates the total velocity, defined exactly on the domain boundary, attributed to both waves and current.

To obtain the expression for the pressure, the linearized Bernoulli equation is used:

$$\frac{\partial \phi_w}{\partial t} = -\frac{p_b}{\rho} - gz - \mathbf{u}_w \cdot \mathbf{U}. \quad (3.35)$$

Again the subscript  $b$  implies that the pressure is specified at the domain boundary.

**S-1 with current** Substituting (3.34) and (3.35) into (3.23) produces:

$$(\mathbf{n} \cdot \mathbf{e}_k) \left( -gz - \frac{p_b}{\rho} - \mathbf{u}_w \cdot \mathbf{U} \right) + (U_k + c_{k0})(\mathbf{u}_w \cdot \mathbf{n}) = 0. \quad (3.36)$$

Since the following relation holds:

$$\begin{aligned} U_k \mathbf{u}_w \cdot \mathbf{n} &= (\mathbf{U} \cdot \mathbf{e}_k)(\mathbf{n} \cdot \nabla) \phi_w = (\mathbf{U} \cdot \mathbf{e}_k)(\mathbf{n} \cdot \mathbf{k}) \phi'_w \\ &= (\mathbf{n} \cdot \mathbf{e}_k)(\mathbf{U} \cdot \mathbf{k}) \phi'_w = (\mathbf{n} \cdot \mathbf{e}_k)(\mathbf{U} \cdot \nabla) \phi_w \\ &= (\mathbf{n} \cdot \mathbf{e}_k)(\mathbf{u}_w \cdot \mathbf{U}). \end{aligned} \quad (3.37)$$

The S-1 with current becomes:

$$(\mathbf{n} \cdot \mathbf{e}_k) \left( -gz - \frac{p_b}{\rho} \right) + c_{k0}[(\mathbf{u}_w - \mathbf{U}) \cdot \mathbf{n}] = 0. \quad (3.38)$$

**GABC-1 with current** In the same way as above, substitution of the relations (3.34) and (3.35) into (??) yields:

$$\begin{aligned} &(\mathbf{n} \cdot \mathbf{e}_k) \left( 1 + b_1 h^2 \frac{\partial^2}{\partial z^2} \right) \left( -gz - \frac{p_b}{\rho} - \mathbf{u}_w \cdot \mathbf{U} \right) \\ &+ \left[ U_k \left( 1 + b_1 h^2 \frac{\partial^2}{\partial z^2} \right) + \sqrt{gh} \left( a_0 + a_1 h^2 \frac{\partial^2}{\partial z^2} \right) \right] (\mathbf{u}_w \cdot \mathbf{n}) = 0. \end{aligned} \quad (3.39)$$

Using the relation (3.37), the GABC-1 with current (3.39) can be written as follows:

$$\begin{aligned} &(\mathbf{n} \cdot \mathbf{e}_k) \left( 1 + b_1 h^2 \frac{\partial^2}{\partial z^2} \right) \left( -gz - \frac{p_b}{\rho} \right) \\ &+ \sqrt{gh} \left( a_0 + a_1 h^2 \frac{\partial^2}{\partial z^2} \right) [(\mathbf{u}_b - \mathbf{U}) \cdot \mathbf{n}] = 0. \end{aligned} \quad (3.40)$$

**ABC-2 with current** In the same manner, the ABC-2 with current can be expressed in terms of the velocity and pressure as follows:

$$\begin{aligned} & \left[ (\mathbf{n} \cdot \mathbf{e}_{k1}) \frac{\partial}{\partial t} + (U_k + c_{k1}) \frac{\partial}{\partial n} \right] \cdot \\ & \left[ (\mathbf{n} \cdot \mathbf{e}_{k2}) \left( 1 + b_1 h^2 \frac{\partial^2}{\partial z^2} \right) \left( -gz - \frac{p_b}{\rho} \right) + \sqrt{gh} \left( a_0 + a_1 h^2 \frac{\partial^2}{\partial z^2} \right) [(\mathbf{u}_b - \mathbf{U}) \cdot \mathbf{n}] \right] = 0. \end{aligned} \quad (3.41)$$

### 3.5 Stability

It is imperative to analyze the stability of the above absorbing boundary condition for combined wave-current flow before implementing it in the program. The stability of the first-order ABC only for waves has been investigated by means of the reflection coefficients in Wellens (2012), followed by Duz (2015) who shows that the criteria stated in Wellens (2012) can safely be used in the second-order ABC. In this work, a uniform current is added into the ABC, thus the stability of this boundary condition is required to be analyzed as well.

Following again the footsteps of the work in Wellens (2012), we study the stability of the boundary condition including the effect of current via reflection coefficients. The reflection coefficient  $|R| = A_{refl}/A_{out}$ , in which  $A_{refl}$  and  $A_{out}$  represent the wave amplitude of the outgoing and reflected waves, respectively. It is required that the reflection coefficient  $|R| \leq 1$ .

The analytical reflection coefficients for progressive, evanescent and spurious waves are derived in Appendix A. Here we only show the results as follows:

$$R = - \left( \frac{k_{out}}{\omega} - \frac{1}{c_{bc} + U} \right) / \left( \frac{k_{refl}}{\omega} - \frac{1}{c_{bc} + U} \right) \quad (3.42)$$

in which  $c_{bc}$  is the approximate celerity in the boundary condition.  $k_{out}$  and  $k_{refl}$  are the wave numbers of the outgoing and reflected wave components respectively, with  $k_{out} \geq 0$  and  $k_{refl} \leq 0$ . They can be computed from the dispersion relation in Appendix A. It holds that  $k_{refl} \neq -k_{out}$  due to the Doppler effect of the current on the dispersion relation. Recall that for right-going progressive and spurious waves  $k_{out}/\omega$  is real and positive.

The stability of the boundary condition is satisfied by adjusting the parameters  $a_0$ ,  $a_1$  and  $b_1$  in the approximate dispersion relation. This can be analyzed by observing the different solution modes to the wave equation: propagating, evanescent and spurious wave modes.

### 3.5.1 Dispersion relation of progressive, evanescent and spurious waves

The intrinsic wave frequency  $\sigma$  satisfies a dispersion relation which links it to the wave number  $\omega = \sigma(k) + kU_k$ :

$$(\omega - kU_k)^2 = \sigma^2 \equiv gh \tanh(kh); \quad c = c_0 + U_k \text{ with } c_0 \equiv \sigma/k. \quad (3.43)$$

In case the magnitude of the wave number is imaginary, i.e.  $k = ik_I$  with  $k_I$  real, the dispersion relation (3.43) can be rewritten as (note  $\tanh(i\theta) = i \tan \theta$ ):

$$\omega = \sigma + kU_k \text{ with } \sigma^2 = -gk_I \tan(k_I h); \quad c = c_0 + U_k \text{ with } c_0^2 = -\frac{\sigma^2}{k_I^2}. \quad (3.44)$$

**Progressive waves** For progressive surface waves  $k$  is real. The dispersion relation (3.43) shows that  $\omega = \sigma + kU_k$  is also real, as well as the phase velocity  $c = c_0 + U_k = \sigma/k + U_k$ . Their signs depend on the magnitude of the current component  $U_k$ .

**Spurious waves** For spurious waves the imaginary wave number satisfies  $0 + n\pi < |k_I|h < \pi/2 + n\pi$  ( $n = 0, 1, \dots$ ). In this case,  $k_I \tan(k_I h)$  is positive, hence the dispersion relation (3.44) shows that  $\sigma^2 < 0$  and the intrinsic frequency becomes imaginary: say  $\sigma = i\sigma_I$  with  $\sigma_I$  real. The absolute frequency  $\omega = \sigma + kU_k$  is purely imaginary and the phase velocity  $c = \omega/k$  is real.

**Evanescent waves** For evanescent waves,  $k$  is purely imaginary,  $k = ik_I$ , with  $\pi/2 + n\pi \leq |k_I|h < \pi + n\pi$  ( $n = 0, 1, \dots$ ). In this case  $k_I \tan(k_I h)$  is negative, hence the intrinsic frequency  $\sigma$  is real as  $\sigma^2 > 0$ , whereas  $c_0$  is purely imaginary. However, the absolute frequency  $\omega = \sigma + kU_k = \sigma + ik_I U_k$  is complex, and so is the phase velocity  $c = c_0 + U_k$ .

Table 3.1 gives an overview whether the frequency and phase velocity are real or complex, depending on the wave number.

wave	wave number $k$	frequency $\omega$		phase velocity $c$	
		intrinsic $\sigma$	$\sigma + kU_k$	intrinsic $c_0$	$c_0 + U_k$
progressive	real	real	real	real	real
spurious	imaginary	imaginary	imaginary	real	real
evanescent	imaginary	real	complex	imaginary	complex

Table 3.1: Signature of the wave properties for the various types of waves.

### 3.5.2 Padé approximation of the dispersion relation

The GABC makes use of a Padé approximation for the dispersion relation. The approximate phase speed is defined as:

$$c_a = \sqrt{gh} \frac{a_0 + a_1(kh)^2}{1 + b_1(kh)^2}. \quad (3.45)$$

In case  $k^2 \geq 0$  the wave number is real, i.e. we deal with progressive waves. As all coefficients in (3.45) are non-negative, the approximate phase velocity  $c_a$  is positive.

However, when  $k^2 < 0$ , i.e. we are dealing with evanescent and spurious waves, the situation differs. For convenience let  $k = ik_I$  with  $k_I$  real-valued. Then the wave speed can be written as:

$$c_a = \sqrt{gh} \frac{a_0 - a_1(k_I h)^2}{1 - b_1(k_I h)^2}. \quad (3.46)$$

Both numerator and denominator can (and will) switch sign, and they will not do so at the same  $k_I$ . Hence  $c_a$  will be negative for a certain interval of  $k_I$  values. We will choose  $c_{bc} = c_a$  for the later analysis.

**Without current** When the current is absent, i.e.  $U = 0$ , the expressions for the reflected wave simplify to:

$$k_{refl} = -k_{out} \quad \text{and} \quad c_{refl} = -c_{out}. \quad (3.47)$$

In this situation, the reflection coefficient turns into :

$$R = \frac{k_{out}/\omega - 1/c_{bc}}{k_{out}/\omega + 1/c_{bc}}. \quad (3.48)$$

For progressive outgoing waves both  $k_{out}/\omega$  and  $c_{bc}$  are real and positive, and  $|R| \leq 1$  follows immediately. According to Table 3.1, also for outgoing spurious waves the quotient  $k_{out}/\omega$  is real and positive. We only have to prevent that  $c_{bc}$  becomes negative, as then  $|R|$  might grow beyond unity. This condition now leads to requirements for the coefficients  $a_0, a_1$  and  $b_1$ : the zeros of numerator and denominator must lie in the evanescent range. This was achieved in Wellens (2012) and Duz (2015):

$$\frac{a_0}{\pi^2} < a_1 < \frac{4a_0}{\pi^2} \quad \text{and} \quad a_1 < b_1 < \frac{4}{\pi^2}. \quad (3.49)$$

Without current, in the evanescent region the numerator and denominator of the expression for  $R$  are each others complex conjugate, independent of the sign of  $c_{bc}$ . In this case, the sign of  $c_{bc}$  can do no harm, since the wave number  $k_{out}$  is purely imaginary (see Table 3.1). Hence, without current  $|R| = 1$  is guaranteed in the evanescent region. Therefore, the parameters  $a_0, a_1$  and  $b_1$  are always chosen according to the conditions (3.49).

**With current** When there is current,  $U > 0$ , the proofs for  $|R| \leq 1$  are getting more complicated. For progressive and spurious waves it has been proven in Appendix B, see (B.9), that  $0 \leq k_{out}/\omega \leq -k_{refl}/\omega$ . With  $c_{bc} \geq 0$ , it is not difficult to see that for these wave always  $|R| \leq 1$ .

However, for evanescent waves the frequency  $\omega$  becomes complex (see Table 3.1). Also the relations (3.47) for  $k_{refl}$  and  $c_{refl}$  do not hold any more. Hence the argument of complex conjugacy for  $R$  is no longer valid. An analytical analysis is quite cumbersome, but a numerical analysis is feasible. With the values for  $k_{refl}$  from Appendix B, the reflection coefficient can be computed from (3.42). It turns out (not shown here) that for  $c_{bc} + U < 0$  the reflection coefficient can become larger than unity. This means that boundary condition GABC does allow reflection coefficients above unity for evanescent waves in the range where  $c_{bc} + U$  is negative. In practice, this has never led to numerical instabilities.

**Remark** Another way to study stability/well-posedness is by means of a normal-mode analysis as promoted by Kreiss (1970) and Higdon (1986). This approach is closely related to, but somewhat weaker than, the above study of the reflection coefficient. It only requires  $|R|$  to be finite, possibly larger than unity (see Sections 3 and 7 of Higdon (1986)). Romate (1992) has carried out a normal-mode analysis for the boundary condition GABC in a situation without current. His analysis can be generalized to include a current in positive  $x$ -direction. The result is that the condition GABC is well-posed, i.e. stable, for all waves that are not parallel to the boundary.

Note that the reflection coefficient of the first-order Sommerfeld condition in a 2D domain is derived in Appendix B. An assumption that  $k_y^{refl} = k_y^{out}$  has been made, in which  $k_y^{refl}$  and  $k_y^{out}$  are the wave numbers of the reflected and outgoing wave modes in  $y$ -direction, respectively. It is open for discussion whether that assumption is correct or not.

### 3.6 Discretization of the boundary conditions

This section presents the discretization of the boundary conditions ABC-1 in Eq. (3.40) and ABC-2 in Eq. (3.41) with current in ComFLOW. We choose  $\mathbf{n} = \mathbf{e}_x$  in these two equations and present the boundary conditions in this situation. The discretization of the boundary conditions S-1 and S-2 with current will not be given here, since they can simply be obtained from the discretization of the ABC-1 and ABC-2 by ignoring the Pade approximation of the dispersion relation.

An ABC contains a combination of pressure and velocity and we want to apply it at the in/outflow boundary of the domain. At the boundary, the velocity is defined, but the pressure is defined half a mesh size away.

**Discretisation of ABC-1** Adding the spatial and temporal level to the variables  $p_b$  and  $\mathbf{u}_b$  in the boundary condition (3.40):

$$\begin{aligned}
& (\mathbf{e}_x \cdot \mathbf{e}_k) \left( 1 + b_1 h^2 \frac{\partial^2}{\partial z^2} \right) \left( -gz - \frac{p_{b,k}^{n+1}}{\rho} \right) \\
& + \sqrt{gh} \left( a_0 + a_1 h^2 \frac{\partial^2}{\partial z^2} \right) [(\mathbf{u}_{b,k}^{n+1} - \mathbf{U}) \cdot \mathbf{e}_x] = 0.
\end{aligned} \tag{3.50}$$

The pressure at the boundary  $p_{b,k}^{n+1}$  is obtained from linear interpolation between the pressure on either side of the boundary:

$$p_{b,k}^{n+1} = \frac{1}{2}(p_{i,k} + p_{i+1,k})^{n+1}. \tag{3.51}$$

in which the locations of the pressures near the boundary  $p_{b,k}$ ,  $p_{i,k}$  and  $p_{i+1,k}$  are shown in Fig. 3.2. The superscript  $n + 1$  denotes the time level that the pressure variables are defined at.

It is essential that the velocity and the pressure at the boundary are defined at the same point in time. The pressures and velocities at the boundary are determined at time  $t^{n+1}$ .

Here we discuss the discrete ABC-1 in the  $xz$ -plane, therefore, the  $x$ -component of the term  $(\mathbf{u}_{b,k}^{n+1} - \mathbf{U}) \cdot \mathbf{n}$  is written as  $u_{b,k}^{n+1} - U_x$ .

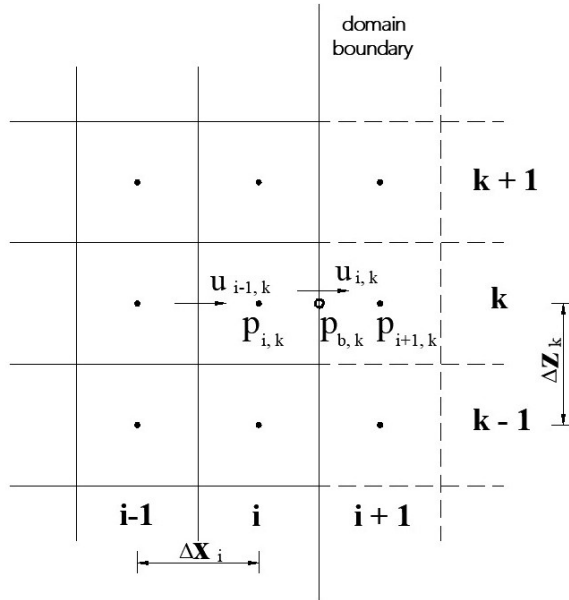


Figure 3.2: Pressure at the domain boundary is calculated from the linear interpolation of the pressure on either side of the boundary

The horizontal velocity at the new time level  $u_{b,k}^{n+1}$  can be eliminated by means of the momentum equation at the boundary:

$$u_{b,k}^{n+1} = u_{i,k}^{n+1} = \tilde{u}_{i,k} - \frac{1}{\rho} \frac{\Delta t}{\Delta x_{i+1,k}} (p_{i+1,k} - p_{i,k})^{n+1}. \quad (3.52)$$

Note that  $\tilde{u}$ , given in Eq. (2.34) in Section 2.5, contains convective and diffusive terms.

For the approximation of the second-order derivation in the  $z$ -direction, the following operator, designed for a stretched grid, which has been used in Wellens (2012) and Duz (2015), is employed:

$$\mathcal{Q} = \begin{bmatrix} \mathcal{Q}_1 \\ \mathcal{Q}_2 \\ \mathcal{Q}_3 \end{bmatrix} = \frac{1}{\frac{1}{2} \Delta z_{i,k} \Delta z_{i,k+1} (\Delta z_{i,k} + \Delta z_{i,k+1})} \begin{bmatrix} \Delta z_{i,k} \\ -\Delta z_{i,k} - \Delta z_{i,k+1} \\ \Delta z_{i,k+1} \end{bmatrix}. \quad (3.53)$$

Here  $\Delta z_{i,k} = z_{i,k} - z_{i,k-1}$  and  $\Delta z_{i,k+1} = z_{i,k+1} - z_{i,k}$ .  $z_{i,k-1}$ ,  $z_{i,k}$  and  $z_{i,k+1}$  are the center locations of the pressure variables  $p_{i,k-1}$ ,  $p_{i,k}$  and  $p_{i,k+1}$  in Fig. 3.2, respectively. The operator  $\mathcal{Q}$  is a grid vector that operates on the vectors  $\mathbf{p}$  and  $\tilde{\mathbf{u}}$  as will be used later.

Substituting the expressions (3.51) through (3.53) into the equation (3.50) yields:

$$\begin{aligned} & (\mathbf{e}_x \cdot \mathbf{e}_k) \left( 1 + b_1 h^2 \frac{\partial^2}{\partial z^2} \right) \left( -gz - \frac{1}{2} (p_{i,k} + p_{i+1,k})^{n+1} \right) \\ & + \sqrt{gh} \left( a_0 + a_1 h^2 \frac{\partial^2}{\partial z^2} \right) \left( \tilde{u}_{i,k} - \frac{1}{\rho} \frac{\Delta t}{\Delta x_{i+1,k}} (p_{i+1,k} - p_{i,k})^{n+1} - U_x \right) = 0. \end{aligned} \quad (3.54)$$

Now the following notations are introduced:

$$\begin{aligned} \varphi &= \sqrt{gh} a_0, \quad \chi = \sqrt{gh} a_1 h^2, \quad \psi = (\mathbf{e}_x \cdot \mathbf{e}_k) b_1 h^2 \quad \text{and} \quad \tau = \frac{1}{\rho} \frac{\Delta t}{\Delta x}, \\ \mathbf{p}_i &= \begin{bmatrix} \mathbf{p}_{i,k-1} \\ \mathbf{p}_{i,k} \\ \mathbf{p}_{i,k+1} \end{bmatrix}, \quad \mathbf{u}_i = \begin{bmatrix} \tilde{u}_{i,k-1} \\ \tilde{u}_{i,k} \\ \tilde{u}_{i,k+1} \end{bmatrix}. \end{aligned} \quad (3.55)$$

By convention, we leave the terms of unknown variables on the left-hand side and known variables on the right-hand side of the equation. The second-order derivatives in  $z$ -direction of the variables  $gz$  and  $U_x$ , i.e.  $\frac{\partial^2}{\partial z^2}(gz)$  and  $\frac{\partial^2}{\partial z^2}U_x$ , are zeros. Applying the grid vector in (3.53) and the notations in (3.55) to Eq. (3.54), a discrete equation for the absorbing boundary conditions is obtained:

$$[\mathcal{B}_{zl} \ \mathcal{B}_c \ \mathcal{B}_{zr}] \mathbf{p}_i + [\mathcal{B}_{rl} \ \mathcal{B}_{rc} \ \mathcal{B}_{rr}] \mathbf{p}_{i+1} = [\mathcal{E}_{zl} \ \mathcal{E}_c \ \mathcal{E}_{zr}] \tilde{\mathbf{u}}_i + (\mathbf{n} \cdot \mathbf{e}_k) gz + \varphi U_x. \quad (3.56)$$

The matrix coefficients in  $\mathcal{C}$  and  $\mathcal{E}$  are defined to be:

$$\begin{aligned} \mathcal{B}_{zl} &= (-\chi\tau + \frac{1}{2}\psi)\mathcal{Q}_1, & \mathcal{B}_c &= -\varphi\tau + \frac{1}{2}(\mathbf{n} \cdot \mathbf{e}_k) - (\chi\tau - \frac{1}{2}\psi)\mathcal{Q}_2, & \mathcal{B}_{zr} &= (-\chi\tau + \frac{1}{2}\psi)\mathcal{Q}_3, \\ \mathcal{B}_{rl} &= (\chi\tau + \frac{1}{2}\psi)\mathcal{Q}_1, & \mathcal{B}_{rc} &= \varphi\tau + \frac{1}{2}(\mathbf{n} \cdot \mathbf{e}_k) + (\chi\tau + \frac{1}{2}\psi)\mathcal{Q}_2, & \mathcal{B}_{rr} &= (\chi\tau + \frac{1}{2}\psi)\mathcal{Q}_3, \\ \mathcal{E}_{zl} &= \chi\mathcal{Q}_1, & \mathcal{E}_c &= \varphi - \chi\mathcal{Q}_2, & \mathcal{E}_{zr} &= \chi\mathcal{Q}_3. \end{aligned} \quad (3.57)$$

Equation (3.56) is an equation for the pressure variable  $p_{i+1,k}$  in a mirror cell outside the domain. The pressure at the new time level  $t^{n+1}$  is located on the left-hand side, while on the right-hand side horizontal velocities including convective and diffusive terms at the old time level  $t^n$  are placed.

The grid stencil of the discrete ABC-1 in (3.56) is quite similar to that of the pressure Poisson equation (2.36) derived in Section 2.4 and can hence easily be combined with the field equations inside the domain. However, the matrix on the left-hand side includes the additional coefficients of the ABC-1, which is neither symmetric nor diagonally dominant, see the stencil in Fig. 3.2. This is different from the matrix in a normal Poisson solver stencil.

**Discretization of ABC-2** Analogous to the discretization for the boundary condition GABC-1, the same steps are followed to discretize the ABC-2 in Eq. (3.41).

The temporal and spatial derivatives in the  $x$ -direction of the variables  $gz$  and  $U_x$ , i.e.  $\frac{\partial}{\partial t}(gz)$ ,  $\frac{\partial}{\partial t}(U_x)$ ,  $\frac{\partial}{\partial x}(gz)$  and  $\frac{\partial}{\partial x}(U_x)$ , are zeros. Therefore, the right-hand side will be zero and the left-hand side with the unknown variables remains as follows:

$$\begin{aligned} & \left[ (\mathbf{e}_x \cdot \mathbf{e}_{k1}) \frac{\partial}{\partial t} + (U_x + c_{k1}) \frac{\partial}{\partial x} \right] \cdot \\ & \left[ -\frac{1}{\rho} (\mathbf{e}_x \cdot \mathbf{e}_{k2}) p_{b,k}^{n+1} - \frac{1}{\rho} (\mathbf{e}_x \cdot \mathbf{e}_{k2}) b_1 h^2 \frac{\partial^2 p_{b,k}^{n+1}}{\partial z^2} + \sqrt{gh} a_o u_{b,k}^{n+1} + \sqrt{gh} a_1 h^2 \frac{\partial^2 u_{b,k}^{n+1}}{\partial z^2} \right] = 0. \end{aligned} \quad (3.58)$$

It can be observed from the above equation that the derivatives of the pressure with respect to time and space are required. They are given as follows:

$$\frac{\partial p_{b,k}^{n+1}}{\partial t} = \frac{p_{b,k}^{n+1} - p_{b,k}^n}{\Delta t}, \quad \frac{\partial p_{b,k}}{\partial x} = \frac{p_{i+1,k}^{n+1} - p_{i,k}^{n+1}}{\Delta x_i}, \quad (3.59)$$

in which  $p_b$  at the time level  $n$  and  $n+1$  are obtained using the linear interpolation of the pressure values on either side of the boundary as in the relation (3.51) for ABC-1. Therefore, the term  $\partial p_{b,k}/\partial t$  can be further expressed as:

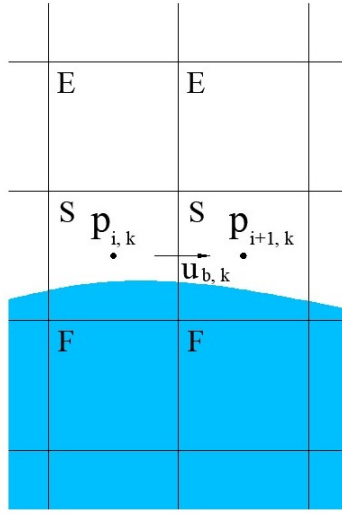


Figure 3.3: No second derivatives of the solution variables are implemented at the free surface

$$\frac{\partial p_{b,k}^{n+1}}{\partial t} = \frac{1}{2} \frac{p_{i+1,k}^{n+1} + p_{i,k}^{n+1} - p_{i+1,k}^n - p_{i,k}^n}{\Delta t}. \quad (3.60)$$

Likewise, the derivatives of the velocity component with respect to time and space are expressed as:

$$\frac{\partial u_{b,k}^{n+1}}{\partial t} = \frac{u_{i,k}^{n+1} - u_{i,k}^n}{\Delta t}, \quad \frac{\partial u_{b,k}^{n+1}}{\partial x} = \frac{u_{i,k}^{n+1} - u_{i-1,k}^{n+1}}{\Delta x_i}, \quad (3.61)$$

where  $\Delta x_i = x_i - x_{i-1}$ , see Fig. 3.2.

In order to make a compact stencil for the pressure, the following notations are introduced:

$$\begin{aligned} \gamma &= -\frac{1}{2\rho}(\mathbf{e}_x \cdot \mathbf{e}_{k1})(\mathbf{e}_x \cdot \mathbf{e}_{k2}) \frac{1}{\Delta t}, & \epsilon &= -\frac{1}{\rho}(\mathbf{e}_x \cdot \mathbf{e}_{k2})(U_x + c_1) \frac{1}{\Delta x_{i,k}}, \\ \lambda &= -(\mathbf{e}_x \cdot \mathbf{e}_{k1}) \frac{1}{\Delta x_{i+1,k}}, & \kappa &= -(U_x + c_1) \frac{1}{\Delta x_{i,k}} \frac{\Delta t}{\Delta x_{i+1,k}}, \\ \mathbf{p}_{i,k}^{n+1} &= \begin{bmatrix} \mathbf{p}_{i,k-1}^{n+1} \\ \mathbf{p}_{i,k}^{n+1} \\ \mathbf{p}_{i,k+1}^{n+1} \end{bmatrix}, & \mathbf{p}_{i,k}^n &= \begin{bmatrix} \mathbf{p}_{i,k-1}^n \\ \mathbf{p}_{i,k}^n \\ \mathbf{p}_{i,k+1}^n \end{bmatrix}, & \tilde{\mathbf{u}}_{i,k} &= \begin{bmatrix} \tilde{\mathbf{u}}_{i,k-1} \\ \tilde{\mathbf{u}}_{i,k} \\ \tilde{\mathbf{u}}_{i,k+1} \end{bmatrix}, & \mathbf{u}_{i,k} &= \begin{bmatrix} \mathbf{u}_{i,k-1} \\ \mathbf{u}_{i,k} \\ \mathbf{u}_{i,k+1} \end{bmatrix}. \end{aligned} \quad (3.62)$$

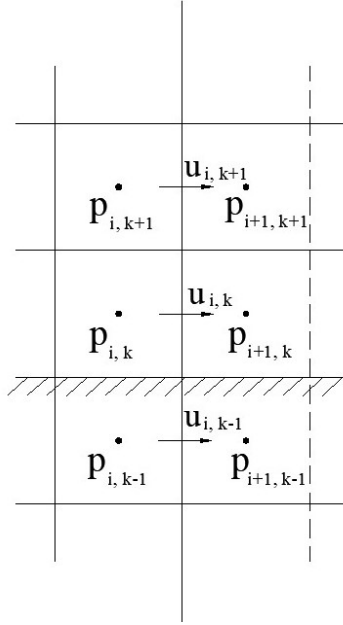


Figure 3.4: The solution variables below the bottom are determined from the constant extrapolation of the solution variables above the bottom

Upon substitution of the expressions from (3.59) to (3.62) into the equation (3.58) and applying the notations given in (3.62), a discrete equation for the absorbing boundary conditions is obtained:

$$\begin{aligned}
 & (\mathcal{K}_{rl} \ \mathcal{K}_{rc} \ \mathcal{K}_{rr}) \mathbf{p}_{i+1,k}^{n+1} + (\mathcal{K}_{zl} \ \mathcal{K}_c \ \mathcal{K}_{zr}) \mathbf{p}_{i,k}^{n+1} + (\mathcal{K}_{ll} \ \mathcal{K}_{lc} \ \mathcal{K}_{lr}) \mathbf{p}_{i-1,k}^{n+1} \\
 & = (\mathcal{N}_{zl} \ \mathcal{N}_c \ \mathcal{N}_{zr}) \hat{\mathbf{u}}_{i,k} + (\mathcal{N}_{ll} \ \mathcal{N}_{lc} \ \mathcal{N}_{lr}) \hat{\mathbf{u}}_{i-1,k} + (\mathcal{O}_{zl} \ \mathcal{O}_c \ \mathcal{O}_{zr}) \mathbf{u}_{i,k}^n \\
 & + (\mathcal{R}_{zl} \ \mathcal{R}_c \ \mathcal{R}_{zr}) \mathbf{p}_{i,k}^n + (\mathcal{R}_{rl} \ \mathcal{R}_{rc} \ \mathcal{R}_{rr}) \mathbf{p}_{i+1,k}^n.
 \end{aligned} \tag{3.63}$$

The matrix coefficients in  $\mathcal{K}$  depend on the variables  $\gamma, \epsilon, \lambda, \kappa, \varphi, \psi$  and  $\chi$ . The coefficients in  $\mathcal{N}$  are combinations of the variables  $\lambda, \kappa, \varphi, \chi$  and  $\tau$ .  $\mathcal{O}$  contains  $\lambda, \varphi$  and  $\chi$ .  $\mathcal{R}$  is only related to the variable  $\lambda$ . Detailed expressions for these matrix coefficients are given in Appendix C.

### Discretization of ABCs at the free surface and the bottom

The second derivatives of the pressures and velocities in the vertical direction from three horizontal layers are required, as can be observed in the pressure Poisson equations (3.56) and (3.63). However, no solution variables are calculated above the free surface in one-phase flow simulations and thus only the solutions below the free surface are available, see Fig. 3.3. The second derivatives of the velocities and pressures, which use only one-sided information, may result in unstable simulations. Therefore,

in the **Surface** cells the Sommerfeld condition (3.23) or (3.32), with a prescribed coefficient  $c_k$ , is implemented at the cost of accuracy.

Similarly in Fig. 3.4, no solution variables are determined below the bottom of the computational domain. Therefore, constant extrapolation is applied to the velocity below the bottom, i.e.  $u_{b,k-1} = u_{b,k}$ . For the pressure below the bottom hydrostatic pressure is assumed, which results in  $p_{b,k-1} = p_{b,k} + gz_{b,k-1}$ .

# Chapter 4

## Verification Results

In this chapter, the absorbing boundary conditions incorporating uniform currents that were derived in Chapter 3 are verified through comparison with analytical solutions. Firstly, the first-order Sommerfeld-inspired condition (S-1) in Eq. (3.38) including uniform current is tested through a series of numerical simulations of regular waves on top of various currents. Secondly, the first-order generating and absorbing boundary condition (GABC-1) with current in Eq. (3.40) is verified by means of regular and irregular waves in the presence of different current velocities. Both following currents, which propagate in the same direction of waves, and opposing currents, which propagate in the opposite direction of waves, are considered. Lastly, the second-order absorbing boundary condition (ABC-2) in Eq. (3.41) with current is investigated via a sphere oscillating in a uniform current. The oscillating sphere produces waves radiating outward in all directions such that following, opposing and normal currents are all contained in one simulation.

### 4.1 Tests: Regular waves on currents

In this section, the first-order Sommerfeld-inspired condition (S-1) and the generating and absorbing boundary conditions (GABC-1) in the presence of uniform currents are verified through numerical simulations of regular waves on currents in truncated domains. The condition S-1 with current in Eq. (3.38) is only perfectly absorbing for a single wave component, while the GABC-1 in Eq. (3.40) can deal with dispersive properties of waves.

Since there is only one phase velocity for a regular wave, the second-order Sommerfeld-inspired condition (S-2) and the absorbing boundary condition (ABC-2), which both contain two celerities, are beyond the necessity for preventing reflections and thus are verified later.

### 4.1.1 S-1 with current

First, the condition S-1 with uniform current, containing a fixed celerity  $c_k$ , is studied in a two dimensional domain. It is applied on the domain boundaries of 25 simulations, in which 25 regular waves with different wave numbers are investigated. For each case, six currents, including three following and three opposing ones, have been studied while keeping the water depth constant. Since the condition S-1 with current performs best for one  $kh$  value which it has been tuned for, numerical reflections can be expected for the other 24 wave components which are away from that  $kh$  value. Here  $k$  and  $h$  denote the wave number and water depth, respectively. The performance of the condition S-1 with current for different wave components can be assessed in comparison with the theoretical reflection.

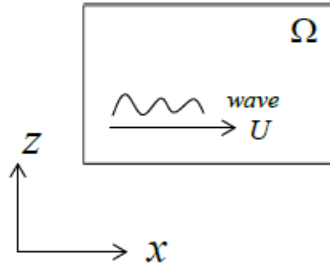


Figure 4.1: Sketch of a computational domain.  $\Omega$  denotes the domain area and  $U$  represents the current.

### Setup of the simulations

The simulations start from uniform current. The surface and velocity signals of regular waves at the inflow boundary are ramped up over two wave periods to minimize initialization errors. The sketch of a computational domain is depicted in Fig. 4.1.

The water depth  $h$  is chosen as 10 m for all simulations. 25 values for the  $kh$  of regular waves vary from 0.2 to 5.0 evenly. We will see later that this range of  $kh$  values is what the condition GABC-1 with current is designed accurately for. For convenience, here we use the same range of  $kh$  values to test the condition S-1 with current. This indicates that their wavelengths span in the range of [12.57 m, 314.16 m]. Considering the range of current velocities in this work, the corresponding wave periods are from 2.55 s to 40 s. A height of  $H_w = 1.0$  m is specified to all waves. In this way, waves, spanned from linear ones to mildly steep ones in waters from being quite shallow to being deep, are considered.

Three following currents with speeds  $U = 0.5$  m/s, 1.0 m/s, 2.0 m/s and three opposing currents  $U = -0.5$  m/s, -1.0 m/s, -2.0 m/s, which are commonly observed in reality, are investigated. The domain length  $L_d$  is selected to be 1.5 times of the wavelength  $L_w$  and thus 25 domain lengths for each current speed are specified. In

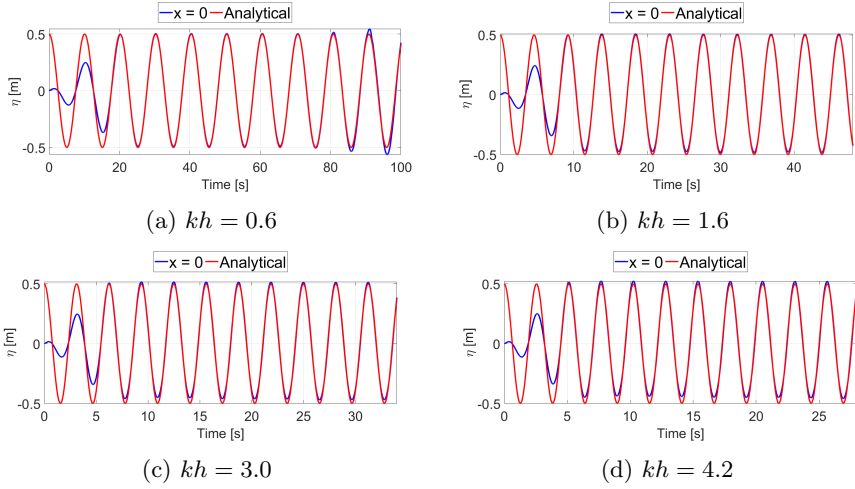


Figure 4.2: Comparison between simulated and theoretical surface elevation at inflow boundary for different waves in a following current:  $U = 1.0 \text{ m/s}$

total, 150 simulations have been performed to assess the condition S-1 with current. The simulation duration is always 6 times of  $L_d / c_g$ , therefore, the duration is different for each simulation and the wave energy (group velocity  $c_g$ ) travels 6 domain lengths in this duration.

The grid resolution  $dx$  in horizontal direction is chosen to be  $0.25 \text{ m}$  in each simulation, with which at least 60 cells per wave length is guaranteed. The vertical grid size  $dz$  is fixed and also specified as  $0.25 \text{ m}$ . The time step  $dt$  changes with the wave period  $T_w$  in each simulation. It is specified as  $T_w / 100$  initially and is adjusted automatically to satisfy the CFL criterion. The reader is referred to Kleefsman (2005) for more information. The parameter  $c_k$  in the condition S-1 including current is designed to perform best for  $k = 0.16$ , with a corresponding wave length  $\lambda = 39.25 \text{ m}$ . Using these settings, the number of cells in the 25 cases ranges from 3620 to 90480 and the run time takes from 7 minutes to three hours.

### Surface elevations for regular waves in currents

Before comparing the numerical reflection coefficients with the analytical solutions for regular waves in currents, their surface elevations calculated from ComFLOW are compared with the theoretical results.

$$\eta_w = \frac{A'(\omega - \mathbf{k} \cdot \mathbf{U})}{g} \cos(|\mathbf{k}|h) \cos(\mathbf{k} \cdot \mathbf{x} - \omega t). \quad (4.1)$$

In the previous chapter, we derived the linearized kinematics boundary condition at the free surface for waves in current, which reads:

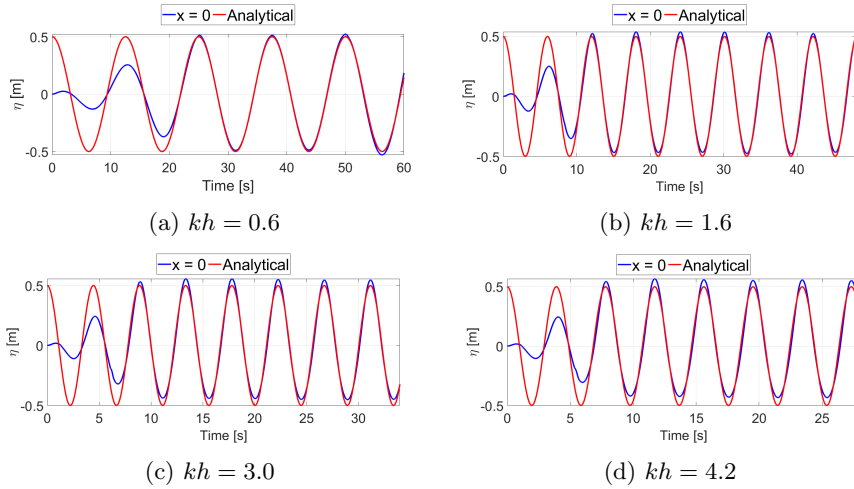


Figure 4.3: Comparison between simulated and theoretical surface elevation at inflow boundary for different waves in an opposing current:  $U = -1.0 \text{ m/s}$

$$\frac{\partial \eta_w}{\partial t} + \mathbf{U} \cdot \nabla \eta_w = \frac{\partial \phi_w}{\partial z} \Big|_{z=\eta}. \quad (4.2)$$

The velocity potential due to waves (only)  $\phi_w = A' \cosh |\mathbf{k}|(z+h) \sin(\mathbf{k} \cdot \mathbf{x} - \omega t)$ . Setting  $\frac{A'(\omega - \mathbf{k} \cdot \mathbf{U})}{g} \cos(|\mathbf{k}|h) = a$  where  $a$  is the amplitude of waves in current, then the analytical surface elevation for waves in current is described as:

$$\eta_w = a \cos(\mathbf{k} \cdot \mathbf{x} - \omega t). \quad (4.3)$$

Here numerical surface elevations for four waves with the  $kh$  values of 0.6, 1.6, 3.0 and 4.2, representing different wave steepness, on top of two currents  $U = 1.0 \text{ m/s}$  and  $-1.0 \text{ m/s}$  are presented, in comparison with the analytical results. As illustrated in Fig. 4.2 and 4.3, the dis-match in the first two wave periods of all figures is because that the input wave is sent into the computational domain gradually with a ramp function over two wave periods.

For the cases of  $kh = 0.6$  and 1.6, in the presence of both a following current  $U = 1.0 \text{ m/s}$  and an opposing current  $U = -1.0 \text{ m/s}$ , the numerical input waves agree well with the analytical solutions, which are illustrated in Fig. 4.2a, 4.2b, 4.3a and 4.3b. For steeper waves such as in Fig. 4.2c and 4.2d, 4.3c and 4.3d, there is a slight offset above the equilibrium position  $\eta = 0$ .

With the verified input waves for all cases, we demonstrate the time evolution of these waves at different positions in the domain. Time series of waves with the same  $kh$  values in different currents are shown from Fig. 4.4 to 4.7. Since there is phase lag at different positions, the results inside the domain and at the outflow boundary

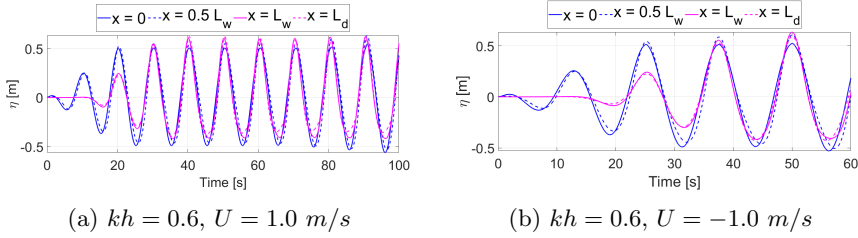


Figure 4.4: Numerical surface elevations of the wave  $kh = 0.6$  at different positions in two currents:  $U = 1.0$  m/s (left),  $U = -1.0$  m/s (right).  $L_w$  is the wavelength and  $L_d = 1.5 L_w$  is the domain length

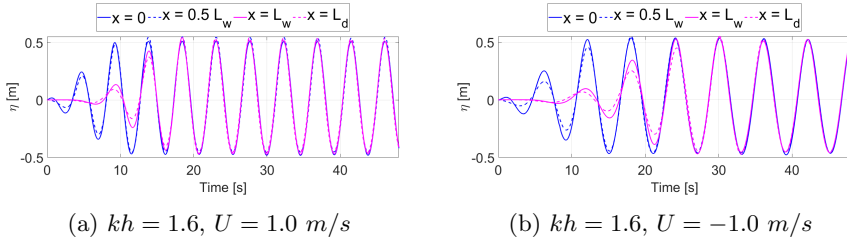


Figure 4.5: Numerical surface elevations of the wave  $kh = 1.6$  at different positions in two currents:  $U = 1.0$  m/s (left),  $U = -1.0$  m/s (right)

are shifted to coincide with those at the inflow boundary for comparison.

As can be observed for all waves of different lengths, the start-up interval becomes longer when the monitoring point moves from the inflow boundary  $x = 0$  further to the outflow boundary  $x = L_d = 1.5 L_w$ . Since the input waves are linearly ramped up in two wave periods into the domain, the wave at  $x = 0$  is fully developed after two wave periods, which are depicted by solid blue lines. Compared to the wave signal at  $x = 0$ , there is a delay of 0.5, 1.0 and 1.5 times of the wave periods for the waves to be fully developed at the position  $x = 0.5 L_w$ ,  $x = L_w$  and  $x = 1.5 L_w$ , which are given in dashed blue lines, solid magenta lines and dashed magenta lines, respectively. The wave heights decrease gradually from the inflow boundary to the outflow boundary due to numerical damping. In particular, numerical damping is clearly observed in the case of opposing current. The wave amplitude at the outflow end is 10% smaller than that at the inflow boundary for the wave  $kh = 3.0$ . For the steeper wave  $kh = 4.2$ , the damping of the amplitude is 12%.

The main reason is that the combination of a mean opposing current, waves and a first-order upwind discretisation yields a numerical scheme with a large amount of dissipation. The thesis focuses on the boundary conditions and does not investigate

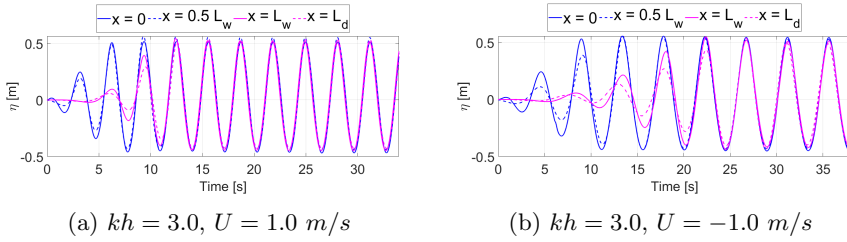


Figure 4.6: Numerical surface elevations of the wave  $kh = 3.0$  at different positions in two currents:  $U = 1.0$  m/s (left),  $U = -1.0$  m/s (right)

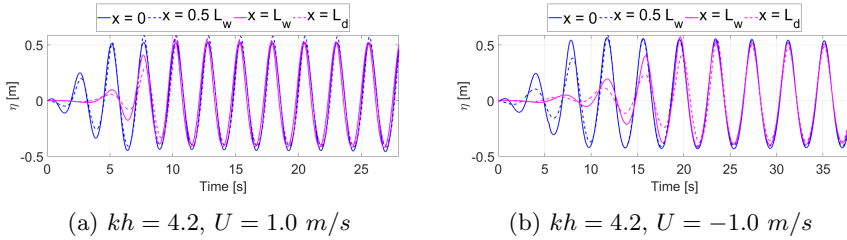


Figure 4.7: Numerical surface elevations of the wave  $kh = 4.2$  at different positions in two currents:  $U = 1.0$  m/s (left),  $U = -1.0$  m/s (right)

this issue.

### Theoretical reflections

The boundary condition  $S$ -1 with current is verified by comparing the numerical reflection coefficients in the wave and current simulations with corresponding theoretical ones. The theoretical reflection coefficient for regular waves on uniform current in a one dimensional domain is derived in Appendix A as:

$$R = - \left( \frac{k_{out}}{\omega} - \frac{1}{c_{bc} + U} \right) / \left( \frac{k_{refl}}{\omega} - \frac{1}{c_{bc} + U} \right) \quad (4.4)$$

Here,  $c_{bc}$  is the coefficient specified as an input for the condition  $S$ -1.  $k_{out}$  and  $k_{refl}$  represent the wave numbers of the outgoing and reflected waves, respectively. Given a certain wave frequency  $\omega$ , the wave number of reflected wave  $k_{refl}$  is determined by solving the dispersion relation using Newton's method.

### Numerical reflections

To obtain the numerical reflection coefficient, the outgoing and reflected waves should be distinguished at their respective wave numbers from the wave signals in the do-

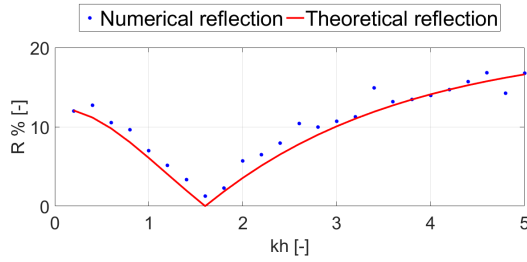


Figure 4.8: Comparison between simulated and theoretical reflection coefficients for regular waves on following current:  $U = 0.5 \text{ m/s}$

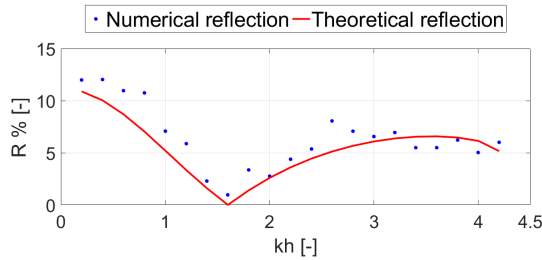


Figure 4.9: Comparison between simulated and theoretical reflection coefficients for regular waves on following current:  $U = 1.0 \text{ m/s}$

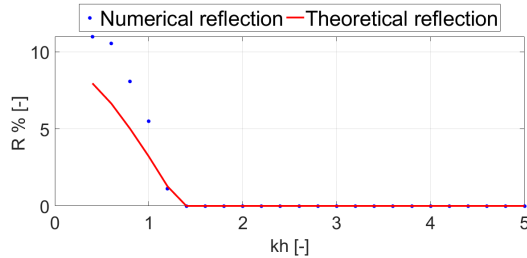


Figure 4.10: Comparison between simulated and theoretical reflection coefficients for regular waves on following current:  $U = 2.0 \text{ m/s}$

main. The time history of the surface elevation at all grid points in the computational domain is adopted to perform Fourier analysis in both space and time. The 2-D fast Fourier transform function `fft2` in Matlab is used to operate on the surface elevations, which results in the wave amplitudes at a series of wave numbers. The wave numbers decomposed from the Fourier transform are located in the range  $-2\pi[-N_x/2 : N_x/2 - 1]/(N_x\Delta x)$ , in which  $N_x$  is the grid number in  $x$ - direction and  $\Delta x$  is the grid size. The numbers of time instances and time steps are denoted by  $N_t$  and  $\Delta t$ , respectively.

It can be observed that the wave signals are decomposed into two parts: one with positive wave numbers and the other with negative wave numbers. The part with negative wave numbers corresponds to reflected waves. The wave amplitudes at their respective wave numbers can be obtained and the ratio of these two values is the numerical reflection coefficient. This method is suitable for regular waves.

Note that for irregular waves there are some other widely-used methods to separate incident and reflected waves. For example, a 2-point method was proposed by Goda and Suzuki (1976). Here a simultaneous recordings of wave profiles is made at two adjacent locations on a line parallel to the direction of wave propagation. Since the 2-point method has limitations, Mansard and Funke (1980) proposed a 3-point approach, which uses a least square analysis for decomposing the measured spectra into incident and reflected spectra with greater accuracy and range.

### Results of reflection coefficients for regular waves in currents

To measure the accuracy of the boundary condition S-1 with a current, the numerical reflection coefficients obtained from the above 150 test cases are compared with the theoretical ones.

It is observed from Fig. 4.8, for the current velocity  $U = 0.5 \text{ m/s}$ , that the simulated reflections agree well with theory for all  $kh$  values. The condition S-1 including current is designed to perform best for  $kh = 1.6$ . Correspondingly, the minimum numerical reflection is close to zero for the same  $kh$ . Away from that  $kh$ , the reflections increase in both simulations and theory.

Fig. 4.9 presents the results for a larger current  $U = 1.0 \text{ m/s}$ . The numerical reflection coefficients are slightly off the analytical solutions. However, they share the mean trend. The reflected waves do not exist for  $kh$  values larger than 4.2, because the group velocities of these waves become smaller than the current speed and thus the reflected waves are blocked by the current.

The reflection coefficients for the case  $U = 2.0 \text{ m/s}$  are presented in Fig. 4.10. For the  $kh$  values smaller than 1.4, the numerical results agree well with their corresponding theoretical values. There is no reflection for the  $kh$  values larger than 1.4, because these reflected wave modes have been blocked by the current and cannot exist.

The numerical reflection coefficients for regular waves on top of opposing currents are also compared with the theoretical values. The results for the current  $U = -0.5 \text{ m/s}$  and  $U = -1.0 \text{ m/s}$  are shown in Fig. 4.11 and 4.12. The simulated reflections show similar tendency and are in good agreement with theory.

With an increasing opposing current  $U = -2.0 \text{ m/s}$ , the reflections for the waves of  $kh$  values larger than 2.4 are hardly obtained, see Fig. 4.13 due to excessive dissipation.

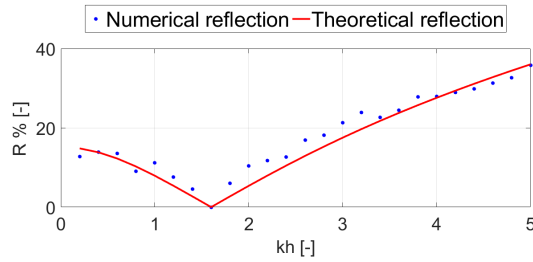


Figure 4.11: Comparison between simulated and theoretical reflection coefficients for regular waves on opposing current:  $U = -0.5 \text{ m/s}$

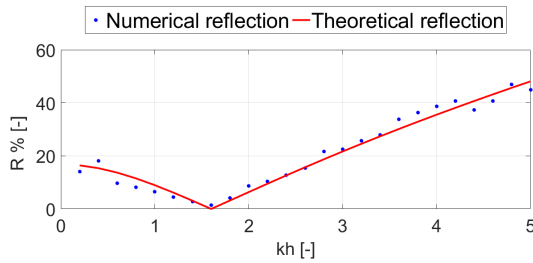


Figure 4.12: Comparison between simulated and theoretical reflection coefficients for regular waves on opposing current:  $U = -1.0 \text{ m/s}$

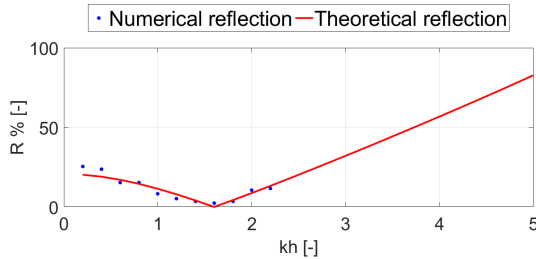


Figure 4.13: Comparison between simulated and theoretical reflection coefficients for regular waves on opposing current:  $U = -2.0 \text{ m/s}$

### 4.1.2 GABC-1 with current

In the above tests, the boundary condition  $S$ -1 with current can only be perfect for one certain wave component and current. However, a wave in reality is often composed by the superposition of a number of components. Each individual component has its own wave number. To account for the dispersive properties of waves, the parameter  $c$  in the Sommerfeld-inspired condition needs to be approximated, which results in GABC-1. The condition GABC-1 is designed to be accurate over a range of  $kh$  values. A better approximation of the dispersion relation leads to a lower reflection. In this

section, the boundary condition GABC-1 including current is verified by means of the test cases of 25 regular waves, each combined with six different currents.

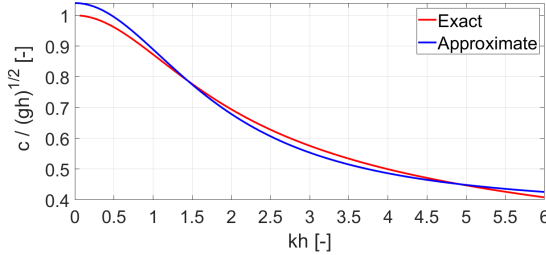


Figure 4.14: Approximation of the dispersion relation

### Setup of the simulations

The parameters specified for waves and currents are exactly the same as in the test of the condition S-1 with current. The wave has a height of  $H_w = 1.0$  m and the water depth  $h$  is 10 m for all simulations. Three following currents with speeds  $U = 0.5, 1.0, 2.0$  m/s and three opposing currents  $-0.5, -1.0, -2.0$  m/s are accounted for. 25 values for  $kh$  of the monochromatic waves vary from 0.2 to 5 evenly. The domain length  $L_d$  is selected to be one and a half wavelength  $L_w$  and thus 25 domains are specified. The simulation duration is always 6 times of  $L_d / c_g$ , therefore, the duration is different for each simulation and the wave energy (group velocity  $c_g$ ) travels 6 domain lengths in this duration.

The only difference from the test of the condition S-1 is that the condition GABC-1 is applied at the domain boundaries. In this study, the coefficients in the boundary condition GABC-1 are chosen such that the dispersion relation of the waves with the  $kh$  in the range  $(0, 6)$  are approximated well. With  $a_0 = 1.04$ ,  $a_1 = 0.106$ , and  $b_1 = 0.289$ , the approximate dispersion relation is illustrated in Fig. 4.14.

### Surface elevations for regular waves in currents

In the same fashion as for the condition S-1 with current, the numerical surface elevations at the inflow boundary for four waves are compared to analytical solutions for a following current  $U = 1.0$  m/s and an opposing current  $U = -1.0$  m/s, see Fig. 4.15 and 4.16. The good agreement implies that the waves are sent into the domain correctly. For these two current velocities, time series of waves with the same  $kh$  values at different positions in the domain are shown from Fig. 4.17 to 4.20. Similar to the results for the condition S-1 with current, the numerical damping in the wave amplitude occurs. As shown in Fig. 4.19b and 4.20b, for the steep waves  $kh = 3.0$  and  $kh = 4.2$  in the opposing current  $U = -1.0$  m/s, the numerical damping at the outflow end is 9.5% and 12.5% respectively.

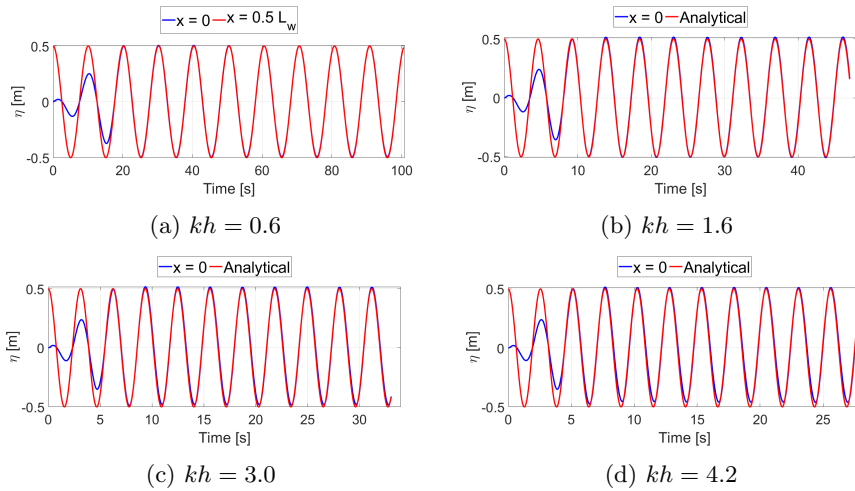


Figure 4.15: Comparison between simulated and theoretical surface elevation at inflow boundary for different waves in current:  $U = 1.0 \text{ m/s}$

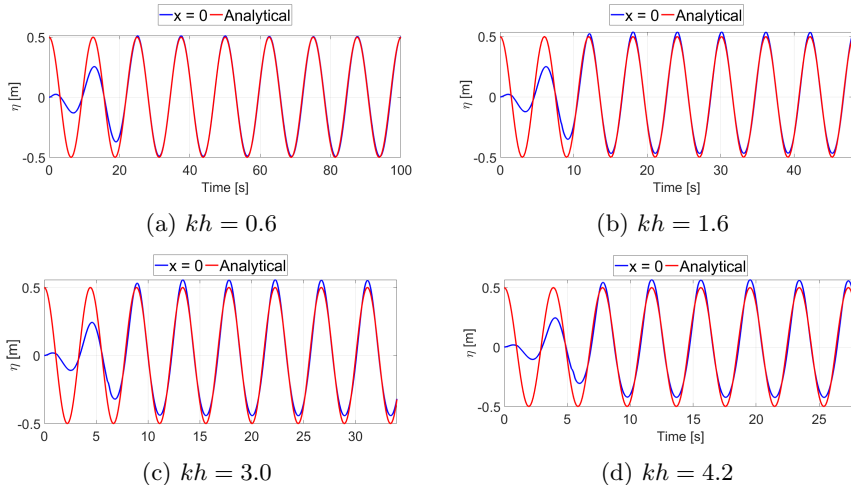


Figure 4.16: Comparison between simulated and theoretical surface elevation at inflow boundary for different waves in current:  $U = -1.0 \text{ m/s}$

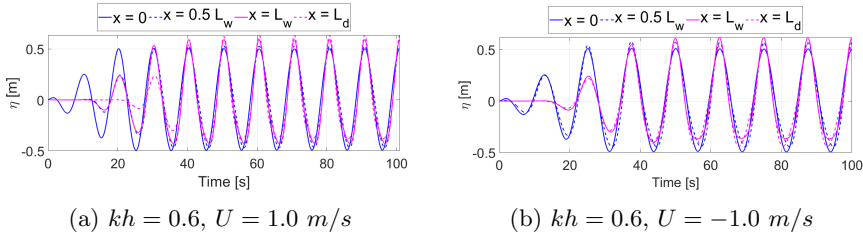


Figure 4.17: Numerical surface elevations of the wave  $kh = 0.6$  at different positions in two currents:  $U = 0.5$  m/s (left),  $U = 1.0$  m/s (right).  $L_w$  is the wavelength and  $L_d = 1.5 L_w$  is the domain length

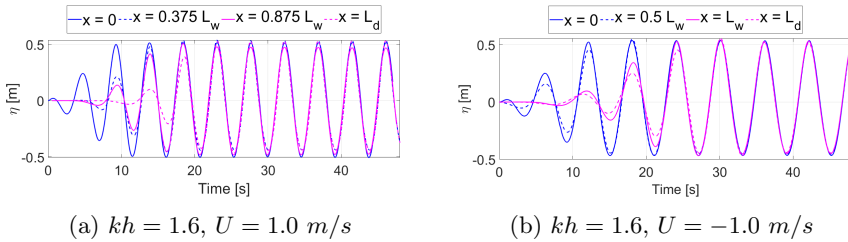


Figure 4.18: Numerical surface elevations of the wave  $kh = 1.6$  at different positions in two currents:  $U = 1.0$  m/s (left),  $U = -1.0$  m/s (right)

The nonlinearity of the surface elevations is clearly observed. In this thesis, the FFT approach is adopted to separate incident and reflected waves for these cases. A nonlinear method was proposed by Andersen et al. (2017), in which the nonlinear wave celerity was used to overcome the amplitude dispersive effect of nonlinear waves. This nonlinear approach separates the superharmonics into bound/free and incident/reflected components.

### Results of reflection coefficients for regular waves in currents

To measure the accuracy of the GABC-1 with current, the numerical reflection coefficients obtained from the above 150 test cases are compared with the theoretical ones. They are presented from Fig. 4.21 to 4.26, which correspond to the following currents  $U = 0.5, 1.0, 2.0$  m/s and the opposing currents  $U = -0.5, -1.0, -2.0$  m/s respectively. All the simulated reflection coefficients are lower than 6%, which are much smaller than those obtained from the condition S-1 including current for the corresponding same six currents, see Fig. 4.8 to 4.13. More detailed observations for the results obtained from the condition GABC-1 including current are given as below. It is observed from Fig. 4.21, for the current  $U = 0.5$  m/s, that the simulated reflections are somewhat larger than analytical values but lower than 6%. This indicates

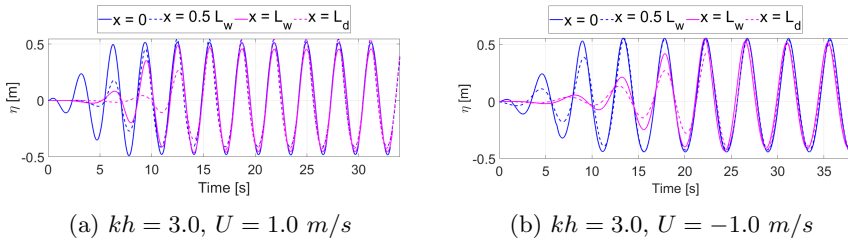


Figure 4.19: Numerical surface elevations of the wave  $kh = 3.0$  at different positions in two currents:  $U = 1.0$  m/s (left),  $U = -1.0$  m/s (right)

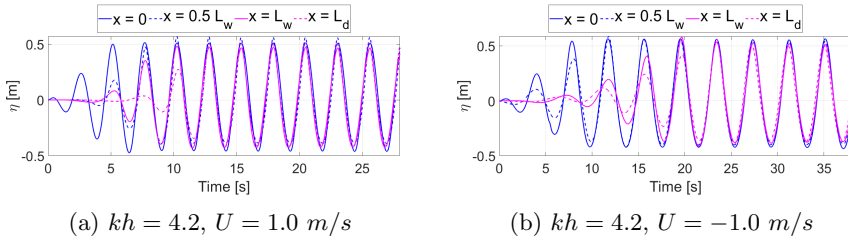


Figure 4.20: Numerical surface elevations of the wave  $kh = 4.2$  at different positions in two currents:  $U = 1.0$  m/s (left),  $U = -1.0$  m/s (right)

that the reflected waves with the  $kh$  values between 0 and 5 in the current  $U = 0.5$  m/s are absorbed well with our boundary condition.

Similar results are obtained for the current speed  $U = 1.0$  m/s, see Fig. 4.22. There is no reflection for the  $kh$  values that are larger than 4.2, because the reflected waves have been blocked by the current.

The reflection coefficients for the case  $U = 2.0$  m/s are presented in Fig. 4.23. The reflected waves do not ever exist for  $kh$  values larger than 1.4, because the group velocities of these waves become smaller than the current speed and thus the reflected waves are blocked by the currents. For the waves of  $kh$  smaller than 1.4, the numerical reflections are less than 4%.

The numerical reflection coefficients for regular waves on top of opposing currents are also compared with the theoretical values. The result for the current  $U = -0.5$  m/s is shown in Fig. 4.24. On the whole, the simulated reflections are larger than their theoretical counterparts, but for all the  $kh$  are less than 5%. Given a stronger opposing current  $U = -1.0$  m/s, the simulated reflections show similar tendency and are in good agreement with theory, see Fig. 4.25.

However, with an increasing opposing current  $U = -2.0$  m/s, the reflections in Fig.

4.26 for the waves of the  $kh$  values larger than 2.4 are difficult to obtain due to excessive dissipation. Four  $kh$  values, representing different wave steepness, have been chosen to show these dissipation, see Fig. 4.27. The envelopes in the figure are determined from the maximum surface elevations during the simulation at each position.

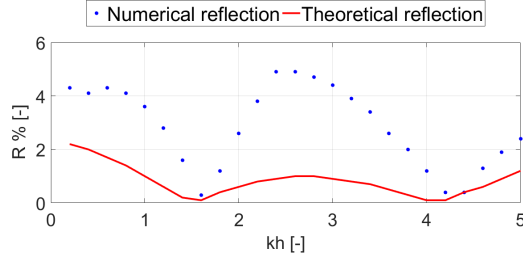


Figure 4.21: Comparison between simulated and theoretical reflection coefficients for regular waves on following current:  $U = 0.5 \text{ m/s}$

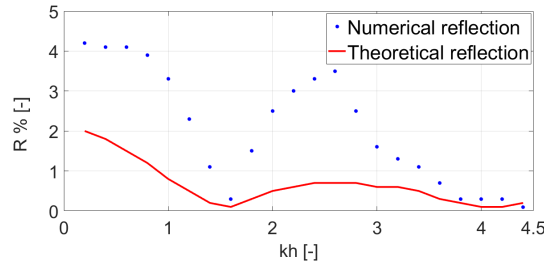


Figure 4.22: Comparison between simulated and theoretical reflection coefficients for regular waves on following current:  $U = 1.0 \text{ m/s}$

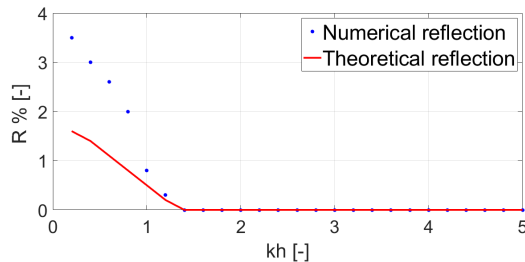


Figure 4.23: Comparison between simulated and theoretical reflection coefficients for regular waves on following current:  $U = 2.0 \text{ m/s}$

As can be observed when the  $kh$  increases the wave dissipation gets larger. For example, in the case of a very short wave with  $kh = 4.0$ , more than 70% of the wave amplitudes are dissipated. It is not clear about the causes of this excessive

dissipation in the case of opposing current  $U = -2.0 \text{ m/s}$  and requires further study in the future. As a preliminary investigation, we plot the dissipation for the same four  $kh$  with following current  $U = 2.0 \text{ m/s}$  in Fig. 4.28. In this case, the dissipation is acceptable.

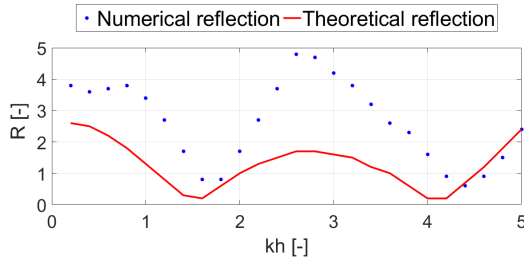


Figure 4.24: Comparison between simulated and theoretical reflection coefficients for regular waves on opposing current:  $U = -0.5 \text{ m/s}$

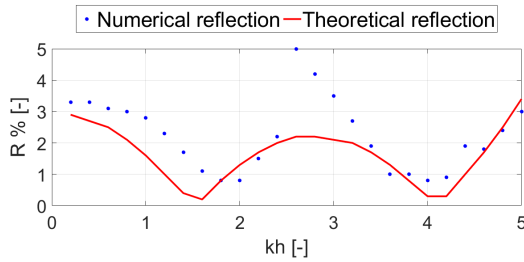


Figure 4.25: Comparison between simulated and theoretical reflection coefficients for regular waves on opposing current:  $U = -1.0 \text{ m/s}$

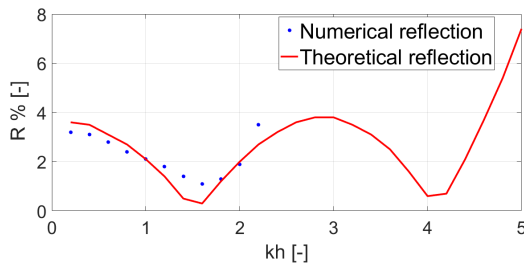


Figure 4.26: Comparison between simulated and theoretical reflection coefficients for regular waves on opposing current:  $U = -2.0 \text{ m/s}$

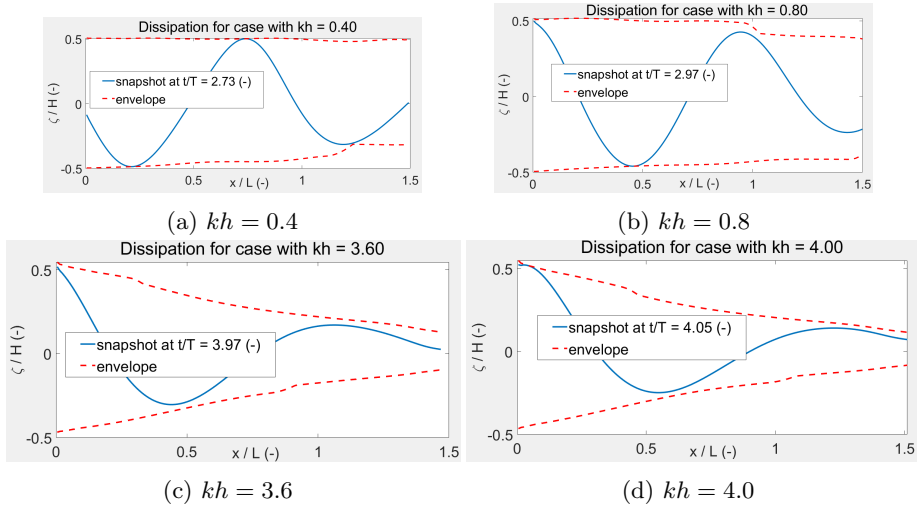


Figure 4.27: Dissipation for four  $kh$  in the opposing current:  $U = -2.0 \text{ m/s}$

## 4.2 Tests: irregular waves on currents

To further test the boundary condition GABC-1 with current, which is mainly designed for simulations of long-crested irregular waves on top of uniform current in truncated domains, tests of irregular waves in combination with following and opposing currents will be performed in a 2D computational domain.

The performance of the boundary condition is measured by means of the reflection coefficients. A JONSWAP wave spectrum, see Table 4.1, on top of a current simulation, with GABC-1 at both inflow and outflow end of the domain, is adopted to obtain the numerical reflection coefficients, which are compared with the theoretical counterparts.

### Setup of the simulations

Four simulations have been performed, in which the above JONSWAP spectrum, which is a narrow-banded spectrum, travels on top of a following current:  $1.0 \text{ m/s}$  and an opposing current:  $-0.5 \text{ m/s}$ , respectively. For each current, two simulations in a small domain of the length  $400 \text{ m}$  and a large domain of the length  $10000 \text{ m}$  are carried out. The finest grid size in both  $x$  and  $z$ - directions is  $0.5 \text{ m}$ . The duration of the simulations is specified as  $1200 \text{ s}$  for the accuracy of the Fourier transform. For the shortest incident wave period that has energy, 200 time steps per period are applied. For the smallest incident wavelength that has energy, 12 cells per wavelength are adopted. For those wave components the effect of numerical dispersion is not negligible. It is a compromise to obtain a reference solution without reflection in the large domain within a reasonable amount of time. The simulation took 36 hours in

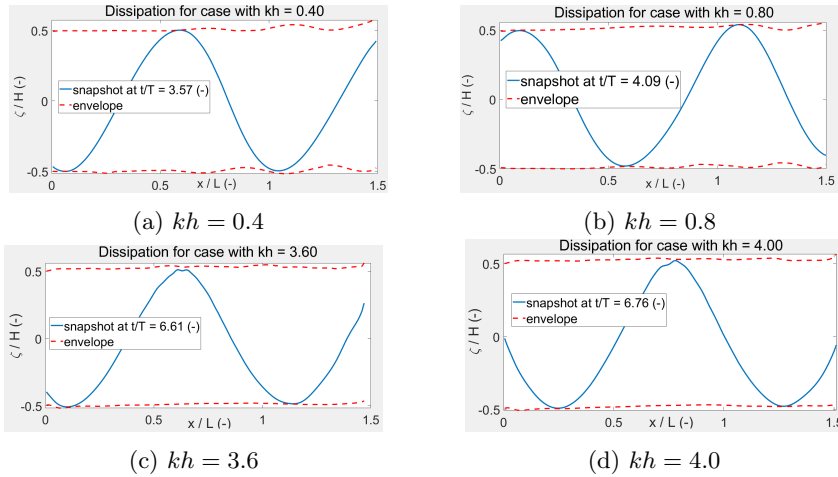


Figure 4.28: Dissipation for four  $kh$  in the following current:  $U = 2.0 \text{ m/s}$

the large domain and 25 minutes in the short domain to finish.

The simulations start from uniform current, i.e. there is a current in the whole domain and no waves at  $t = 0$ . Waves are imposed at the inflow side of the domain using linear wave potential theory. The surface elevation and velocities at the inflow boundary are gradually built up by means of linear ramp function over an interval of two significant wave periods.

The coefficients of the GABC-1 are given in Table 4.2. They are tuned in such a way that the reflection coefficients over the range of  $kh \in (0, 6]$  are less than 2%. The coefficient in the Sommerfeld condition applied at the surface cells, which is the phase velocity of the outgoing wave, is tuned according to the peak component in the spectrum.

Parameter	Value
Peak period	6.0 s
Significant wave height	2.0 m

Table 4.1: JONSWAP spectrum

### Numerical reflections

Here the procedure to extract the numerical reflection coefficients is different from what was used for regular waves, because the wave components in irregular waves propagate with different celerities and thus reach the domain boundaries at different

time instances. Another method proposed in Wellens (2012) is adopted. First, a wave simulation is performed in a large domain, which is large enough that during the entire duration reflected waves cannot reach the measurement location. The required domain length is determined from the phase velocity of the fastest propagating wave components and the duration of the simulation:  $L_d = \sqrt{gh}t_{max}$ . Here  $h$  is the water depth.

Parameter	Value
a0	1.04 [-]
a1	0.106 [-]
b1	0.289 [-]

Table 4.2: Coefficients of ABC

In the meantime, another simulation is carried out in a small domain. This simulation is same as the previous one in the large domain in every aspect, except for the domain length and the boundary condition applied at the outflow end of the domain. Measurements of the surface elevation in the small domain, taken at exactly the same positions, are compared to measurements in the large domain. Their difference can only be attributed to the boundary condition since everything else is same. The large domain and small domain, with the measurement location in the middle of the small domain, are illustrated in Fig. 4.29.

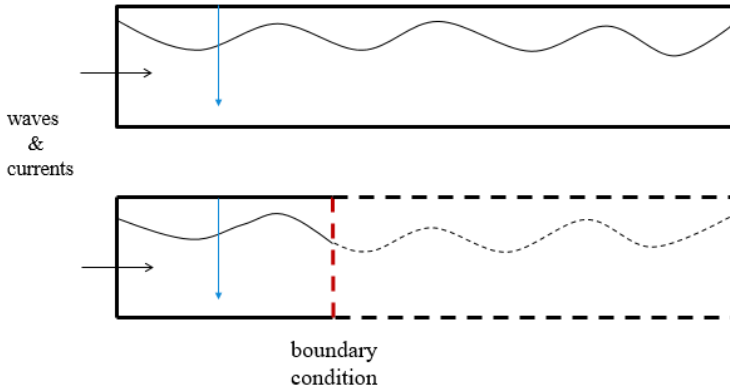


Figure 4.29: Large and small domains used to obtain reflected signals in the middle of the small domain

### Results for following current

Subtraction of the wave signal at the measurement location in the large domain from the wave signal in the small domain where the boundary condition GABC-1 is applied

results in a reflection signal. Subsequently, the wave signal in the large domain and the reflection signal are decomposed into their Fourier components, which are used to calculate the spectra and reflection coefficients. Note that this method disregards any nonlinearities such as wave-wave interactions. The resulting input spectrum, reflected spectrum and reflection coefficients will be compared with theory, see Fig. 4.30.

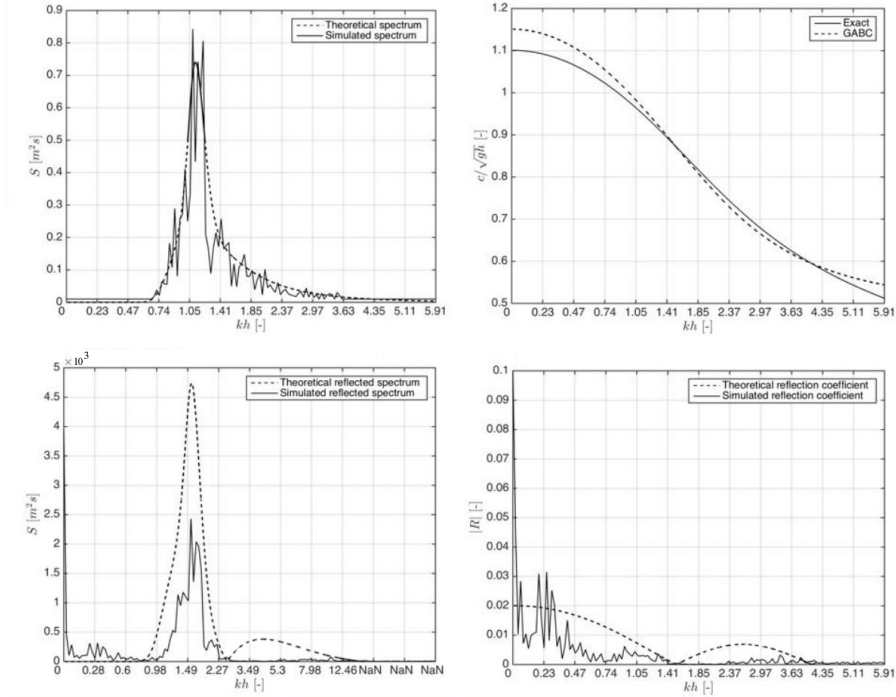


Figure 4.30: Input wave spectrum (top-left), Approximated dispersion relation (top-right), Reflected wave spectrum (bottom-left) and Reflection coefficients (bottom-right) obtained from the simulation in comparison with theory:  $U = 1.0$  m/s

First, the input spectrum obtained from the numerical simulation is given in the top-left figure, which shows reasonable agreement with the theoretical one. The reflected wave spectrum is shown in the bottom-left figure. A shift of the wave number of the reflected waves is visible due to the Doppler effect of the opposing current on the reflected waves. The  $kh$ -axis is different from that in the other three figures, since the reflected modes have shorter wavelengths compared to the outgoing modes in the presence of the following current.

The reflection coefficients in comparison with theory are illustrated in the bottom-right figure. The simulated reflections for the shorter waves are smaller than theory. This may be attributed to wave nonlinearity and insufficient grid resolution for these shorter waves. There is no more reflection for  $kh > 4.24$ , because the corresponding

reflected wave modes are blocked by the current.

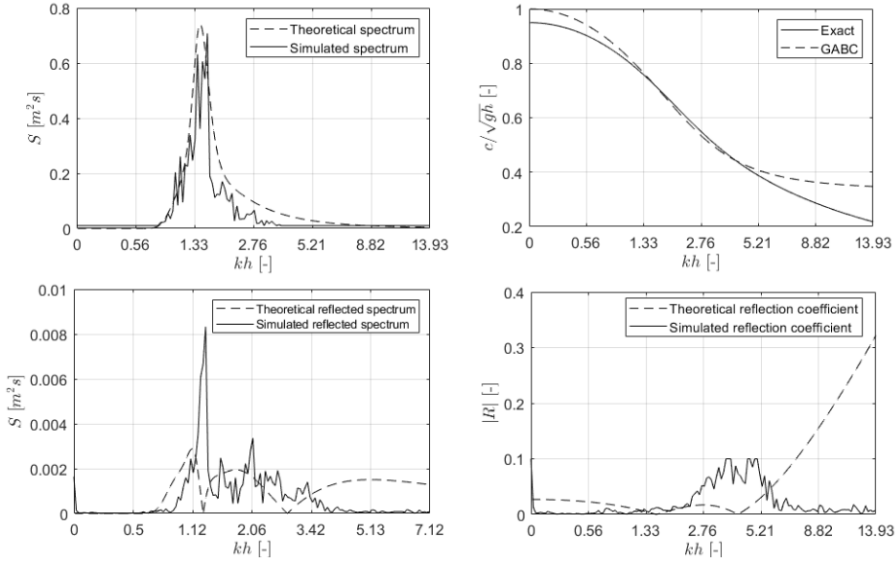


Figure 4.31: Input wave spectrum (top-left), Approximated dispersion relation (top-right), Reflected wave spectrum (bottom-left) and Reflection coefficients (bottom-right) obtained from the simulation in comparison with theory:  $U = -0.5 \text{ m/s}$

### Results for opposing current

The procedure to post-process the results of irregular waves in an opposing current is the same as what is used for a following current. Fig. 4.31 presents the input spectrum, reflected spectrum and reflection coefficients, which are numerically computed, in comparison with the analytical solutions.

As can be observed in the top-left figure, the numerical input spectrum agrees well with the analytical spectrum. Note that the  $kh$ -axis for the reflected spectrum (see the bottom-left figure) is different from that in the other three figures, because the reflected wave modes have longer wavelengths than the corresponding outgoing modes in the presence of the opposing current. The reflected wave energy around  $kh = 1.3$  is much larger than the theoretical values, which requires further study. For the other reflected wave components with  $kh < 3.8$ , which correspond with the outgoing modes with  $kh < 6$ , the reflected energy matches reasonably with theory.

In the bottom-right figure, the reflection coefficients for different wavelengths are presented. For the wave modes with  $3 < kh < 6$ , the reflection coefficients are larger than the analytical results. This deviation may be caused by the following reasons. Firstly, the nonlinear interaction of waves at the boundary is not accounted for, since the boundary condition is derived from the linear wave theory. Secondly, the op-

posing current increases the wave steepness, which adds to the nonlinear effects at the boundary. Thirdly, the procedure to post-process the numerical results may also contribute to this difference. The simulation duration is short compared to the peak period of the spectrum.

The simulated amounts of reflected wave energy for  $kh > 3.8$ , see the bottom-left figure, and the reflection coefficients, see the bottom-right figure, are worse than theory, because the boundary condition is not designed for these wave components.

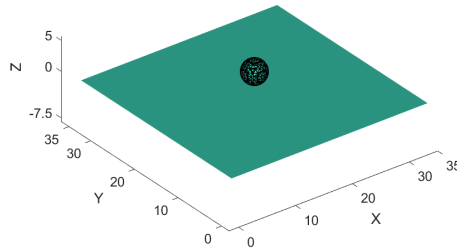


Figure 4.32: Initial position of the oscillating sphere

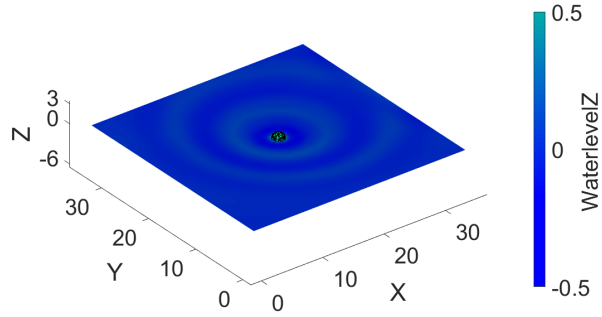
### 4.3 Oscillating sphere in currents

In this section, a solid sphere with a prescribed motion is oscillating on the water surface with a uniform current in a numerical tank. Wehausen and Laitone (1960) studied the analytical solutions of an oscillating source at forward speed. The oscillating sphere produces waves radiating outwards in all directions. Therefore, there are waves moving with following, opposing and normal currents in one simulation, which is interesting and helpful to verify the boundary condition with currents in 3D.

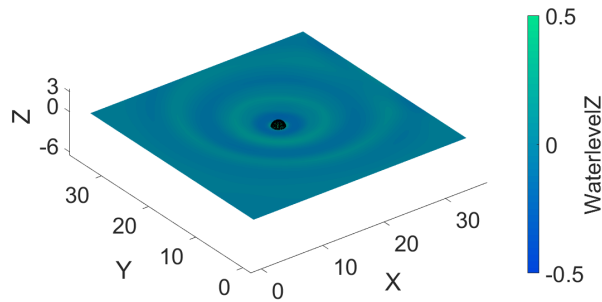
	Theoretical (m)	Numerical					
		0.5 m	Diff %	0.29 m	Diff %	0.17 m	Diff %
Following	10.04	11.31	12.65	9.74	2.99	9.43	6.08
Normal	7.92	9.19	16.04	7.71	2.65	8.01	1.14
Opposing	5.43	6.36	17.13	5.68	4.6	5.89	8.47

Table 4.3: Comparison of theoretical and numerical wavelengths in the directions of following, opposing and normal currents at  $t = 10.8$  s

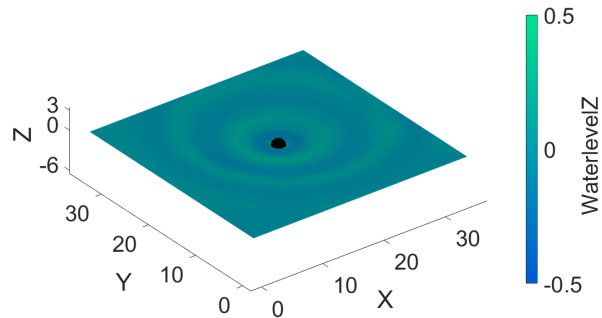
**Setup** The sphere with a radius of  $2$  m is initially located  $2$  m above the free surface, see Fig. 4.32 for the initial condition of the problem. The sphere is allowed to make only vertical motion along  $z$ -direction. Sinusoidal motion of the sphere is prescribed



(a) gird size: 0.5 m



(b) gird size: 0.29 m



(c) gird size: 0.17 m

Figure 4.33: Snapshots of numerical water surface elevations at  $t = 10.8s$

by  $z_s(t) = 1 + \cos 2.4t$ . The current has a speed of  $0.5 \text{ m/s}$  and propagates at  $45^\circ$  with the positive  $x$ -axis. After the impact of the sphere on the water surface initially with uniform current, a series of waves are produced radiating outward in all directions. The second-order boundary condition ABC-2 is used at the domain boundaries to absorb these waves and current, because it contains two angles and is designed for waves under different angles.

The domain lengths in both  $x$ - and  $y$ -directions are chosen as  $35 \text{ m}$ , to make sure that at least two wavelengths can be measured. The water depth is  $7.5 \text{ m}$ . Three simulations have been performed, with grid resolutions of  $0.5 \text{ m}$ ,  $0.29 \text{ m}$  and  $0.17 \text{ m}$ , respectively. The duration for both the simulations is  $10.8 \text{ s}$ , which ensures that the waves in each direction radiated from the oscillating sphere have fully reached the domain boundaries and have been reflected. In this way, the performance of the ABC-2 can be tested.

**Results** The wave lengths are calculated in each direction and compared with the theoretical values, see Table 4.3. With a small grid size in all three directions being  $0.17 \text{ m}$ , the numerical wave lengths in the directions of following, opposing and normal currents agree reasonably with the theoretical amounts.

The procedure to determine the wavelengths is explained as follows. Fig. 4.33 illustrates three snapshots from the simulations on three grids at  $t = 10.8 \text{ s}$ . As can be seen, smooth water surface fields are obtained on all grids, which indicates qualitatively that the boundary condition ABC-2 prevents wave reflections in all directions, including the direction of following, opposing and normal currents.

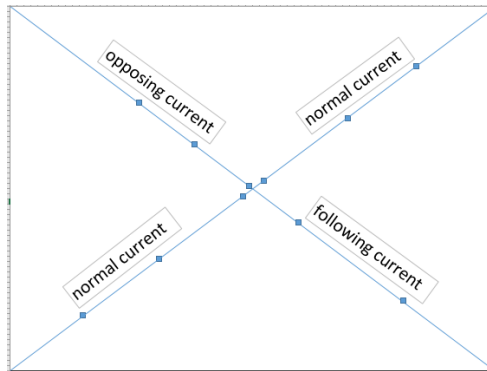


Figure 4.34: Sketch of wave lengths calculation in different directions from excel files

Further observations are expected to verify the boundary condition quantitatively. The water level in the entire numerical domain at  $t = 10.8 \text{ s}$  is exported to an excel file and used to obtain the wavelengths in the direction of following, opposing and normal currents. Fig. 4.34 shows a sketch how to obtain the wavelengths in these directions from excel files. Small blue markers in the figure show the highest values in each wave, which represent the wave crests. The wave length in each direction is

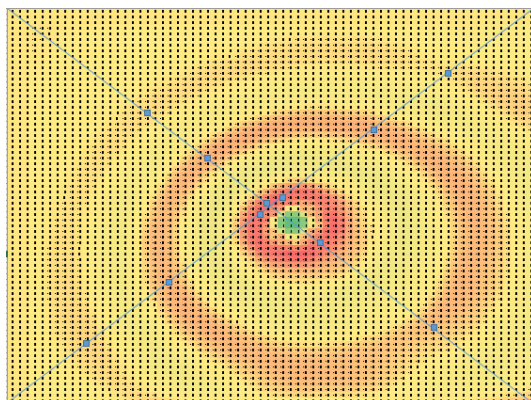
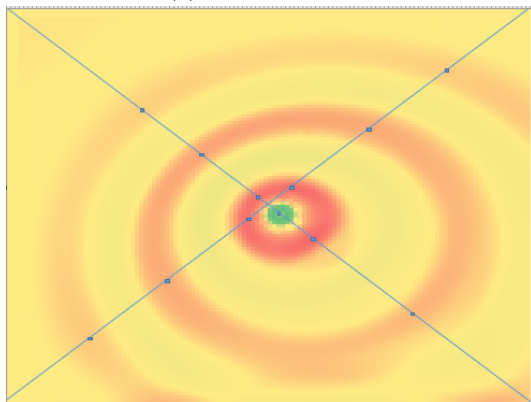
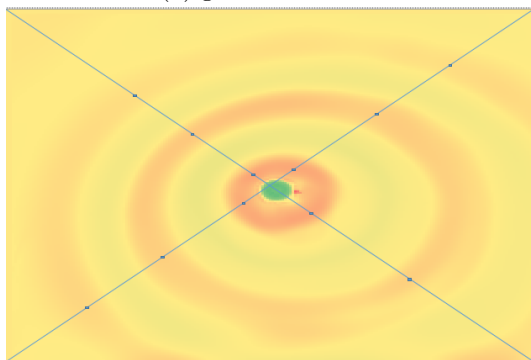
(a) gird size:  $0.5\ m$ (b) gird size:  $0.29\ m$ (c) gird size:  $0.17\ m$ 

Figure 4.35: wavelengths in the directions of following, opposing and normal currents at  $t = 10.8\ s$  for different grid resolutions. Small blue markers show the highest values in each wave which represent the wave crests.

determined as the distances between two neighbouring markers in its corresponding direction.

The snapshots of wavelengths in these directions on three grids are illustrated in Fig. 4.35a, 4.35b and 4.35c, respectively. The elliptic wave patterns are observed due to the Doppler effect of the current, instead of the circular waves in the absence of current. The wave length in the direction of the following current are longer than that in the direction of the opposing current. As is known, a ship at forward speed in calm water generates a Kelvin wave which includes diverging waves. In this work, no diverging waves are observed from the oscillating sphere in uniform current. The wavelength is in agreement with theory.

In addition, the ratios of wave amplitudes at different radii are also compared to the theoretical values in the direction of following, opposing and normal currents, respectively. It can be seen in Table 4.4 that the ratios of numerical wave amplitudes are in reasonable agreement with theory at the finest grid size of 0.17 *m*.

	0.5 m		0.29 m		0.17 m	
	A1 / A2	$\sqrt{R_2 / R_1}$	A1 / A2	$\sqrt{R_2 / R_1}$	A1 / A2	$\sqrt{R_2 / R_1}$
Following	1.43	1.44	1.62	1.46	1.61	1.45
Normal	1.44	1.54	1.52	1.54	1.48	1.51
Opposing	2.00	1.61	2.11	1.56	1.60	1.51

Table 4.4: Comparison of theoretical and numerical wave amplitudes ratios at different radii in the directions of following, opposing and normal currents at  $t = 10.8$  s

Disregarding the viscous forces, the total magnitude of the energy released from the oscillating sphere and transported by the wave is constant. Therefore, the power of the wave is also constant. In the case of a circular wave that is travelling in a two dimensional area, the power of the wave calculated at the distance  $r_1$  from the source is equal to the intensity  $I_1$  multiplied by the circumference of the circle  $2\pi r_1$ . The same power  $P$  calculated at a distance  $r_2$  from the source is equal to the intensity  $I_2$  multiplied by the circumference of the circle  $2\pi r_2$ , i.e.  $P = I_1 2\pi r_1 = I_2 2\pi r_2$ . Accordingly, the ratio of the intensities  $I_1$  and  $I_2$  is equal to the ratio of the radii  $r_2$  over  $r_1$ :  $I_1 / I_2 = r_2 / r_1$ . Since the intensity is proportional to the square of the amplitude of the wave and also to the square of the frequency  $f$  which remains constant, i.e.  $I_1 \sim A_1^2 f^2, I_2 \sim A_2^2 f^2$ . Therefore, the ratio of the amplitudes at different distance from the source can be obtained:  $A_1 / A_2 \sim \sqrt{r_2 / r_1}$ .



# Chapter 5

## Validation results

In this chapter, results from a validation study are presented. The numerical approach, which is explained in the previous chapters, is applied to the tests: heave and pitch motions of a Wigley hull at forward speed in head waves. The simulations are performed with GABC-1 imposed at both inflow and outflow boundaries to prevent reflection of waves into the computational domain. The experimental setup is described and an overview of the parameters in the simulations is provided, followed by the comparison between 3D ComFLOW wave-current-structure simulation results, in which a current velocity is used to model the ship's forward speed, and experimental results.

With the experiments involving a ship, we showed that the boundary condition GABC-1 not only works for theoretical conditions, but also for the cases where the ship generated waves are present. The simulated results in terms of ship motions take approximately one month, which is considered long, but still come close to the measurements. This work is the first to show validated ship motions for a combination of forward speed and waves within the ComFLOW project.

An application of green water impact on the deck of the Wigley hull is shown with the validated numerical method, by making the waves higher. A green water event is the name given to the situation that masses of water flow over the deck of the ship. The advantage of this simulation in ComFLOW is that one not only gets ship motions as in other models, but for a slightly harsher wave condition one can also predict and quantify water on the deck.

The chapter ends up with a discussion of the results.

### 5.1 Introduction

Vessels at sea are continuously subject to waves, wind and currents. These disturbances cause the vessels to move vertically. In addition, there are many maritime applications that require a compensation of the vertical vessel motion excited by

ocean waves and thus an exact knowledge about the vertical motion. Examples for such applications are safe aircraft landing on vessels and subsea lifting operations required for underwater installations on the seabed like pipelines and conveying systems for oil and gas. In this work, heave and pitch motions of a ship, with a constant forward speed in waves, in a truncated domain are investigated.

Ship parameters				
L (m)	B (m)	T (m)	Mass (kg)	J22 (m)
3.0	0.3	0.2	81.9	0.64

Table 5.1: Ship parameters used in the experiments and simulations. J22 is the radius of inertia for pitch.

A ship's heave and pitch motions vary with the wave length. In very long waves they will just follow the sea surface, while for shorter waves, near the heave and pitch resonance, they will be strongly amplified and out of the phase with sea surface.

A linear 3D Boundary Element Method (BEM) in the frequency domain is usually implemented to investigate ship motions. In contrast, in this work a Navier-Stokes solver, with the numerical approaches mentioned in previous chapters, is adopted to determine the heave and pitch motions of a ship moving forward in waves. The major differences between BEM and the Navier-Stokes solver ComFLOW for this application are: 1, the free surface position in ComFLOW is not linearized around a mean free surface; 2, the motion of the body is not linearized around a mean body position; 3, the free surface is not confined to a single value at each horizontal position  $(x, y)$ , but is free to flow over the deck of the body in large relative wave height situations. An experiment of a Wigley hull at forward speed in waves has been specifically designed and carried out at Delft University of Technology during the development of ComFLOW.



Figure 5.1: The wigley hull model in the towing tank

## 5.2 Experiment modeling

The experimental tests have been carried out in the towing tank at Delft University of Technology. The model used in the experiments is a Wigley hull. It is mathematically defined and used regularly for tests and validation work. The Wigley hull is based on the length  $L = 3 \text{ m}$ , the width  $B = 0.3 \text{ m}$  and the draft  $T = 0.1875 \text{ m}$ . However, the actual draft of the model in the experiment was  $0.2 \text{ m}$ , which was different from the  $T$  in the Wigley parameter set. The ship parameters used in the experiments and simulations are presented in Table 5.1.

Fig. 5.1 shows the photograph of the Wigley hull model in the experiments. The experiments have been performed in a quite long, but narrow wave tank. Waves are generated with a flap-type wavemaker at one of the narrow ends of the tank. At the opposing end a beach is present to induce wave breaking and reduce reflection. The model is initially positioned a considerable distance away from the wavemaker and towed by the carriage in head waves after the experiments start.

The motions of the Wigley hull are measured through two vertical position gauges, located a half meter away from the center of gravity (CoG) of the model. Then the heave and pitch motions at the CoG of the hull can be calculated. Fig. 5.2 shows the positions of the measurement instruments which will be utilized to compare the numerical results with the experimental results. The wave gauge *whm* fixed to the carriage, which was located at a distance of  $2.984 \text{ m}$  away from the center of gravity (CoG), measured the surface elevations. Also, video recordings have been made during the model tests. The measurements were stopped as soon as reflected waves from the beach started to arrive at the hull model in the tank. Several sea states such as regular and irregular long-crested waves as well as different forward speeds for the Wigley hull, were generated.

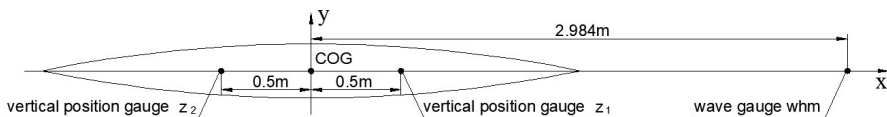


Figure 5.2: Vertical position gauges on the ship model

## 5.3 Numerical simulation

A number of simulations have been performed. A grid study is performed first. Then it is studied how the results change when the boundary, at which the GABC-1 with current is specified, is placed closer to the structure. In the end, the results of a Wigley hull at constant speed in an irregular head wave are present, to demonstrate the type of simulations that the boundary condition GABC-1 with current was designed for.

### 5.3.1 Grid study

In coarse grid simulations, a specific amount of grid-size-dependent numerical viscosity is applied to obtain a velocity field without spatial instability, effectively resulting in a first-order upwind discretization of the convective term in the momentum equation. Upwind discretization induces spurious wave energy dissipation, which is undesirable because it reduces the motion of a structure.

As a result, the aim of the grid study is to obtain sufficient grid resolution for representing the input, according to the measurements in the experiments, using the first-order upwind scheme. The grid study simulations are performed in 2-D computational domains. The domain size in  $x$ -direction was chosen to correspond to five wave lengths. The water depth is specified as 0.73 m in line with the depth in the experiment.

At  $t = 0$  the wave, having a period of 1.25 s, is generated with velocities according to Airy theory and ramped up linearly over two wave periods to the full amplitude into the computational domain. At every time step after the initial condition, the flow variables at the boundary are calculated according to the Airy wave theory, and prescribed at the inflow boundary.

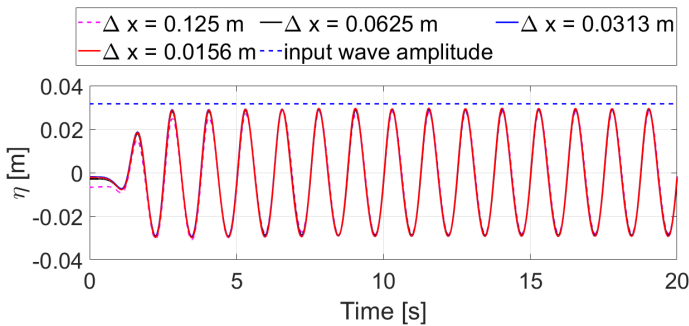


Figure 5.3: Time history of surface elevations for four grid resolutions

Four simulations are performed to obtain sufficient grid resolution for the desired wave height. The input wave height is 0.0633 m. The first simulation is performed with a mesh size of  $\Delta x = 0.125$  m on a uniform grid. With the same wave, the mesh sizes for the other three tests are refined to  $\Delta x = 0.0625$ , 0.0313 and 0.0156 m, respectively.

At both inflow and outflow boundary, the first-order generating and absorbing boundary condition (GABC-1) with current is applied. A free-slip condition is employed at the side boundaries of the computational domain, as it allows us to use a coarser grid near the outer walls.

The numerical surface elevations measured slightly inside the domain are depicted in Fig. 5.3. With the grid refined by a factor of 2 in three successive tests, the nu-

merical wave amplitudes increase from  $0.0282\text{ m}$  to  $0.0289\text{ m}$ ,  $0.0291\text{ m}$  and finally  $0.0294\text{ m}$ . As can be seen, the expected wave amplitude of  $0.0316\text{ m}$  is not yet reached. Increasing the vertical grid resolution in the wave height does not reduce the errors in terms of dissipation or numerical dispersion for this thesis. In addition, it is very likely to cause large errors in the VoF displacement algorithm to have a grid aspect ratio far away from 1.

With a refinement factor of 2, the computational cost will increase by a factor of  $2^4$ . Considering the grid numbers and durations adopted in the later simulations in this work, a further refinement level will make the simulations incredibly expensive. In order to obtain the desired wave height, our strategy is to specify a slightly higher input wave height in the simulation on relatively coarse grids.

### 5.3.2 Sensitivity study

The sensitivity study aims to investigate how the ship motions change when the domain boundary is located closer to the structure. Two waves are chosen from two tests 77 and 79 in the experiments, where different forward speeds of the ship are considered. The test identification numbers of the experiments with regular waves are given in Table 5.2, with wave heights, periods, lengths and ship forward speeds associated with these tests.

Run ID	H [m]	T [s]	$\lambda$ [m]	V_ship [m/s]
77	0.057	1.25	4.09	1.0
79	0.052	1.645	4.68	0.5

Table 5.2: Wave heights, periods, lengths and ship forward speeds in the regular wave experiments

The initial setup of the simulation 77 is given in Fig. 5.4. A Wigley hull is included in the computational domain. To make the Wigley hull clear, two more snapshots of the top and side view of the hull are presented in Fig. 5.5. The ship has a length of  $L = 3.0\text{ m}$ , a width of  $0.3\text{ m}$  and a draft with a value of  $0.2\text{ m}$ .

In the simulation 77, the Wigley hull is located at a distance of two ship lengths away from the inflow boundary. Another two ship lengths are left on the trailing side of the hull. Consequently, the size of the domain along the  $x$ - direction becomes  $L_x = 5L = 15\text{ m}$ . Along the  $y$ - direction, the width of the domain is selected the same as that in the experiment, which is  $L_y = 2.75\text{ m}$ . The water depth is specified as  $0.73\text{ m}$ , exactly the same as in the experimental towing tank.

For simulation 79, the dimension of the computational domain in the  $x$ - direction is  $L_x = 3.33L = 10\text{ m}$ , which is smaller than the domain size  $L = 15\text{ m}$  in the test 77. The width and water depth are taken as  $2.75\text{ m}$  and  $0.73\text{ m}$ , which are identical to those in the test 77.

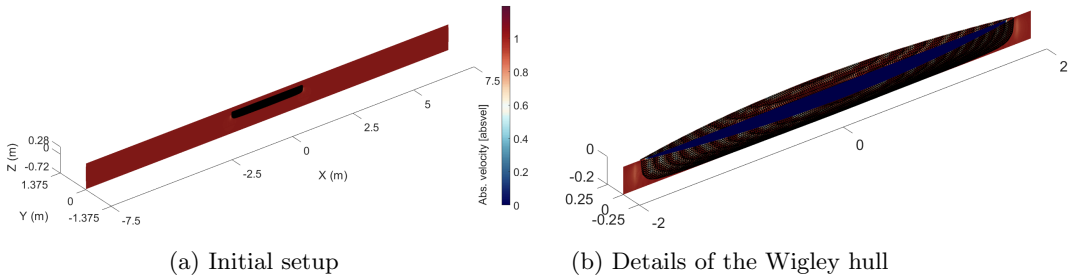


Figure 5.4: Initial setup for the test 77

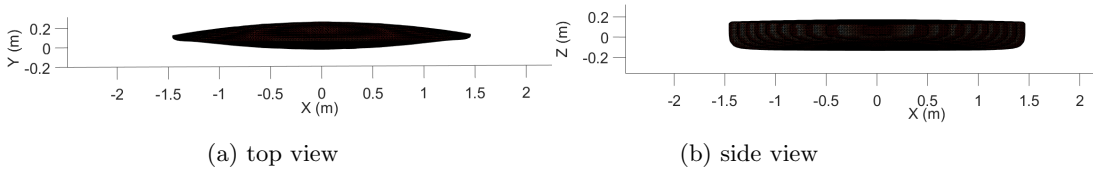


Figure 5.5: Top view and side view of the Wigley hull

The mesh is kept constant at  $\Delta x = \Delta y = \Delta z = 0.0156 \text{ m}$  in all three directions. The GABC-1 with current is applied at both inflow and outflow boundaries.

To calculate the interaction between the moving Wigley hull and waves, the quasi-simultaneous interaction law, described in Section 2.7 of Chapter 2, developed in ComFLOW has been used in this work, see Veldman et al. (2019). It makes use of a 6 DOF model for the dynamics of the geometry, which is solved simultaneously with the equations in the fluid domain. In the case of the Wigley simulations the degrees of freedom are restrained to heave and pitch only. The interaction law is a relation between the pressure and the local velocity of the body surface, which will show up as a boundary condition in the pressure Poisson equation.

**Results** For test 77, first the water surface elevation measured at  $2.984 \text{ m}$  in front of the Wigley hull is presented in Fig. 5.6. It can be seen that the resulting wave height from the numerical simulation is  $0.057 \text{ m}$ , which is identical as measured in the experiment. With this wave, the results of heave and pitch motions are obtained, see Fig. 5.7a and 5.7b. The numerical heave amplitude has a value of  $0.023 \text{ m}$ , which is the same as in the experiment. The pitch amplitudes measured in both the simulation and experiment are  $2.45^\circ$ .

For the test 79, the domain size is  $1/3$  times smaller than that in the test 77, the surface elevation measured also at  $2.984 \text{ m}$  in front of the ship hull is shown in Fig. 5.8.

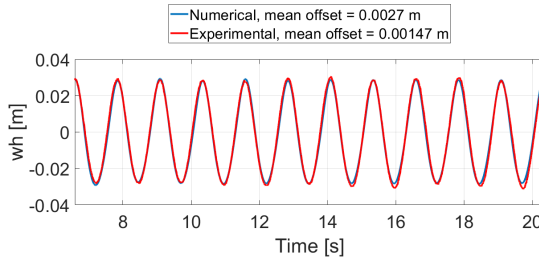


Figure 5.6: The comparison of numerical and experimental surface elevation for test 77

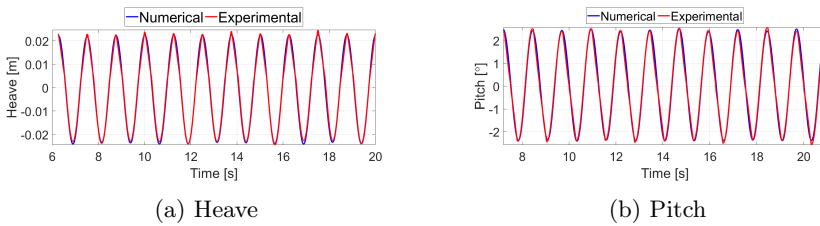


Figure 5.7: Numerical results of the heave and pitch motion for the test 77

The wave heights for both the simulation and experiment are  $0.052\text{ m}$ . Similarly as in the test 77, the resulting heave and pitch motions for the test 79 in the simulation and experiment are demonstrated in Fig. 5.9a and 5.9b, respectively. The average heave amplitude of  $0.018\text{ m}$  is obtained in the simulation, which agrees with that in the experiment. The average numerical and experimental pitch amplitudes are both  $1.57^\circ$ .

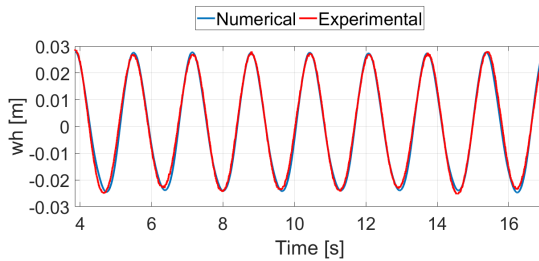


Figure 5.8: The comparison of numerical and experimental surface elevation for the test 79

**Discussion** It can be concluded from the sensitivity study that the boundary condition GABC-1 incorporating current works as fine in the smaller domain of test 79 as

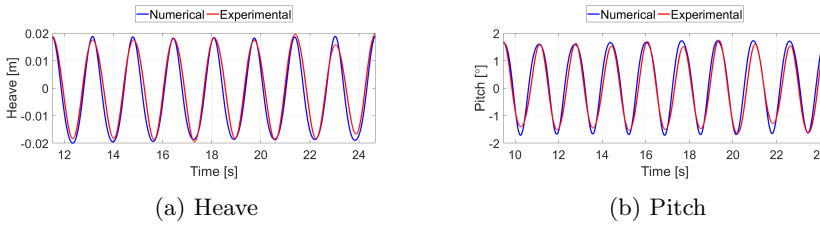


Figure 5.9: Numerical results of the heave and pitch motion for the test 79

in the large domain of test 77, for the Wigley hull at forward speed in regular waves with the same grid size. The domain boundaries can be located quite close around the geometry using this boundary condition.

### 5.3.3 Wigley hull at forward speed in irregular waves

In this section, an irregular wave, with the significant wave height being  $0.006\text{ m}$  and the peak period being  $1.39\text{ s}$ , will pass the Wigley hull causing wave diffraction and ship motions. The interaction between the irregular waves and the moving hull is simulated.

The numerical results from test 63 are presented. The forward speed of the hull in this test is  $0.5\text{ m/s}$ , and thus the Froude number is  $Fr = 0.092$ . This numerical experiment is intended to show that the boundary condition GABC-1 with current gives stable and accurate results for irregular waves. Numerical and experimental results are compared in terms of the surface elevations, as well as the hull's heave and pitch motions.

#### Input wave spectrum from the experiment measurement

To obtain the input wave spectrum for the numerical simulation, the wave signal from  $t = 42\text{ s}$  to  $t = 102\text{ s}$ , measured by the wave gauge located at  $2.984\text{ m}$  away from the center of gravity of the Wigley hull, is extracted as shown in Fig. 5.10.

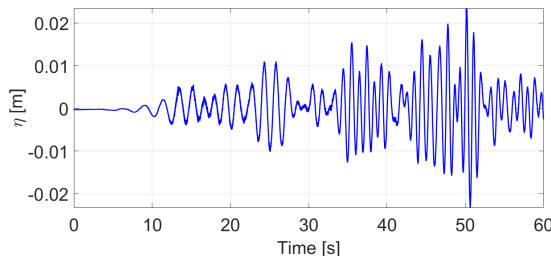


Figure 5.10: Time history of the wave from  $t=42\text{ s}$  to  $t=102\text{ s}$  in the experiment 63

By means of Fourier transform of the wave signal in Fig. 5.10, a wave spectrum with encounter frequencies is obtained. These frequencies need to be transformed to earth-fixed values as input in the numerical simulation. The Fourier components directly resulting from the Fourier transform are in complex form and the wave properties, such as wave amplitude and wave phase for each component, can be calculated from these complex numbers. With all wave properties known, including wave amplitudes, frequencies and phases, they can be used as input for the numerical simulation.

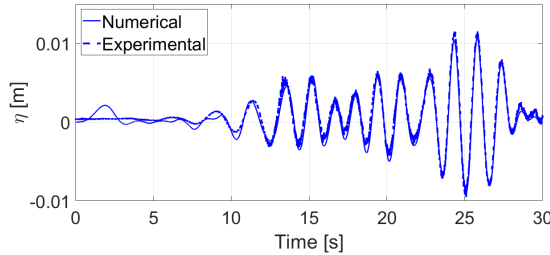


Figure 5.11: Surface elevation for test 63

**Simulation setup** The extent of the computational domain in the horizontal direction is  $12\text{ m}$ . The width of the domain is prescribed as  $2.75\text{ m}$  which is exactly the same as in the experiment. The water depth has a value of  $0.73\text{ m}$ . The boundary condition GABC-1 with current is applied at the outflow boundary of the domain. The grid size in all three directions is  $\Delta x = \Delta y = \Delta z = 0.015\text{ m}$ , which results in 10 million grid points. The time step is  $0.025\text{ s}$ .

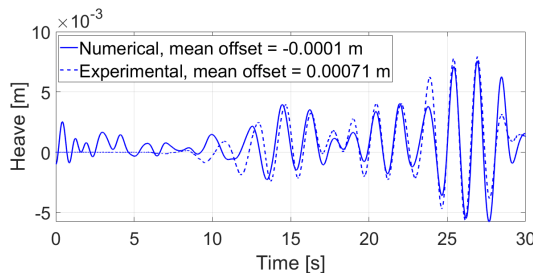


Figure 5.12: Heave motion for test 63

**Results** First the time series of numerical surface elevation at the inflow boundary is compared with the experimental results. For visualization the experimental surface elevation is shifted from  $t = 42\text{ s}$  to  $t = 0$ , as shown in Fig. 5.11. In the first 10 seconds, the numerical elevation is oscillating around the mean level. From then on, the root mean square error between the simulated and experimental surface elevation is  $0.001\text{ m}$ .

With this input wave, the resulting heave and pitch motions of the Wigley hull are obtained and compared with the experimental data in Fig. 5.12 and 5.13 respectively. There is a mean offset in both simulated and experimental heave motions, which is removed in the figure for comparison. There is a phase lag between two curves in the time interval between 10 and 15 seconds. After that the phase difference disappears. However, the amplitude of the numerical heave is lower between  $t = 17$  s and  $t = 25$  s and higher for the rest of the time than the experimental data. The root mean square error between the simulation and experiment is  $0.0011$  m.

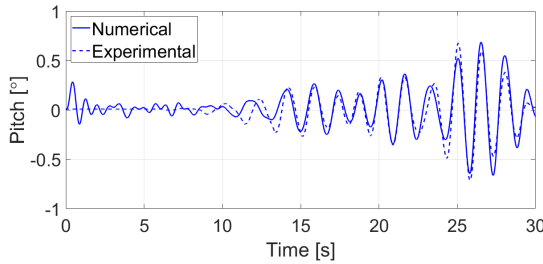


Figure 5.13: Pitch motion for test 63

In the comparison of the pitch motion, a slight phase difference between simulated and experimental results is also present but much smaller than in the heave motion. The root mean square error of the pitch amplitude obtained from the simulation is  $0.09^\circ$  compared to the experiment.

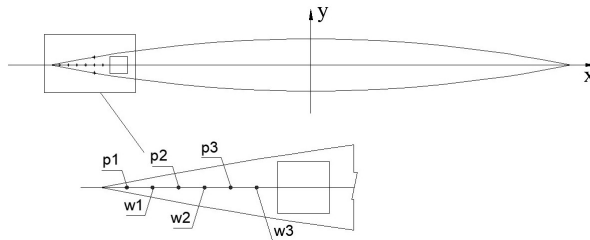


Figure 5.14: Monitor points locations in the simulation of regular waves. The distances of the wave gauges  $w_1$ ,  $w_2$  and  $w_3$  away from the front of the hull are  $0.1$ ,  $0.2$  and  $0.3$  m, respectively. The distances of the pressure gauges  $p_1$ ,  $p_2$  and  $p_3$  away from the front of the hull are  $0.05$ ,  $0.15$  and  $0.25$  m, respectively.

**Discussion** The simulation of a Wigley hull at forward speed in irregular head waves is completed with a good agreement with the experiment. This indicates that our boundary condition GABC-1 not only works fine for the theoretical conditions where only irregular waves exist in Chapter 4, but also works well for the cases where the ship generated waves are present. The ship generated waves are stationary with

respect to the ship, which means they do not propagate much. The validated results here have demonstrated that the ship generated waves do not disturb the boundary condition GABC-1 much.

### 5.3.4 Application: green water in extreme waves

Based on the validated waves and ship motions in the above sections, we will show one of the applications that the ComFLOW program has been developed for: green water in extreme waves. Buchner (2002) studied the physics of the green water process on the bow systematically. All phases of the green water problem were investigated, which included relative wave motions, water flow onto the deck, water behaviour and loading on the deck and green water impact on structures.

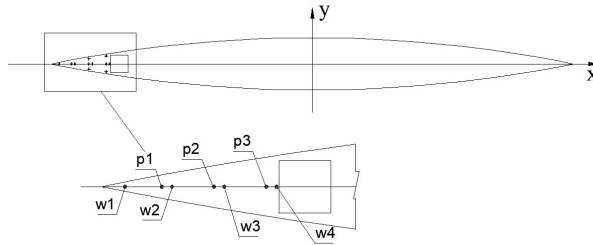


Figure 5.15: Monitor points locations in the simulation of irregular waves. The distances of the wave gauges  $w_1$ ,  $w_2$ ,  $w_3$  and  $w_4$  away from the front of the hull are 0.05, 0.14, 0.24 and 0.34  $m$ , respectively. The distances of the pressure gauges  $p_1$ ,  $p_2$  and  $p_3$  away from the front of the hull are 0.12, 0.22 and 0.32  $m$ , respectively.

Waves and currents can induce large forces on sea-going ships that have to operate under extreme weather conditions. For instance, in heavy storms waves and ship motions can become so large that solid amounts of sea water, called 'green water' flow over the deck, thus threatening the safety and operability of the ship. The amount of water flowing onto the deck depends on the relative motion of the ship versus the oncoming wave crest, as well as the phase between the ship and wave motions, which indicates the dependence on the wave group and its interaction with the ship dynamics.

Two simulations have been performed. In both test cases, a box is added on the deck of the Wigley hull, which was used in Section 5.3.2 and 5.3.3. The hull moves at a speed of 0.5  $m/s$  in the opposite direction of the wave. The Fig. 5.14 and 5.15 show the positions of the monitor points to capture the surface elevations and pressures.

**Regular wave** Firstly, a regular wave, with period  $T = 1.2$   $s$  and height  $H = 0.12$   $m$  is used. In  $x$ -direction the domain length is 10  $m$  and 640 cells are used. In  $y$ -direction, the domain size is 2.75  $m$ : 176 cells are used in the range  $[-0.7$   $m$ , 0.7  $m]$  and half the resolution is adopted for the rest. In  $z$ -direction 64 cells are specified from  $-0.4$   $m$  to 0.28  $m$  and also half the resolution in the rest areas. The time step is 0.025  $s$ . The

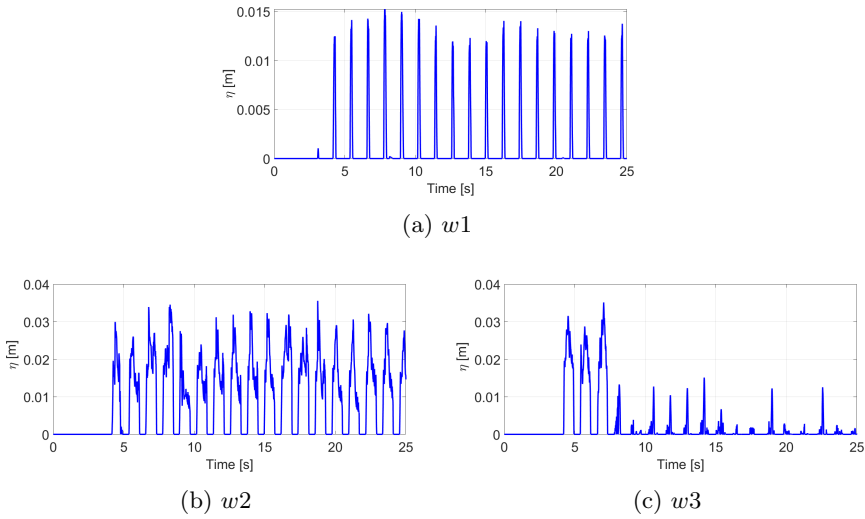


Figure 5.16: Numerical surface elevations at different positions on the deck of the hull in a regular wave. The distances of the wave gauges  $w1$ ,  $w2$  and  $w3$  away from the front of the hull are 0.1, 0.2 and 0.3  $m$ , respectively.

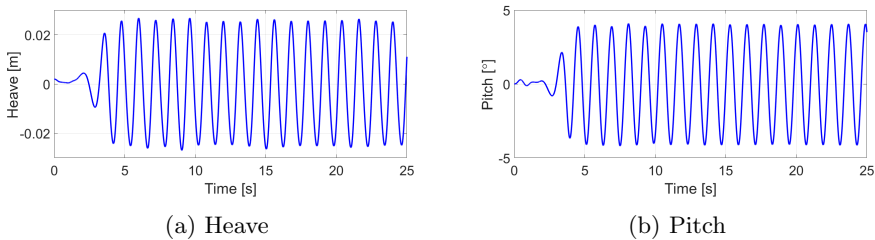


Figure 5.17: Numerical heave and pitch motions of the hull in a regular wave

first-order generating and absorbing boundary condition GABC-1 in this research is used at both the inflow and outflow end of the domain.

The surface elevations at four positions along the center of the structure on the deck are shown in Fig. 5.16. The wave becomes approximately two times larger near the box than in the foremost part of the hull. The resulting heave and pitch motions of the hull are illustrated in Fig. 5.17.

The pressures at three different locations are presented in Fig. 5.18. The green water on the deck of the hull is a result of the wave and ship motions. Negative pressures have been removed because they are artefacts of the numerical method. Snapshots of the simulation at several time instances are given from Fig. 5.19 to 5.21.

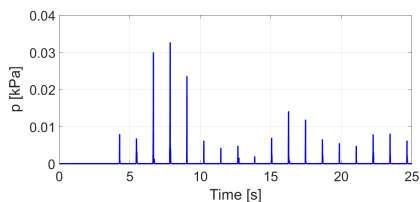
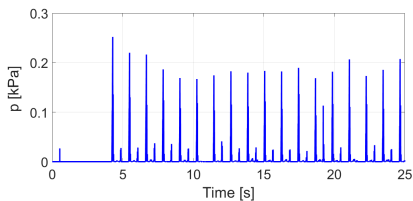
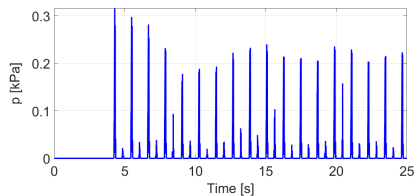
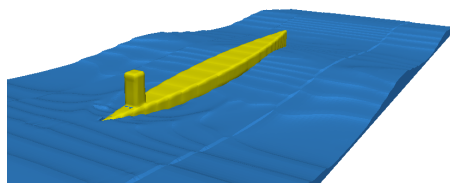
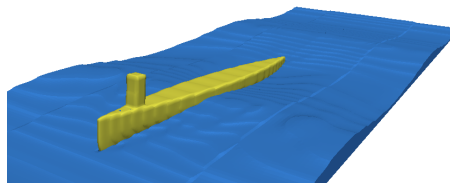
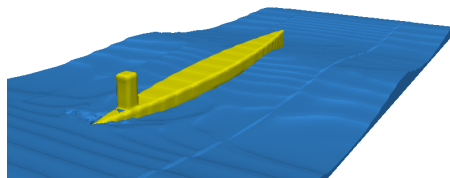
(a)  $p1$ (b)  $p2$ (c)  $p3$ 

Figure 5.18: Numerical pressures at different positions on the deck of the hull in a regular wave. The distances of the pressure gauges  $p1$ ,  $p2$  and  $p3$  away from the front of the hull are  $0.05$ ,  $0.15$  and  $0.25$   $m$ , respectively.

Figure 5.19: Snapshot at  $t = 6.3$   $s$  in a regular waveFigure 5.20: Snapshot at  $t = 7.0$   $s$  in a regular waveFigure 5.21: Snapshot at  $t = 7.5$   $s$  in a regular wave

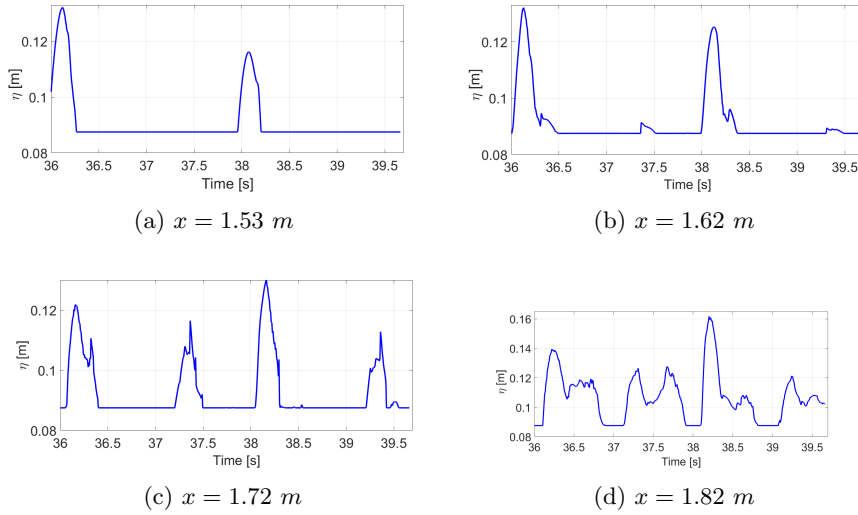


Figure 5.22: Numerical surface elevations at different locations on the deck of the hull in an irregular wave. The distances of the wave gauges w1, w2, w3 and w4 away from the front of the hull are 0.05, 0.14, 0.24 and 0.34  $m$ , respectively.

**Irregular wave** Secondly, an irregular wave, with the elevations being 6 times of those in Fig. 5.11 at all time instances, is adopted. The peak period remains 6  $s$ . The domain size in  $x$ ,  $y$ , and  $z$ -directions are 12, 2.75 and 1.1  $m$ , respectively. The grid sizes in all directions are uniform with a value of 0.0156  $m$ . The time step is 0.025  $s$ . The boundary condition GABC-1 is only applied at the downstream end of the domain.

Similarly, in the test with the irregular wave, several snapshots of the green water phenomenon are depicted as well. Time histories of the surface elevations at different locations on the deck are presented in Fig. 5.22. The heave and pitch motions of the hull caused by the wave are shown in Fig. 5.23. Fig. 5.24 gives the pressure signals at three locations. Their magnitudes are of the expected order. As has been studied

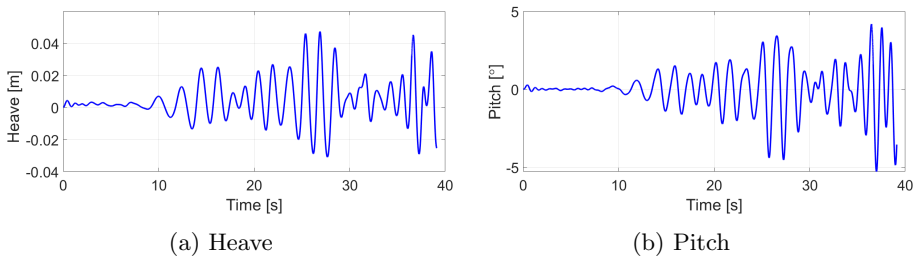


Figure 5.23: Numerical heave and pitch motions of the hull in an irregular wave

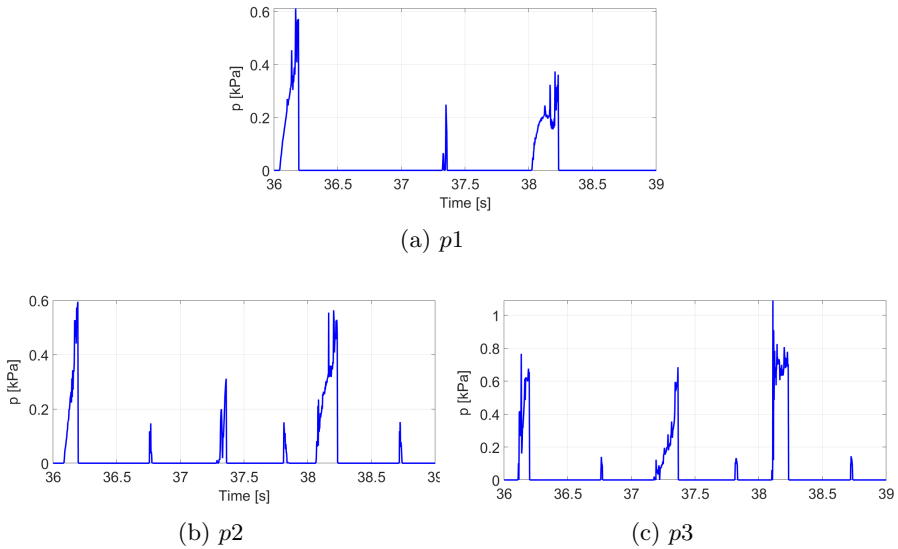


Figure 5.24: Numerical pressures at different positions on the deck of the hull in an irregular wave. The distances of the pressure gauges  $p_1$ ,  $p_2$  and  $p_3$  away from the front of the hull are 0.12, 0.22 and 0.32  $m$ , respectively.

in Buchner (2002), the air entrapment seems to be less disturbing for the green water problems compared to the breaking wave problem, since no overtopping is observed and thus no real air pockets can be trapped between the water and the structure. However, during the process of water flowing onto the deck, air may come into the water. During the final impact this air in the water can result in some cushioning.

With the bow of the hull moving downward and the wave crest reaching the bow at the same time, the water flows over the deck, see Fig. 5.25, and even run up the box as in Fig. 5.26. When the bow moves upward, the water on the deck decreases gradually, see Fig. 5.27.

### 5.3.5 Discussion

In this chapter, the boundary condition GABC-1 which is extended to include uniform current has been validated by means of test cases with a Wigley hull moving at forward speed in regular and irregular waves. The interaction between the sailing hull and waves is also incorporated.

For the simulation of the Wigley hull at two different forward speeds (0.5 and 1.0  $m/s$ ) in two regular waves with different amplitudes and periods, the resulting surface elevations, heave and pitch motions agree well with the experiments. From the sensitivity study, the inflow and outflow boundaries of the computational domain can be placed as close as 1.67 times of the ship length to the structure, which makes the computation

efficient and attractive for the maritime applications.

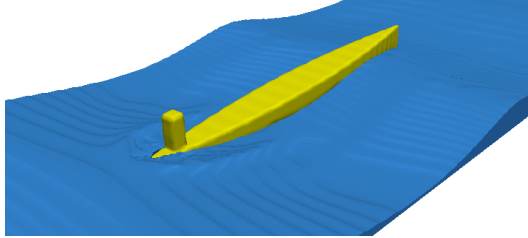


Figure 5.25: Snapshot at  $t = 37.0$  s in an irregular wave

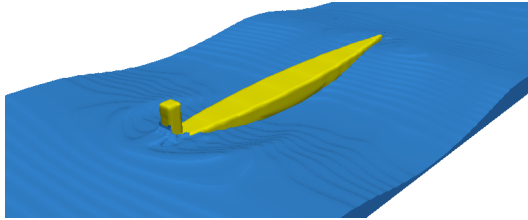


Figure 5.26: Snapshot at  $t = 37.2$  s in an irregular wave

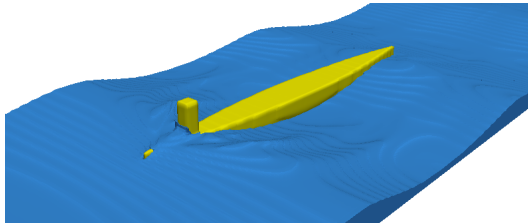


Figure 5.27: Snapshot at  $t = 38.2$  s in an irregular wave

In addition, in the test of Wigley hull at a forward speed of  $0.5$  m/s in irregular head waves, the resulting heave and pitch motions are also observed to be in good agreement with the experiments, which indicates that the boundary condition GABC-1 is applicable to moving vessels in long-crested waves, where the ship generated waves are present.

Finally, an application of green water impact on the deck of the Wigley hull is presented. With the method being validated for milder waves, the application demonstrates how the numerical method can be used as a first-principles-based extrapolation to more extreme waves. The green water phenomena demonstrated in the snapshots coincide with the surface elevations and the hull motions at the same time instances. It is an advantage for ComFLOW that one not only gets ship motions as in other

---

models, but for a harsher wave condition one can also predict and quantify water on the deck.



# Chapter 6

## Conclusions

This thesis presents the outcome of a doctoral study on the topic: an absorbing boundary condition for wave-current flow simulations in maritime applications. Modelling of wave loads on structures at sea is incomplete without currents and thus the combination of currents and waves is an important aspect of simulating a realistic loading environment. Prediction of nonlinear forces exerted on the structures demands that we consider the combination of waves and currents. The numerical approach that addresses the topic has been implemented in the CFD simulation tool ComFLOW. In order to perform numerical simulations for wave-current-structure interaction, absorption of reflections of these waves and currents from the boundaries of the computational domain is required. The thesis is dedicated to this problem, and results demonstrating the performance of such boundary conditions are included in Chapter 4 and 5. Below a summary of the findings and conclusions stemming from the results in this work are presented.

### **Verification with regular and irregular waves on top of currents**

By means of simulations of regular waves on top of six uniform currents, the first-order Sommerfeld condition (S-1) and generating and absorbing boundary condition (GABC-1), both including the effect of current, have been verified.

For each current, the simulated surface elevations for four waves, varying from small amplitude waves to mildly steep waves, at the inflow boundary are compared to the input waves first. With the small amplitude waves, which have small  $kh$  values, the numerical input waves agree well with the analytical solutions. In the cases of steeper waves, there exist discrepancies between simulated and theoretical amplitudes. These differences may be attributed to the fact that linear theory is used to generate these waves. Particularly, the opposing current further increases the steepness, i.e. nonlinearity, of these steeper waves.

Subsequently, numerical surface elevations of mildly steep waves at four positions in the domain, from near the inflow boundary to near the outflow end, are shown.

The wave heights decrease gradually from the inflow boundary to the outflow boundary due to numerical damping. However, the damping of the wave heights is within an acceptable level and does not influence the investigation of the reflected waves.

Lastly, the numerical reflection coefficients, defined as the ratio of the reflected wave amplitude and the outgoing wave amplitude, are studied in comparison with theoretical values. The findings and conclusions resulting from the condition Sommerfeld-1 and GABC-1 including current are presented as below.

**Sommerfeld-1 including current** For six currents: three following and three opposing ones, the numerical reflection coefficients are slightly off the theory, but they share the same trend.

Note that in the case of  $U = 1.0 \text{ m/s}$ , there is no reflection for the waves whose  $kh$  values are larger than 4.2 since these reflected waves modes are blocked by the current. For a larger following current, the reflected waves corresponding to the outgoing waves of the  $kh > 1.4$  cannot exist, because the group velocities of these waves become smaller than the current speed. The numerical reflections for the opposing current  $U = -2.0 \text{ m/s}$  are hardly observed due to excessive dissipation in these simulations.

**GABC-1 including current** For all six currents, the numerical reflection coefficients for 25 regular waves are lower than 5%. It is somewhat higher than the theoretical value, which is 2%. The difference between simulation and theory is mainly attributed to the fact that the boundary condition GABC-1 does not account for non-linearity: bound frequency components do not propagate at phase velocities which can be predicted with linear theory.

As can be seen, for the following current  $U = 0.5 \text{ m/s}$ , reflections for all 25 waves have been obtained and measured. Similar to the cases for the condition Sommerfeld-1, there is no reflection for the waves with  $kh > 4.2$  when  $U = 1.0 \text{ m/s}$  and for the components with  $kh > 1.4$  when  $U = 2.0 \text{ m/s}$ .

The simulated reflections obtained from the regular waves on top of the first two opposing currents  $U = -0.5 \text{ m/s}$  and  $U = -1.0 \text{ m/s}$  match well with theory. Again, the numerical reflections for the stronger opposing current  $U = -2.0 \text{ m/s}$  are hardly observed due to excessive dissipation in these simulations. For larger  $kh$  values, i.e. shorter wave length, the dissipation exceeds even 70%. The causes are not clear yet and need further investigation in the future.

### Verification with irregular waves on top of currents

The capability of the boundary condition GABC-1 with current to account for dispersive effects of waves on top of different currents is investigated as well. A JONSWAP wave spectrum, with a peak period of 6.0 s and significant wave height of 2.0 m, is imposed at the inflow side of the 2D computational domain. Two currents: one

following and one opposing, are accounted for.

For the following current  $U = 1.0 \text{ m/s}$ , the numerical reflection coefficients for the entire spectrum, with  $kh < 4.24$ , are less than 3%. On the whole, they are smaller than the theoretical amounts, especially for shorter waves. This may be caused by wave nonlinearity and insufficient grid resolutions for these shorter waves. There is no more reflection for  $kh > 4.24$ , because the corresponding reflected wave modes are blocked by the current.

In the presence of the opposing current  $U = -0.5 \text{ m/s}$ , the numerical reflection coefficients for the wave modes with  $3 < kh < 6$  are larger than theory. This difference may be attributed to several reasons. The first one is that the nonlinear interaction of waves at the boundary is not accounted for. Besides, the opposing current increases the wave steepness, which adds to the nonlinear effects at the boundary. The procedure to post-process the numerical results may also contribute to this deviation.

### **Verification with an oscillating sphere in the 3D domain**

In addition, to study how the second-order boundary condition ABC-2 incorporating current behaves, three simulations of an oscillating sphere in a current have been carried out on three grids. The sphere is allowed to make only vertical motion along the  $z$ -direction. After the impact of the sphere on the water surface initially with uniform current, a series of waves are produced radiating outward in all directions. The boundary condition ABC-2 with current is applied at the outflow ends of the computational domain.

The elliptic wave patterns are observed due to the Doppler effect of the current, instead of the circular waves in the absence of current. The wave length in the direction of the following current is longer than that in the direction of the opposing current. As is known, a ship at forward speed in calm water generates Kelvin wave which includes diverging waves. In this work, no diverging waves are observed from the oscillating sphere in uniform current.

In three simulations, wave lengths in the direction of the following, normal and opposing current have been inspected in comparison with the theoretical values. The ratio of simulated wave amplitudes at different radii are compared to theory in the above three directions, respectively. With grid refinement, the numerical wavelengths and the ratio of wave amplitudes at different radii in the direction of following, opposing and normal current agree well with the theoretical amounts.

### **Validation with experimental results**

In this thesis, model-scale experiments have been executed at the towing tank of Delft University of Technology to validate the present boundary condition GABC-1 with current. A number of numerical simulations have been performed to compare with the experimental results.

**Wigley hull in regular waves** First, the grid study simulations are performed to obtain sufficient grid resolution for representing the waves at the position where the ship hull is supposed to be. In simulation 77, the inflow and outflow boundaries of the domain are placed at 2.5 times of the ship length away from the hull. The simulated heave and pitch signals match well with the measured data in the experiment 77. Then in the test 79, the domain boundaries are moved closer to the hull, which is 1.67 times of ship length. The resulting heave and pitch motions are also in line with the experimental results. It indicates that the boundary condition GABC-1 including the effect of current works as fine in the small domain of test 79 as in the large domain of test 77, for the Wigley hull at forward speed in regular waves with the same grid size. The domain boundaries can be located at least this close to the structure using this boundary condition.

**Wigley hull in irregular waves** Subsequently, a test of the same Wigley hull at forward speed in irregular head waves is performed. The interaction between the irregular waves and the moving hull is simulated. The input wave spectrum is obtained from the Fourier transform of the experimental wave signal measured by the wave gauge. The boundary condition GABC-1 with current is applied at the outflow boundary of the domain.

The numerical input wave spectrum matches well with that extracted from the experimental data. The resulting heave and pitch motions of the hull agree well with the measured results. This indicates that our boundary condition GABC-1 not only works fine for the theoretical conditions where only irregular waves exist in Chapter 4, but also works well for the cases where the ship generated waves are present. The ship generated waves are stationary with respect to the ship, which means they do not propagate much. The validated results here have demonstrated that the ship generated waves do not disturb the boundary condition GABC-1 much. The diffracted and radiated waves of the ship have many different angles with respect to the boundary. They are expected to be less well absorbed.

### Future outlook

In this work, the first-order boundary condition GABC-1 with uniform current is verified and validated systematically. However, the second-order boundary condition ABC-2 with uniform current has only been tested in the case of an oscillating sphere in current. A complete study of the ABC-2 with uniform current is going to be an interesting subject, in which oblique waves moving with current need to be verified thoroughly.

Secondly, a depth-uniform current is considered in this work. However, linear and logarithmic profile current are worthwhile to be included in a future absorbing boundary condition for more practical phenomena.

Besides, the design of the boundary condition can accommodate further extensions. It

is important to note that linear potential theory is utilized at several points through the derivations. It is recommended to explore other possibilities for building non-linear effects in the design. This will improve simulation results with steeper waves.

It is also important to investigate the numerical damping, which is caused by the combination of a mean opposing current, waves and a first-order upwind discretization.

The reflection coefficient of the first-order Sommerfeld condition with current in the 2D domain is derived with an assumption, which requires further assessment.



# Appendix A

## 1D reflection coefficient

In this appendix, the theoretical reflection coefficient for the first-order Sommerfeld condition (S-1) incorporating uniform current in a one dimensional domain is derived.

Consider the condition S-1 applied to a wave potential function  $\phi_w$  and constant current  $U$ :

$$[\partial/\partial t + (c_{bc} + U)\partial/\partial x]\phi_w = 0, \quad (\text{A.1})$$

in which  $c_{bc}$  is a tuning parameter, which is an approximation of the intrinsic celerity, i.e. without current. The condition (A.1) is formulated in  $x$ - direction.

Suppose that an outgoing wave component and its reflected component can be identified. Then, the wave potential function  $\phi_w$  can be written as a combination of the outgoing wave potential and reflected wave potential:

$$\phi = \phi_{out} + \phi_{refl}. \quad (\text{A.2})$$

where  $\phi_{out} = A_{out}e^{i(\omega t - k_{out}x + \theta_{out})}$  and  $\phi_{refl} = A_{refl}e^{i(\omega t - k_{refl}x + \theta_{refl})}$ .  $A_{out}$  and  $A_{refl}$  are the amplitudes of the respective wave modes.  $k_{out}$  and  $k_{refl}$  are the wave numbers of the outgoing wave and reflected wave mode, respectively.

Note that the outgoing wave mode propagates along the positive  $x$ - direction. The reflected wave mode is produced by the outgoing wave mode when the boundary condition S-1 is not perfectly tuned to the wave mode. Accordingly, this reflected wave mode propagates in the opposite direction of the outgoing wave mode, i.e. along the negative  $x$  direction. Hence, the wave number  $k_{refl}$  is negative.

Since we have the relation  $\omega t_0 - k_{out}x_{bc} + \theta_{out} = \omega t_0 - k_{refl}x_{bc} + \theta_{refl}$  at a certain time  $t = t_0$  at the boundary  $x = x_{bc}$ , the phase for the reflected mode  $\theta_{refl}$  can be expressed as:

$$\theta_{refl} = \theta_{out} + (k_{refl} - k_{out})x_{bc}. \quad (A.3)$$

The wave numbers  $k_{out}$  and  $k_{refl}$  are obtained from the dispersion relation as follows:

$$\omega - kU = \pm \sqrt{gk \tanh(kh)} \quad (A.4)$$

To obtain the reflection coefficient, the following derivatives are required:

$$\begin{aligned} \partial\phi_{out}/\partial t &= i\omega\phi_{out}, & \partial\phi_{refl}/\partial t &= i\omega\phi_{refl} \\ \partial\phi_{out}/\partial x &= -ik_{out}\phi_{out}, & \partial\phi_{refl}/\partial x &= -ik_{refl}\phi_{refl}. \end{aligned} \quad (A.5)$$

Substitution of the relations in (A.5) into Eq. (A.1) and evaluation of the obtained expression yields:

$$\begin{aligned} &[\omega - (c_{bc} + U)k_{out}]A_{out}e^{i(\omega t - k_{out}x + \theta_{out})} \\ &+ [\omega - (c_{bc} + U)k_{refl}]A_{refl}e^{i(\omega t - k_{refl}x + \theta_{refl})} = 0. \end{aligned} \quad (A.6)$$

Then the reflection coefficient at the boundary  $x = x_{bc}$  is determined as:

$$R = \frac{A_{refl}}{A_{out}} = -\frac{[(c_{bc} + U)k_{out} - \omega]e^{i(\omega t - k_{out}x_{bc} + \theta_{out})}}{[(c_{bc} + U)k_{refl} - \omega]e^{i(\omega t - k_{refl}x_{bc} + \theta_{refl})}}. \quad (A.7)$$

Since the relation (A.3) at the boundary  $x = x_{bc}$  holds, the reflection coefficient  $R$  can be further written as:

$$\begin{aligned} R &= -\frac{(c_{bc} + U)k_{out} - \omega}{(c_{bc} + U)k_{refl} - \omega} \\ &= -\frac{k_{out}/\omega - 1/(c_{bc} + U)}{k_{refl}/\omega - 1/(c_{bc} + U)}. \end{aligned} \quad (A.8)$$

# Appendix B

## 2D reflection coefficient

In this appendix, the theoretical reflection coefficient for the first-order Sommerfeld condition (S-1) incorporating uniform current in a two dimensional domain is derived.

Consider the condition S-1 applied to a wave potential function  $\phi_w$  and constant current  $\mathbf{U}$ :

$$\left( (\mathbf{e}_x \cdot \mathbf{e}_k) \frac{\partial}{\partial t} + (c_{bc} + U_k) \frac{\partial}{\partial x} \right) \phi_w = 0, \quad (\text{B.1})$$

where  $\mathbf{e}_x$  and  $\mathbf{e}_k$  represent the unit vector in the  $x$ -direction and the wave direction  $\mathbf{k}$ , respectively.  $U_k = \mathbf{U} \cdot \mathbf{e}_k$ .

Similar to the derivation of 1D reflection coefficient in Appendix A, the wave potential function  $\phi_w$  is equal to:

$$\phi_w = \phi_{out} + \phi_{refl}, \quad (\text{B.2})$$

where  $\phi_{out} = A_{out} e^{i(\omega t - \mathbf{k}_{out} \cdot \mathbf{x})}$  and  $\phi_{refl} = A_{refl} e^{i(\omega t - \mathbf{k}_{refl} \cdot \mathbf{x})}$ .  $A_{out}$  and  $A_{refl}$  are the amplitudes of the respective wave modes. For the wave numbers, we have  $\mathbf{k}_{out} = (k_x^{out}, k_y^{out})$  and  $\mathbf{k}_{refl} = (k_x^{refl}, k_y^{refl})$ .

Outgoing wave modes leave the domain over the boundary in the direction of  $\mathbf{e}_k^{out}$ . The reflected wave mode is generated by the outgoing wave mode when the boundary condition S-1 is not perfectly tuned to the wave mode.

To obtain the reflection coefficient, the following derivatives are required:

$$\begin{aligned}
\partial\phi_{out}/\partial x &= -ik_x^{out} A_{out} e^{i(\omega t - k_x^{out} x - k_y^{out} y)} \\
\partial\phi_{out}/\partial y &= -ik_y^{out} A_{out} e^{i(\omega t - k_x^{out} x - k_y^{out} y)} \\
\partial\phi_{refl}/\partial x &= -ik_x^{refl} A_{refl} e^{i(\omega t - k_x^{refl} x - k_y^{refl} y)} \\
\partial\phi_{refl}/\partial y &= -ik_y^{refl} A_{refl} e^{i(\omega t - k_x^{refl} x - k_y^{refl} y)} \\
\partial\phi/\partial t &= i\omega(A_{out} e^{i(\omega t - k_x^{out} x - k_y^{out} y)} + A_{refl} e^{i(\omega t - k_x^{refl} x - k_y^{refl} y)})
\end{aligned} \tag{B.3}$$

Substitution of the above relations in (B.3) into Eq. (B.1) and evaluation of the obtained expression yield:

$$\begin{aligned}
&i[(\mathbf{e}_x \cdot \mathbf{e}_k)\omega - (c_{bc} + U_k)k_x^{out}]A_{out} e^{i(\omega t - k_x^{out} x - k_y^{out} y)} \\
&+ i[(\mathbf{e}_x \cdot \mathbf{e}_k)\omega - (c_{bc} + U_k)k_x^{refl}]A_{refl} e^{i(\omega t - k_x^{refl} x - k_y^{refl} y)} = 0
\end{aligned} \tag{B.4}$$

Then the reflection coefficient is found to be:

$$R = \frac{A_{refl}}{A_{out}} = - \frac{[(\mathbf{e}_x \cdot \mathbf{e}_k)\omega - (c_{bc} + U_k)k_x^{out}]e^{i(\omega t - k_x^{out} x - k_y^{out} y)}}{[(\mathbf{e}_x \cdot \mathbf{e}_k)\omega - (c_{bc} + U_k)k_x^{refl}]e^{i(\omega t - k_x^{refl} x - k_y^{refl} y)}} \tag{B.5}$$

Since the above relation holds at the positions  $\mathbf{x} = (0, y)$ , it is assumed that the potential terms have to be canceled out which results in  $k_y^{refl} = k_y^{out}$ . Then the theoretical reflection coefficient becomes:

$$\begin{aligned}
R &= \frac{A_{refl}}{A_{out}} = - \frac{(\mathbf{e}_x \cdot \mathbf{e}_k)\omega - (c_{bc} + U_k)k_x^{out}}{(\mathbf{e}_x \cdot \mathbf{e}_k)\omega - (U_k + c_{bc})k_x^{refl}} \\
&= - \frac{(c_{bc} + U_k)k_x^{out} - (\mathbf{e}_x \cdot \mathbf{e}_k)\omega}{(c_{bc} + U_k)k_x^{refl} - (\mathbf{e}_x \cdot \mathbf{e}_k)\omega}
\end{aligned} \tag{B.6}$$

The 2D dispersion relation for the reflected wave  $\mathbf{k}_{refl} = (k_x^{refl}, k_y^{refl})$  becomes:

$$(\omega - \mathbf{U} \cdot \mathbf{k}_{refl})^2 = gk_{refl} \tanh(k_{refl} h). \tag{B.7}$$

When taking the square root of the relation (3.43), the same root of the right-hand side applies as for  $k_{out}$ , i.e. both  $k_{out}$  and  $k_{refl}$  satisfy:

$$\omega - \mathbf{U} \cdot \mathbf{k} \equiv \sigma = \sqrt{gk \tanh(kh)}. \tag{B.8}$$

When  $k_y^{refl}$  is known, then for a given  $\omega$  this equation has only one unknown variable, i.e.  $k_x^{refl}$ . Peregrine (1976) shows that it can have several solutions. One of these corresponds with  $k_{out}$ , another one (if it exists) gives  $k_{refl}$ , and there can be more. We have seen in Section 3.5.1 that wave numbers can be complex, and we will now

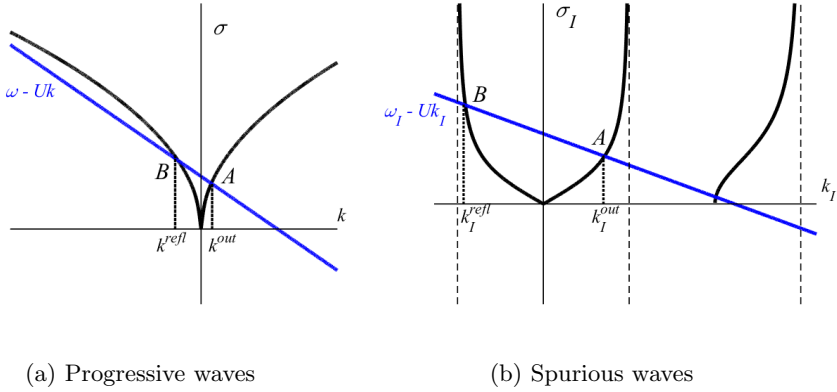


Figure B.1: The roots of the dispersion relations (B.8) for progressive waves (*left*) and (B.11) for spurious waves (*right*) are the intersection points of their left-hand sides (in blue) and their right-hand sides (in black) (*graphs inspired by Peregrine(1976)*).

treat several cases where  $k_y = 0$  and the current  $\mathbf{U}$  runs in  $x$ -direction.

### Progressive waves

For progressive waves the wave numbers  $k_{out}$  and  $k_{refl}$  are real, as is the frequency  $\omega$ . Fig. B.1(a) shows the left-hand side as well as the right-hand side of the relation (B.8). The intersection point giving the reflection is indicated by  $B$ . It is noted that  $0 \leq k_{out} \leq -k_{refl}$  (hence  $0 \leq -c_{refl} \leq c_{out}$ ). As  $\omega > 0$ , we have:

$$0 \leq \frac{k_{out}}{\omega} \leq -\frac{k_{refl}}{\omega} \quad (\text{B.9})$$

Also it can be seen that there no intersection occurs when the current is too large. This is understandable, since then the reflected wave is blocked by the current.

### Spurious waves

For spurious waves the wave numbers and the frequency are purely imaginary:

$$k_{out} \equiv ik_I^{out}; \quad k_{refl} \equiv ik_I^{refl}; \quad \omega \equiv i\omega_I; \quad \sigma \equiv i\sigma_I. \quad (\text{B.10})$$

The dispersion relation (B.8) now reads:

$$\omega_I - Uk_I^{refl} = \sigma_I^{refl} = \sqrt{gk_I^{refl} \tan(k_I^{refl}h)}. \quad (\text{B.11})$$

As mentioned above, for spurious waves  $0 + n\pi < |k_I h| < \pi/2 + n\pi$ , hence  $k_I \tan(k_I h)$  is positive and all terms in (B.11) are real. Fig. B.1(b) illustrates the solutions of the dispersion relation (B.11) by showing the intersection points of its left-hand side and its right-hand side. The outgoing wave is indicated at  $A$ , whereas the relevant

reflected wave corresponds with  $B$ . It is seen that  $0 \leq k_I^{out} \leq -k_I^{refl}$ . As now  $\omega$  is purely imaginary, we see that the inequality (B.9) also holds for spurious waves. Additionally, Fig. B.1(b) shows that more intersection points (can) exist, which correspond with higher order reflections, see Dingemans (1994).

### Evanescent waves

For evanescent waves, satisfying  $\pi/2 + n\pi < |k_I|h < \pi + n\pi$ ,  $k_I \tan(k_I h)$  is negative. The dispersion relation now reads:

$$\omega - iU_k k_I = \sqrt{-g k_I \tan(k_I h)}. \quad (\text{B.12})$$

In this situation where  $k$  is imaginary, i.e.  $k_I$  is real, the right-hand side is real. Without current, i.e.  $U_k = 0$ , this means that also  $\omega$  is real. Both  $k_{out}$  and  $k_{refl}$  satisfy (B.12), and a situation similar to Fig. B.1(b) applies, but now in the complementary  $k_I h$ -intervals and with a horizontal ‘blue line’, implying  $k_I^{refl} = -k_I^{out}$ .

However, with current, i.e.  $U_k \neq 0$ , (B.12) forms an equation in the complex plane, which complicates finding the desired root  $k_{refl}$  by analytical means. It will become complex, with non-zero real as well as imaginary parts. Numerically, the roots can be calculated following a continuation procedure in  $U$ , starting with  $U = 0$  for which  $k_I^{refl} = -k_I^{out}$ . For  $h = 1$ , Fig. B.2 shows the dependence of  $k_{refl}$  on  $U$  for two values of  $k_{out}$ :  $\pi i/4$  in the spurious range and  $3\pi i/4$  in the evanescent range. For large  $U$  the wave numbers  $k_{refl}$  approach  $-\pi i/2$ . It is clear that the evanescent reflections do not satisfy an inequality like (B.9). This will hamper the further analysis.

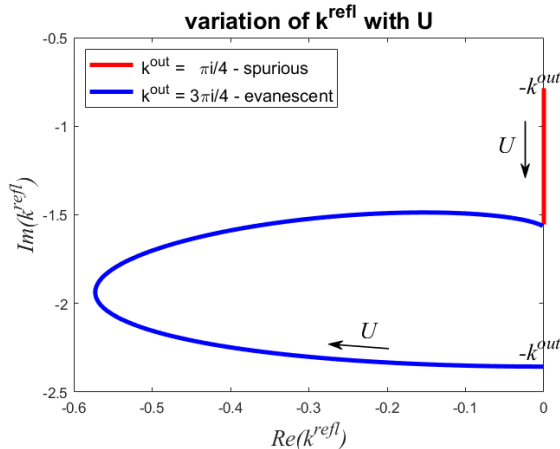


Figure B.2: Locus of  $k_{refl}$  with varying current strength  $U$  for a spurious wave  $k_{out} = \pi i/4$  and an evanescent wave  $k_{out} = 3\pi i/4$  (here  $h = 1$ ).

# Appendix C

## Coefficients in ABC-2

At the end of Chapter 3, we obtain the discrete equation (3.63) for the boundary condition ABC-2, in which a series of matrix coefficients are introduced. Their definitions are presented as follows:

$$\begin{aligned}\mathcal{K}_{rl} &= (\gamma\psi + \epsilon\psi + \lambda\chi + \kappa\chi)\mathcal{Q}_1 \\ \mathcal{K}_{rr} &= (\gamma\psi + \epsilon\psi + \lambda\chi + \kappa\chi)\mathcal{Q}_3 \\ \mathcal{K}_{rc} &= \gamma + \epsilon + \lambda\varphi + \kappa\varphi + (\gamma\psi + \epsilon\psi + \lambda\chi + \kappa\chi)\mathcal{Q}_2 \\ \mathcal{K}_{zl} &= (\gamma\psi - \epsilon\psi - \lambda\chi - \kappa\chi)\mathcal{Q}_1 \\ \mathcal{K}_{lr} &= (\gamma\psi - \epsilon\psi - \lambda\chi - \kappa\chi)\mathcal{Q}_3 \\ \mathcal{K}_c &= \gamma - \epsilon - \lambda\varphi - \kappa\varphi + (\gamma\psi - \epsilon\psi - \lambda\chi - \kappa\chi)\mathcal{Q}_2 \\ \mathcal{K}_{ll} &= \kappa\chi\mathcal{Q}_1, \quad \mathcal{K}_{rr} = \kappa\chi\mathcal{Q}_3, \quad \mathcal{K}_{lc} = \kappa\varphi + \kappa\chi\mathcal{Q}_2 \\ \mathcal{N}_{zl} &= (\lambda\chi/\tau_{pi+1} + \kappa\chi\tau_{ui})\mathcal{Q}_1 \\ \mathcal{N}_{zr} &= (\lambda\chi/\tau_{pi+1} + \kappa\chi\tau_{ui})\mathcal{Q}_3 \\ \mathcal{N}_c &= \lambda\varphi/\tau_{pi+1} + \kappa\varphi\tau_{ui} + (\lambda\chi/\tau_{pi+1} + \kappa\chi\tau_{ui})\mathcal{Q}_2 \\ \mathcal{N}_{ll} &= -\kappa\chi/\tau_{ui}\mathcal{Q}_1, \quad \mathcal{N}_{lr} = -\kappa\chi/\tau_{ui}\mathcal{Q}_3, \quad \mathcal{N}_{lc} = -\kappa\varphi/\tau_{ui}\mathcal{Q}_2 \\ \mathcal{O}_{zl} &= -\lambda\chi/\tau_{pi+1}\mathcal{Q}_1, \quad \mathcal{O}_{zr} = -\lambda\chi/\tau_{pi+1}\mathcal{Q}_3, \quad \mathcal{O}_c = -\lambda\varphi/\tau_{pi+1}\mathcal{Q}_2 \\ \mathcal{R}_{zl} &= \lambda\mathcal{Q}_1, \quad \mathcal{R}_{zr} = \lambda\mathcal{Q}_3, \quad \mathcal{R}_c = \lambda + \lambda\mathcal{Q}_2 \\ \mathcal{R}_{rl} &= \lambda\mathcal{Q}_1, \mathcal{R}_{rr} = \lambda\mathcal{Q}_3, \mathcal{R}_{rc} = \lambda + \lambda\mathcal{Q}_2\end{aligned}\tag{C.1}$$



# Bibliography

- T. L. Andersen, M. R. Eldrup, and P. Frigaard. Estimation of incident and reflected components in highly nonlinear regular waves. *Coastal Engineering*, 119:51–64, 2017.
- J. P. Berenger. A perfectly matched layer for the absorption of electromagnetic waves. *Journal of Computational Physics*, 114:185–200, 1994.
- E. Blayo and L. Debreu. Revisiting open boundary conditions from the point of view of characteristic variables. *Ocean Modeling*, 9:231–252, 2005.
- B. Buchner. Green water on ship-type offshore structures. *Delft University of Technology*, PhD thesis, 2002.
- A. Chawla and J. T. Kirby. Experimental study of wave breaking and blocking on opposing currents. *26th International Conference on Coastal Engineering*, 1998.
- L. F. Chen, Y. T. Wang, X. L. Wang, and X. S. Cao. 3d numerical simulations of green water impact on forward-speed wigley hull using open source codes. *Journal of Marine Science and Engineering*, 2020.
- J. Choi and S. B. Yoon. Numerical simulations using momentum source wave-maker applied to rans equation model. *Coastal Engineering*, 56(10):1043–1060, 2009.
- R. W. Clayton and B. Engquist. Absorbing boundary conditions for the numerical simulation of waves. *Geophysics*, 1980.
- M. W. Dingemans. Water wave propagation over uneven bottoms. *Delft University of Technology*, PhD thesis, 1994.
- M. Droge and R. Verstappen. A new symmetry-preserving cartesian-grid method for computing flow past arbitrary shaped objects. *International Journal for Numerical Methods in Fluids*, 47:979–985, 2005.
- D. Dumitru. Numerical investigation of a two-degree-of-freedom ship model fro pitch-roll motion. *IOP Conference Series: Materials Science and Engineering*, 2016.
- B. Duz. Wave generation, propagation and absorption in cfd simulations of free surface flows. *Delft University of Technology*, PhD thesis, 2015.

- B. Engquist and A. Majda. Absorbing boundary conditions for the numerical simulation of waves. *Mathematics of Computation*, 74(5):1765–1766, 1977.
- G. Fekken. Numerical simulation of free-surface flow with moving rigid bodies. *University of Groningen*, PhD thesis, 2004.
- P. C. Fernando, J. Guo, and P. Z. Lin. Wave-current interaction at an angle 1: experiment. *Journal of Hydraulic Research*, 49(4):424–436, 2014.
- J. Gerrits. Dynamics of liquid-filled spacecraft: numerical simulation of coupled solid-liquid dynamics. *University of Groningen*, PhD thesis, 2001.
- Y. Goda and Y. Suzuki. Estimation of incident and reflected waves in random wave experiments. *Proceedings of the 15th International Conference on Coastal Engineering*, 1(15):828–845, 1976.
- A. S. Hemming and G. Klopman. Review of multidirectional active wave absorption methods. *Journal of Waterway, Port, Coastal and Ocean Engineering*, 126(2): 88–97, 1985.
- T. A. Henriques, S. C. Tedds, A. Botsari, G. Najafian, T. S. Hedges, C. J. Sutcliffe, I. Owen, and R. J. Poole. The effects of wave-current interaction on the performance of a model horizontal axis tidal turbine. *International Journal of Marine Energy*, 8:17–35, 2014.
- R. L. Higdon. Absorbing boundary conditions for difference approximations to the multi-dimensional wave equation. *Mathematics of Computation*, 47(176):437–459, 1986.
- P. Higuera. Enhancing active wave absorption in rans models. *Applied Ocean Research*, 94:1–10, 2020.
- P. Higuera, J. L. Lara, and I. J. Losada. Realistic wave generation and active wave absorption for navier-stokes models. *Coastal Engineering*, 71:102–118, 2013.
- P. Higuera, I. Losada, and J. L. Lara. Three-dimensional numerical wave generation with moving boundaries. *Coastal Engineering*, 101:35–47, 2015.
- C. W. Hirt and B. D. Nichols. Volume of fluid (vof) method for the dynamics of free boundaries. *Journal of Computational Physics*, 39(1):201–225, 1981.
- J. M. J. Journee. Motions and resistance of a ship in regular following waves. *Website: www.shipmotions.nl*, Report 440, 2007.
- M. M. Karim and N. Naz. Computation of hydrodynamic characteristics of ships using cfd. *International Journal of Materials, mechanics and Manufacturing*, 5(4): 219–223, 2017.
- R. G. Keys. Absorbing boundary conditions for acoustic media. *Geophysics*, 50(6): 892–902, 1985.

- T. Kleefsman. Wave impact loading on offshore structures. *University of Groningen*, PhD thesis, 2005.
- W. Koo and M. H. Kim. Current effects on nonlinear wave-body interactions by a 2d fully nonlinear numerical wave tank. *Journal of Waterway, Port, Coastal, and Ocean Engineering*, 133(2):136–146, 2007.
- H. O. Kreiss. Initial boundary value problems for hyperbolic systems. *Communications on Pure and Applied Mathematics*, 23(3):277–298, 1970.
- E. M. Lane, J. M. Restrepo, and J. C. McWilliams. Wave-current interactions: a comparison of radiation-stress and vortex-force representations. *Journal of Physical Oceanography*, 37:1122–1141, 2006.
- Y. Li and M. Lin. Wave-current impacts on surface-piercing structure based on a fully nonlinear numerical tank. *Journal of Hydrodynamics*, 27(1):131–140, 2015.
- E. L. Lindman. Free space boundary conditions for the time dependent wave equations. *Journal of Computational Physics*, 18:66–78, 1975.
- A. Liu, X. Shen, G. H. Smith, and I. Grant. Particle image velocimetry measurements of wave-current interaction in a laboratory flume. *Optics and Lasers in Engineering*, 16:239–264, 1992.
- E. P. D. Mansard and E. R. Funke. The measurement of incident and reflected spectra using a least squares method. *Proceedings of the 17th International Conference on Coastal Engineering*, 1(17):154–172, 1980.
- M. Onorato, D. Proment, and A. Toffoli. Triggering rogue waves in opposing currents. *Physical Review Letters*, 2011.
- I. Orlanski. Simple boundary condition for unbounded hyperbolic flows. *Journal of Computational Physics*, 21(3):251–269, 1976.
- B. D. Paolo, J. L. Lara, G. Barajas, A. Paci, and I. J. Losada. Numerical analysis of wave and current interaction with moored floating bodies using overset method. *Proceedings of the ASME 37th International Conference of Ocean, Offshore and Arctic Engineering*, 2018.
- J. C. Park, M. H. Kim, and H. Miyata. Fully nonlinear free surface simulations by a 3d viscous numerical wave tank. *Journal for Numerical Methods in Fluid*, 29: 685–703, 1999.
- J. C. Park, M. H. Kim, and H. Miyata. Three-dimensional numerical wave tank simulations on fully nonlinear wave-current-body interactions. *Journal of Marine Science and Technology*, 6:70–82, 2001.
- D. H. Peregrine. Interaction of water waves and currents. *Advances in Applied Mechanics*, 16:9–117, 1976.
- D. H. Peregrine and I. G. Jonsson. Interaction of waves and currents. *U.S. Army Coastal Engineering Research Center*, 1983.

- R. Peric and M. Abdel-Maksoud. Reliable damping of free surface waves in numerical simulations. *Ship Technology Research*, 63(1):1–41, 2015.
- A. L. Perkins, L. F. Smedstad, D. W. Blake, G. W. Heburn, and A. J. Wallcraft. A new nested boundary condition for a primitive equation ocean model. *Journal of Geophysical Research*, 102(C2):3483–3500, 1997.
- J. E. Romate. Absorbing boundary conditions for free surface waves. *Journal of Computational Physics*, 99(1):135–145, 1992.
- Y. Sato, H. Miyata, and T. Sato. Cfd simulations of 3-dimensional motion of a ship in waves: application to an advancing ship in regular head waves. *Journal of Marine Science and Technology*, 4:108–116, 1999.
- R. Sherbin and A. J. Kings. Resistance analysis of wigley hull design on calm water using openfoam. *Proceedings of 4th international Conderence on Energy Efficient Technologies for Sustainability*, 2018.
- R. L. Soulsby, L. Hamm, G. Klopman, D. Myrhaug, R. R. Simons, and G. P. Thomas. Wave-current interaction within and outside the bottom boundary layer. *Coastal Engineering*, 21:41–69, 1993.
- I. K. Suastika. Wave blocking. *Delft University of Technology*, PhD thesis, 2004.
- C. Swan, I. P. Cummins, and R. L. James. An experimental study of two-dimensional surface water waves propagating on depth-varying currents. part 1. regular waves. *Journal of Fluid mechanics*, 428:273–304, 2001.
- M. J. Teles, A. A. P. Silva, and M. Benoit. Numerical modelling of wave current interactions at a local scale. *Ocean Modelling*, 68:72–87, 2013.
- S. V. Tsynkov. Numerical solution of problems on unbounded domains. a review. *Applied Numerical Mathematics*, 27:465–532, 1998.
- H. J. L. van der Heiden. Modelling viscous effects in offshore flow problems. *University of Groningen*, PhD thesis, 2019.
- P. van der Plas. Local grid refinement for free-surface flow simulations. *University of Groningen*, PhD thesis, 2017.
- A. E. P. Veldman. New, quasi-simultaneous method to calculate interacting boundary layers. *AIAA Journal*, 19:79–85, 1981.
- A. E. P. Veldman. A simple interaction law for viscous-inviscid interaction. *Journal of Engineering Mathematics*, 65:367–383, 2009.
- A. E. P. Veldman, H. Seubers, P. van der Plas, and J. Helder. Accelerated free-surface flow simulations with interactively moving bodies. *MARINE 2017, VII International Conference on Computational Methods in Marine Engineering*, 2017.

- A. E. P. Veldman, H. Seubers, P. van der Plas, S. M. H. Zahrae, and P. R. Wellens. Preventing the added mass instability in fluid-solid interaction for offshore applications. *Proceedings of 37th International International Conference of Ocean, Offshore and Arctic Engineering*, 2018.
- A. E. P. Veldman, H. Seubers, M. Hosseini, X. Chang, P. R. Wellens, P. van der Plas, and J. Helder. Computational methods for moving and deforming objects in extreme waves. *International Conference of Ocean, Offshore and Arctic Engineering*, 2019.
- G. K. Verboom and A. Slob. Weakly-reflective boundary conditions for two dimensional shallow water flow problems. *Advances in Water Resources*, 7(4):192–197, 1984.
- R. Verstappen and A. E. P. Veldman. Symmetry-preserving discretisation of turbulent flow. *Journal of Computational Physics*, 187:343–368, 2003.
- J. V. Wehausen and E. V. Laitone. Surface waves. *Encyclopedia of Physics*, 9:446–778, 1960.
- P. R. Wellens. Wave simulation in truncated domains for offshore applications. *Delft University of Technology*, PhD thesis, 2012.
- P. R. Wellens and M. Borsboom. A generating and absorbing boundary condition for dispersive waves in detailed simulations of free-surface flow interaction with marine structures. *Computers and Fluids*, 200:1–13, 2020.
- R. Wemmenhove. Numerical simulation of two-phase flow in offshore environments. *University of Groningen*, PhD thesis, 2008.
- J. S. Zhang, Y. Zhang, D. S. Jeng, P. L. F. Liu, and C. Zhang. Numerical simulations of wave-current interaction using a rans solver. *Ocean Engineering*, 75:157–164, 2014.



# Acknowledgements

In my journey towards this moment there are many people to thank. First I would like to thank my promotor, Rene H.M. Huijsmans, who provided me the opportunity to participate in the project ComMotion and a lot of encouragements. I owe a debt of gratitude to my copromotor, Peter Wellens and Arthur E.P. Veldman, who offered valuable help in my PhD life.

Peter, it is your excellent guidance and stimulating encouragements that help me step forwards continually. You never know how much confidence I have got from your reply 'we will make it'. Every time I ran into issues in research, you always gave me new insights and some possible alternative solutions. I also learned from you when to stop facing issues, which makes me avoid being stuck in useless efforts. Even after I went back to China, we still had regular discussions on the subject via email, Skype and WhatsApp. You put so much effort in our simulations, experiments and results analysis, which I appreciate a lot. You, as my copromotor, took care of the Dutch translation of the Summary. I owe you too much of thanks.

Arthur, your enthusiasm and dedication to the project have impressed me a lot. You are always patient to my questions and guide me how to approach the subject step by step. Countless emails have witnessed your efforts in my research. You have read all of my documents and slides seriously and given detailed comments every time. Your three-rounds comments on the dissertation have improved my confidence so much. I enjoyed our progress meetings at Delft and Groningen, in which you offered much constructive advice. I would never forget the moments right before I gave presentations at every STW and JIP meeting, your 'Xing, are you ready?' is a great support.

I thank all of the committee members for their reviewing my dissertation. Dr. Higuera, I appreciate your so much effort in reading my thesis. Your detailed and constructive comments help me prepare the defense better. Dr. Gao, thank you for finishing the review so quickly, which gives me much confidence. Prof. Visonneau, I appreciate a lot that you immersed yourself in the equations with interest. Prof. Hopman, thank you for reminding me to highlight the societal relevance of my thesis in Chapter Introduction and Conclusions. Prof. Cees, thanks for your attendance in both my Go/No Go meeting and defense.

As a PhD candidate of the project ComMotion, I thank all the participants who contributed to the STW and JIP meetings as well as the project managers Joop Helder and Tim Bunnik from Marin. Bogdan, Mart and Bulent, I am thankful for your interesting questions and useful feedback on my presentations. Riaan, thank you for your kind help, although with a short time.

My fellow PhD as well as officemate, Matin, I am grateful for your patient help in debugging even when you are under pressure and after I am back to China. We had a

lot of conversations on ComFLOW and worries in life, which relieved the stress effectively. Peter(vdP), I have many thanks for your valuable help in the code. I admire your ability to manage the whole ComFLOW program and great contribution to the project. Henk, thanks for your many suggestions from the perspective of mathematics. The cover of this thesis is from your painting on holiday which is pretty admirable.

My colleagues and friends in the corridor, Jun, Xiaobo, Marco, Pengpeng and Bobjun, thanks for your being in my PhD life. Jun, we shared a lot of dinner and shopping which leaves much pleasure in the Netherlands. Xiaobo, your kindness to friends and knowledge in history impressed me a lot.

Thank you, my friend Wen. You are my first female friend in the Netherlands and brought me plenty of enjoyments. Many thanks also to my housemates, Yawen, Yuetian, Tao and Lijian for your friendship. Yawen, thank you for keeping my personal stuff in your wardrobe for so long time. Yuetian, Hai and Qingsong, thank you for having me dinner before I left Delft.

I am grateful to China Scholarship Council (CSC) who provided a four-year funding for my PhD. Thank Xiaoli for your interview and introducing me to Rene.

Last but not least, I would like to thank my husband, Fan. Your unconditional love and support, both in life and research, creates the foundation of this achievement. We will face all the good and bad things together for the rest of our life.

# Curriculum Vitae

Xing Chang was born on 1 February 1990 in Shanxi, China. After she obtained her Bachelor degree in Naval Architecture and Marine Engineering at Wuhan University of Technology, she continued her M.Sc. in the same major at the same University. In 2014, she started her PhD study at Delft University of Technology, funded by China Scholarship Council (CSC). Her research interests include absorbing boundary conditions with current, ship motions in waves, green water loading and fluid-structure interaction.